Simulating monopile installation through scour protection using the Discrete Element Method

Evelien Hageman

Simulating monopile installation through scour protection using the Discrete Element Method

by

Evelien Hageman

to obtain the degree of Master of Science
at the Delft University of Technology,
to be defended publicly on the 18th of July 2022 at 10:00 AM

Student number: 5156602
Offshore and Dredging Engineering

Graduation committee

dr. Ir. D.L. Schott	Chair, TU Delft	Maritime and Transport Technology
dr. Ir. M. J. Mohajeri	TU Delft	Maritime and Transport Technology
dr. Ir. R.L.J. Helmons	TU Delft	Offshore and Dredging Engineering
Ir. V.M. Thumann	Seaway7	Geotechnical department
Ir. L.C.H. Braakenburg	Seaway7	Geotechnical department

An electronic version of this thesis is available at http://repository.tudelft.nl/.
Cover photo: Balmoral Comtec Ltd (2022)

Acknowledgment

First of all, I want to thank Javad Mohajeri, as my daily supervisor, he was a great help and inspiration throughout the whole process. The weekly meetings helped me to create structure and to continue working every time. His useful tips and feedback helped me to reach for higher quality within my research.
Secondly, I want to thank Rudy Helmons for our monthly update meetings and his honest feedback. I want to thank Dingena Schott for her input and enthusiasm during the progress meetings.
Furthermore, I want to express my gratitude toward Seaway7, where I was warmly welcomed and given the opportunity to create and execute my research plan. The interesting and useful talks with my supervisors Vladimir Thuman and Louisa Braakenburg were always much appreciated.
The Thursday meetings at 3ME with the Marine Transport and Technology department were an inspirational and fun moment of the week. The talks afterward with fellow students working in the DEMlab always was a good moment to help each other out with the next step in our graduation processes.
Furthermore, I would like to thank Stephan, my friends, and my family who supported me throughout my graduation, but also all the years before. They have always had confidence in me and I am very grateful for their support.

Abstract

Over 5000 offshore wind turbine generators have been installed in the past decades. 80% of these wind turbines have a monopile foundation. Monopiles are hollow steel tubular piles with a diameter of up to $10m$. The first phase of the monopile installation consists of the self-weight penetration into the seabed due to the mass of the monopile. Followed by the placement of the hammer, which installs the piles to the designated depth. A scour protection is deposited near the piles to avoid erosion (scour holes) around the monopiles. The scour protection consists of rock material with different size gradations and densities. Generally, the scour protection is installed in two campaigns. The first campaign consists of the installation of smaller rocks (filter layer), followed by the installation of bigger rocks (armour layer). Between these two campaigns, the monopile is installed through the filter layer. To achieve a more time-efficient installation sequence, in some projects a full scour protection (single layer) is deposited prior to the installation of the monopile. However, the technical feasibility of monopile installation through a scour protection has not been researched. Within practice, difficulties arise during the installation of monopiles through a single layer of scour protection. This leads to timely and costly delays.

This thesis contributes by use of simulations, to study the technical feasibility of monopile installation through scour protection. With a focus on the scour protection behavior in the first phase of the installation, where the monopile penetrates the seabed due to its mass, so-called self-weight penetration.

During monopile self-weight penetration, physical processes within the subsoil, scour protection, and monopile wall create penetration resistance. The most important physical processes during monopile self-weight penetration are identified using literature:

- The development of tip resistance due to the scour protection layer.
- The development of shaft resistance due to the scour protection layer.
- The self-weight penetration due to the weight and dimensions of the monopile.
- The interaction between the monopile wall and the scour protection rock, and inter-rock interaction (interlocking, rotation, breaking, and protrusion of the subsoil).

The Discrete Element Method (DEM) is considered most suitable for the representation of the scour protection behavior. DEM is an effective method for addressing engineering problems in granular materials. The most important reason for using DEM is due to the discontinuous behavior the scour protection materials. To set up the simulation, calibrated DEM input parameter sets are required to recreate reliable bulk behavior.

These parameter input sets are found with the use of two Key Performance Indicators (KPIs) of the bulk material: the porosity and the angle of repose. These KPIs are included because they represent the inter particle frictional resistance to movement. With the calibrated input sets combined with data from a case study, the Full-Scale Monopile Simulation is set up. Consistent with the case study, the simulation is designed using a monopile with a tip diameter of $8m$ and a wall thickness of $0.08m$. The seabed consists of a sandy subsoil and a scour protection on top.
To achieve a realistic stable simulation with a reasonable computational time, experiments are executed. Within an experimental design, a reference simulation is developed, followed by a parameter sensitivity analysis. The most important conclusions of the parameter sensitivity analysis are:

- When using an $8m$ diameter monopile, a minimum simulation domain of $12 * 12m^2$ is recommended. Resulting in a minimum of 2m space around the monopile.
- A subsoil is required for successful penetration through the scour protection layer.
- The subsoil input parameters are of significant influence on the penetration behavior of the monopile, due to the rock penetration into the subsoil.
- The scour protection thickness can be included as a variable parameter.

To verify whether the reference simulation properly represents practice, a qualitative validation is executed using the case study. Successful penetration is achieved within both the reference simulation and the case study. However, the current simulation does not present a comparable depth over time correlation. An underestimation of the penetration resistance is observed. Increasing the rolling resistance and therefore limiting the angular velocity of the particles results in higher penetration resistance. Restricting the angular velocity of the scour protection completely, results in an unsuccessful penetration.

Further research should focus on representative penetration resistance of the scour protection, combined with an alternative and more representative inclusion of the subsoil. Furthermore, the validation should be elaborated using adequate data from practice.

Contents

1. Introduction

Over 5000 offshore wind turbine generators have been installed in the last decades. The average design life of an offshore wind turbine is about 25 years. When the lifetime has passed, the turbines and foundations are removed fully and the area is available for new turbines. With an eye on circular wind farms, the existing scour protection may still be usable for new monopiles. It will create new opportunities when it is possible to install an offshore wind turbine foundation through existing scour protection. To identify this feasibility, a comparison with current practice can be made. The installation of scour protection for offshore foundations is currently executed in multiple phases:

1. Deposition of filter layer (smaller rock)
2. Installation of foundation
3. Deposition of armour rock (larger rock)

Hence, commonly the armour layer of the scour protection is installed after the foundation is installed. Currently, no guidelines exist regarding the technical feasibility to install offshore foundations through (armour) rock layers, whether this rock layer is an old scour protection from previous foundations or a pre-installed new scour protection.

1.1. Problem statement

The offshore renewable energy industry is a highly competitive market, therefore it is often required to work towards the limit of known possibilities, for example when it comes down to installing monopile through scour protection rock. Costly consequences could arise when crossing a limit. For example, when unexpectedly the monopile installation is not processing as expected due to the pre-installed scour protection, this leads to significant financial losses. Currently, the industry holds a technical note providing a recommendation towards driveability through filter layers and armour layers. The recommendation is *'Limit the size of the maximum stones (possibly the D_{50} size) to 3-5 times the wall thickness of the toe of the monopile'* (Seaway7 confidential, 2010). The word 'possibly' is rather peculiar, as is the wide range in the recommended ratio. Another note that should be given is that this document is dated 2010. Since 2010, monopiles have increased significantly in diameter. Slenderness ratio, the wall thickness over monopile diameter (t/D ratio) changed simultaneously. Where ratios of 4-8 were applied in the past, depending on the soil conditions. It is anticipated that a slenderness ratio of 3 or less will be used in the future. (Murphy et al., 2018) The reliability of this recommendation in the current industry is questionable.

Current installation sequence

Within a double-layered scour protection design, installation of the protection layers is mostly executed in two phases. Firstly, the filter layer (smaller rock) is installed, followed by the installation of the monopile. Secondly, the larger rock of the armour layer is installed around the monopile. Within this sequence, the scour protection installation vessel has to visit each location twice. Additionally, the placement of rocks around a monopile after installation is a more complex operation. A cost reduction of scour protection installation can be achieved by depositing all the rocks of the scour protection in a single campaign, before the monopile installation. Installing the scour protection before monopile installation is favorable, because of quick scour development, erosion occurs within a few hours after the installation of a monopile. Furthermore, rock deposition is easier without having to maneuver around the foundation. Monopile installation through scour protection asks for a deeper understanding of the mechanisms involved.

Case study

Currently, Seaway7 installs foundations where the full scour protection has already been pre-installed. A single layer protection is installed with a wider rock gradation, to function as a filter layer and armour layer simultaneously. Due to the pre-installed scour protection, difficulties arose during the installation of monopiles. Resulting in a higher installation time and sometimes even abortion of the installation. This has significant financial consequences.

1.2. Aim

This research aims to numerically model monopile installation through scour protection. Based on experience from practice, a limit regarding the possibility to install monopiles through scour protection is desired. The limit is where refusal during monopile installation occurs. Refusal means that the monopile cannot penetrate to the designated depth into the seabed. Whether this limit is due to the rock size, layer thickness or something else is currently unknown. The general aim is to find a limit concerning the technical feasibility of installing a monopile through scour protection.

1.3. Scope

Within this research, a better understanding of the technical feasibility of monopile self-weight penetration through scour protection is aimed for. This research includes the interaction of the scour protection material and the monopile during self-weight penetration. To start with the basics of the problem, the environmental conditions like the flow patterns around the monopile and weather conditions during installation are considered outside the scope of the research. The interaction between the pile and scour protection is the focus of the research.

1.4. Research questions and methodology

In current standards, no guidelines concerning monopile self-weight penetration (SWP) through scour protection exists, nor in public databases or at the company level. Unexpected conditions reported during monopile installation through scour protection are not publically available. Within a case study at Seaway7 undesired and unexpected conditions occurred.
Therefore the objective of this thesis is to increase understanding of the monopile SWP through scour protection. To achieve this objective, the following research question is formulated:

Is it feasible to develop a full-scale numerical model of monopile self-weight penetration through scour protection?

To answer the main research question, five sub-questions are formulated:

SQ1: What physical processes can be identified during monopile self-weight penetration through scour protection?

SQ2: What is an adequate numerical modelling method?

SQ3: What are appropriate parameter input sets for the bulk behavior of the scour protection?

SQ4: How can a numerical model for full-scale monopile self-weight penetration be reached with optimization in accuracy and computation time?

SQ5: To what extent does the full-scale numerical model represent practice?

1.5. Thesis outline

The research is built up in different chapters, Chapter 2 identifies the knowledge gaps in the literature and current research. In Chapter 3, the modeling techniques are explored. The parameter input, to mimic the scour protection behavior within the model is calibrated in Chapter 4. In Chapter 5, a full-scale numerical model off monopile installation through scour protection is presented, for which four experiments are introduced and executed. To verify the reliability of the Full-Scale Monopile Simulation, a qualitative validation is presented in Chapter 6. The conclusions and recommendations are given in Chapter 7.

2. Literature survey

This literature survey aims to increase the understanding of the current monopile installation sequence and identify the knowledge gaps within science. In this chapter, the first part of the literature survey is presented. The physical processes that can be identified during monopile installation will be given.

In the first section of this chapter, Section 2.1, will start with terminology. Monopile installation and the processes involved are presented in Section 2.2. In Section 2.3, the need for scour protection, the design, rock characteristics, and the installation of scour protection is explained. More in-depth information on the physical process involved in monopile installation is presented in Section 2.5. Two previously executed projects with pre-installed scour protection are presented in Section 2.6, followed by the identification of knowledge gaps in current research and the conclusions in Section 2.7.

2.1. Introduction to offshore wind turbine foundations

For ease of understanding the research, some basic terminology is presented in this chapter. This is combined with a short introduction to offshore wind turbine foundations in general.

As of the end of 2019, the total cumulative offshore wind capacity has exceeded 29 GW (Lee & Zhao, 2020). Offshore wind turbines can have multiple types of foundations, depending on the depth and environmental conditions. Floating and bottom-founded structures exist, a range of bottom-founded offshore structures are visualized in Figure 2.1. A common choice is monopiles when the water depth is not deeper than 35m (Bhattacharya, 2014). According to Gupta and Basu (2020), more than 80% of the substructures of offshore wind turbines are monopiles. At the end of 2019, 4258 of the 5258 installed wind turbine support structures were monopiles (Kay et al., 2021).

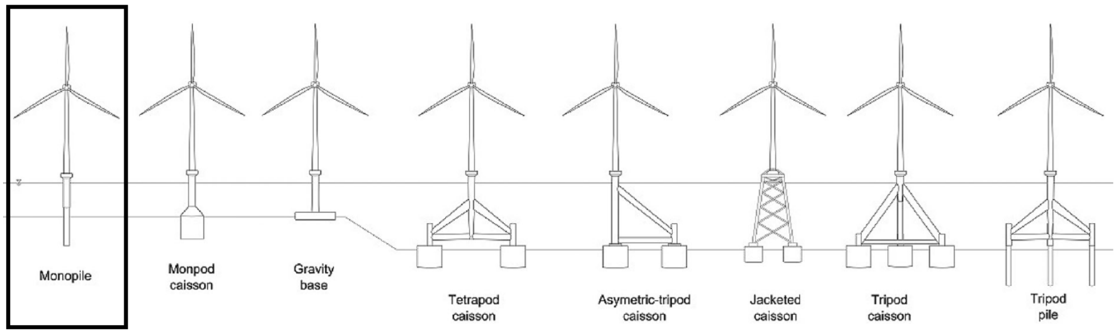

Figure 2.1: Offshore wind turbine foundations (Bhattacharya, 2014)

2.1.1. Terminology

To clarify some of the terminologies of the offshore wind industry, an image is constructed, see Figure 2.2. Note that this figure is not up to scale. In the figure, only a small part of the tower is shown and the nacelle, rotor, and blades are not incorporated. Starting at the bottom of the structure, the monopile is shown in dark grey. Around the monopile at the seabed, a scour protection is visualized. The scour protection maintains the integrity of the structure by preventing scour hole development. On top of the monopile, a yellow transition piece (TP) is installed. The transition piece can have multiple purposes. For example compensation of misalignment, the TP functions as the base structure for the boat landing as well. Commonly the tower of the wind turbine is connected to its foundation at the transition piece. On top of the tower, the nacelle, rotor, and blades are attached (not presented in this figure). In the figure also some dimensions are shown, for example the penetration. The penetration is equal to the length of the monopile within the subsoil.

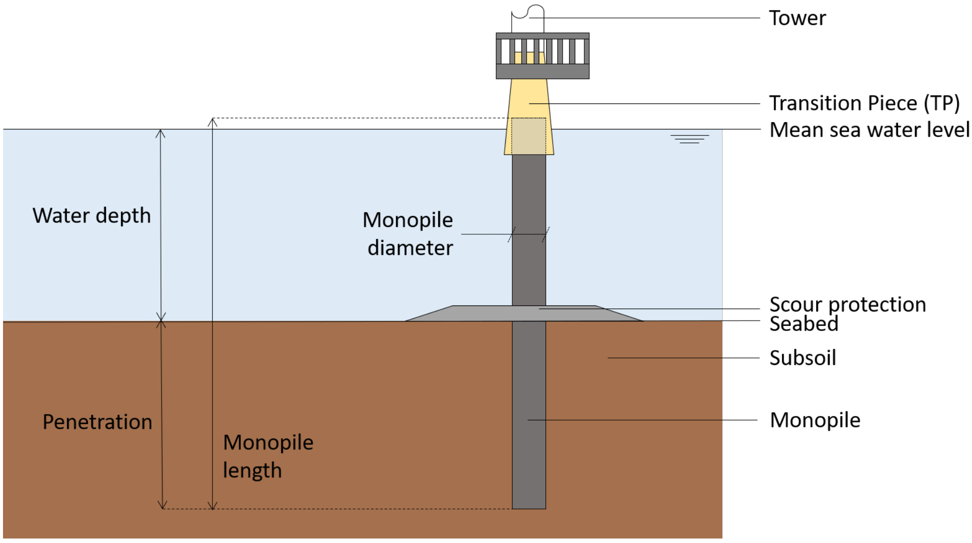

Figure 2.2: Terminology of monopile foundation for a wind turbine (not to scale)

2.2. Monopile installation

In this section, the monopile installation sequence is explained, and the physical processes involved are identified. Since not all physical processes can be taken into account, the scope is delineated.

2.2.1. Monopile installation sequence

To increase the understanding of monopile installation a 5-step sequence of this process will be explained. Figure 2.3 shows an infographic of a monopile installation sequence, starting with a vessel in blue, loaded with a monopile in grey, and the hammer in black. In this example a floating vessel is depicted, however, monopile installation can also be executed with a jack-up. A jack-up is a floating platform provided with legs on which it can stand stable on the seabed, without the interference of sea conditions. Other deviations within the installation sequence are possible, varying per project. The industry is growing rapidly and new technologies are implemented regularly. Therefore this installation sequence must be seen as a guideline.

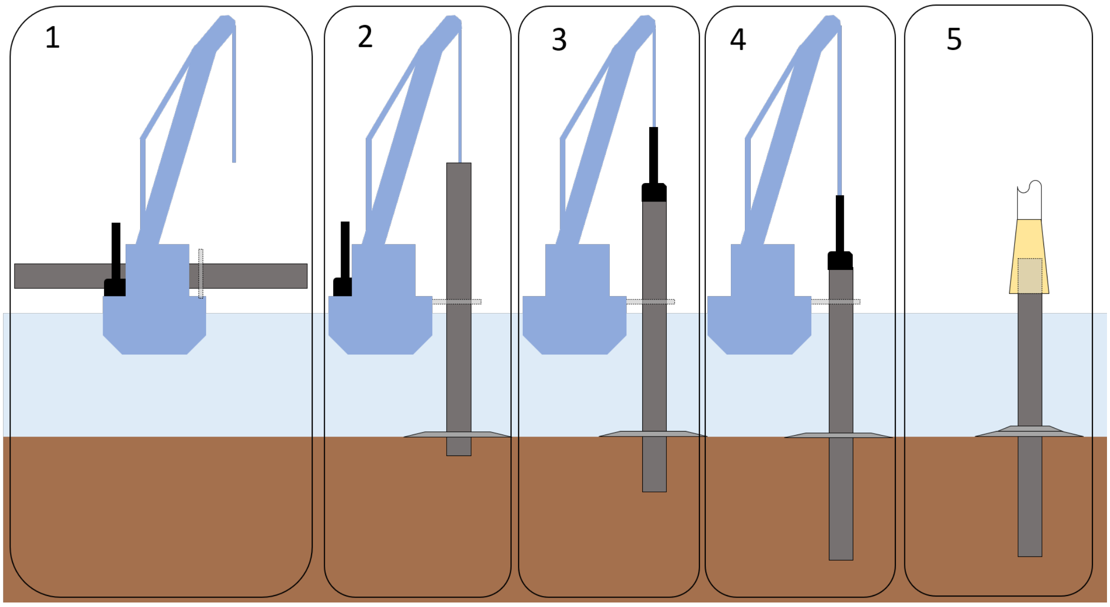

Figure 2.3: Monopile installation sequence

1. Within the first step, Figure 2.3, the monopile is transported from the yard to the installation site. At the installation site, the vessel is kept in place either using mooring or dynamic positioning (DP). Small movements can still occur, depending on the weather conditions. As the monopile is transported in a horizontal position, the pile needs to be hoisted in a vertical position before installation, also known as up-ending. This is done with the use of a crane mounted onto the vessel, additionally, an up-ending frame can be used, see Figure 2.4a. The monopile is re-positioned from the up-ending frame into a motion-compensated gripper on the side of the vessel with the use of the crane.

2. Further lowering of the monopile will take place, Figure 2.3. When it reaches the seabed, the earth's fixed position is determined and the monopile is turned when necessary. With the use of the gripper, the monopile is kept in a vertical position. Due to the weight of the monopile, it self-penetrates the seabed. Depending on the soil and scour protection properties, this is generally in the range of a few meters.

3. The crane is detached from the monopile, to place the impact hammer on top of the monopile, Figure 2.3 and see Figure 2.4b. When using a floating vessel, it is crucial that the monopile already feels some stability of the soil surrounding the pile, due to the top weight of the hammer. Otherwise, an unstable situation may arise. The weight of the hammer can be in the order of 0.5 times the monopile weight. Placing the hammer on top of the monopile results in further self-weight penetration of the monopile.

4. Now the monopile can be further hammered into the subsoil using the impact

hammer, Figure 2.3. Once the monopile is hammered to the designated depth the hammer can be removed and the monopile is released from the gripper.

5. The vessel might change position to place a transition piece (TP) on top, Figure 2.3. In the subsequent operation campaigns, an additional scour protection layer can be installed. And eventually, the wind turbine will be installed on top.

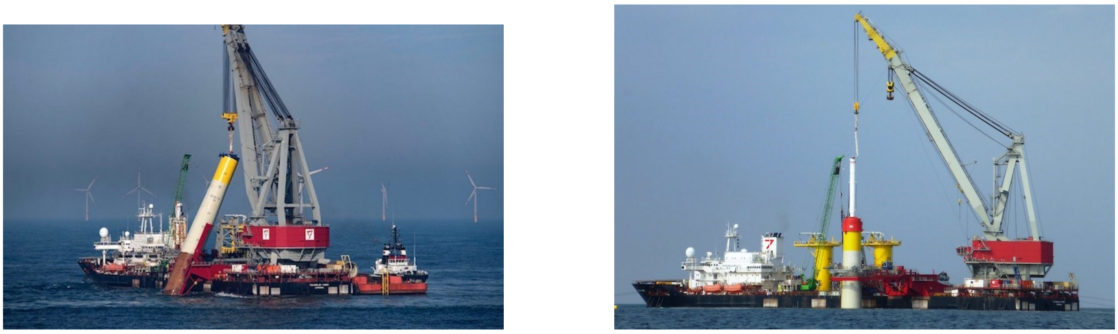

(a) Up-ending monopile (renew.biz,2018)

(b) Monopile with hammer on top (Splash,2020)

Figure 2.4: Installation of offshore monopile

After installation a monopile might not be perfectly vertical, however, it will be rather close. For each project different tolerance agreements are made, generally in the order of about 0.5°. With the use of a transition piece, some of the misalignment can be compensated when needed (Golightly, 2014). In the explanation above an impact hammer is used, another option is the use of a vibration lifting tool (VLT). This tool can be used during the up-ending of the monopile and vibrates the pile into the soil. An advantage of a vibration tool is the decreased noise impact. Generally, the VLT is used in combination with an impact hammer, since for the VLT more frequent refusal is encountered. Refusal means that the monopile has reached a point in which it cannot be penetrated further. Within this research, the VLT is outside the scope.

Sometimes surface obstacles are encountered during the installation of monopiles, which can be either natural obstacles or artificial ones like pre-installed scour protections. There is a lack of insight knowledge regarding the process of monopile installation when enhancing surface obstacles, like scour protection.
Three risks that might occur during the installation of monopiles are 1) refusal, 2) punch-through, and 3) drop fall. When refusal occurs, the monopile can not be hammered to the designated depth, this can happen due to interaction with a boulder, or a stiff layer in the soil. The opposite is a drop fall, where the monopile sinks too easily and possibly too far through a very soft layer of the soil. A punch-through is when an appearing refusal transfers to a sudden lowering of the pile.

Other uncertainties are the weather conditions during installation. There is an operation range in which installation can be executed, simply because it can become too dangerous during certain weather conditions. This range of good weather conditions is referred to as a weather window. Even within this window, a variation in conditions is present which might influence the ease and therefore the time of operations.

2.3. Scour protection

This section will shortly explain about scour, why it should be mitigated and how this can be achieved. Furthermore, rock characteristics are examined and the installation of scour protection is explained.

2.3.1. Scour

The presence of monopile foundations in water flow increases the hydrodynamic field locally, possibly producing an associated increase in sediment transport and erosion. This erosion is referred to as scour and the erosion around a monopile is a scour hole. More information about scour can be found in Schiereck (2004) and Breusers and Raudkivi (1991).

Need for protection

A scour hole around a monopile can cause severe problems regarding the stability of the pile, like loss of moment bearing capacity and fatigue-induced instability. This could even lead to failure of the monopile. Multiple solutions to prevent this phenomenon exist and are already brought into reality. An option is for example to increase the length and penetration of the monopile. More commonly, a scour protection is designed and installed around the monopile. A scour hole is not completely prevented, but it is moved away from the structure.

2.3.2. Scour protection design

Different scour protection materials are used: armour stone, filled nets or bags, or grouted fabric mattresses (Matutano et al., 2013). Rock armour is most commonly used as scour protection at monopiles, using gravel, quarry run stone, or blasted rock (usually limestone or granite rocks) (Whitehouse et al., 2011). Rock scour protections in the form of stone depositions, are often seen in practice. Rock protections originally consist of a filter layer and armour layer, see Figure 2.5. The filter layer consists of smaller rock than the armour layer. Where the armour layer guards the stability of the protection and the filter layer prevents the subsoil from eroding through the stone layer above. In practice currently, one layered protections are used as well, where a wide gradation takes care of both the stability of the rocks and prevents the eroding subsoil.

Design parameters

The design of scour protection focuses on the diameter of the stones, the extent of the protection, the gradation width, and the thickness of the layers (Fazeres-Ferradosa et al., 2018). What dimension the scour protection should have, has been studied by multiple researchers (Fazeres-Ferradosa et al., 2018) (Matutano et al., 2013) (Ciria et al., 2006). The stability of the rocks required is different in the methods. This difference has to do with the critical shear stress, which is the minimum shear stress necessary to drag the stones from their initial conditions, also known as the threshold of motion indicated with the non-dimensional Shield parameter. The non-dimensional Shields parameters (Θ_{cr}) is used in design equations. Commonly used is the value $\Theta_{cr} = 0.56$, corresponding to the start of motion. (Schiereck, 2004)
The median nominal diameter (D_{n50}) of the upper layer is calculated with the help of the wave and current data, this is an iterative process. Due to placement uncertainties, additional materials are added to the design to ensure the stability of the protection. Making a thin layer accurately in deep water is unrealistic. The accuracy of layer thickness under water is d/2, with a minimum of $0.2m$. (Schiereck, 2004)

Scour protection design example

In Figure 2.5 an example of scour protection design is given, this example is from the Princess Amalia wind farm. The figure identifies the median nominal diameter (D_{n50}), minimum extend and the thickness of the layer. (Esteban et al., 2019)

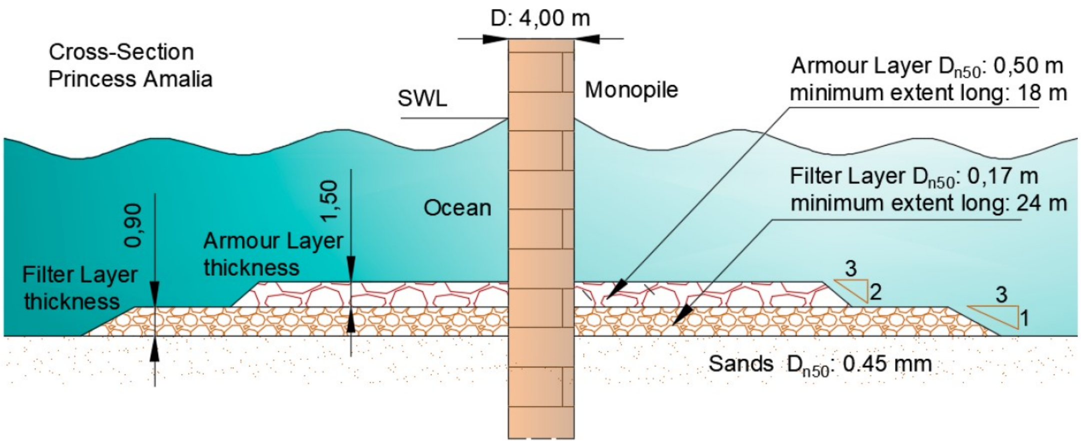

Figure 2.5: Scour protection design example of the Princess Amalia wind farm (Esteban et al., 2019)

2.3.3. Rock characteristics

In the previous section, the importance of the rock size is clarified. However also other rock characteristics are of importance. In this section the rock size/gradation, rock density and rock shape are discussed. Scour protection rocks will shortly be discussed as well.

Rock size and gradation

Rocks are classified by the normal grain size of d_{50}. This means that 50% of the grains are smaller than the value of d_{50}. This value is determined by a sieve sample, where a sample of material is sieved and rock sizes are determined. Not only the d_{50} but also for example d_{15} and d_{90} are measured. These values are used to identify the rock size gradation of the material. Plotting this data results in a curve, where the steepness represents the grading width. This curve is referred to as the particle size distribution (PSD). The grading width classifies rocks in narrow-, wide- or very wide gradations. With the commonly used term 'rip-rap', is referred to armour stones with a wide gradation, which generally are placed in bulk and used in revetments. When referring to a 'well graded' sample implies that there are no significant gaps in the sizing of the materials.
When the rocks become larger (in the order of 300 kg), sieving is rather difficult or even impossible. Therefore, a different procedure is followed for this. A sample is taken (for example a truckload) and the weight of all individual stones is determined. From the particle weight distribution following from this a W_{50} is determined, just as the W_{85} and W_{15}. These numbers are used to determine the grading width of the sample. Most design formulas make use of the d_{n50}, the median nominal diameter, similarly in Figure 2.5. Using the formula below the diameter can be expressed in weight and visa versa. (Schiereck, 2004)

$$D_{n50} = \sqrt[3]{\frac{W_{50}}{\rho_s}} \tag{2.1}$$

With ρ_s being the solid density of the sediment, expressed in kg/m^3.

Rock density

The density of rock(s) can have multiple meanings, it is not always specified what specific density is used. A list of density definitions is given (*The Rock Manual*, 2007):

- Real mass density (ρ_{real}): the mass density of the mineral components of the rock.
- Apparent mass density (ρ_{app}): the ratio of mass over its volume. Where the volume is determined by the water displaced where pores of the rock may be filled with water.
- Relative buoyant density ($\Delta = \frac{\rho_{app}}{\rho_w} - 1$)

In design calculations of scour protection design the apparent mass density is used (ρ_{app}). (*The Rock Manual*, 2007)
A contribution to the list of densities above is:

- Bulk density $\rho_b = \frac{m_b}{V_T}$: the bulk material mass $[kg]$ divided by the volume $[m^3]$ occupied by this bulk material

The bulk density is an important behavior characteristic of bulk materials. The bulk density can be interchanged with the porosity of bulk materials. Both define a ratio between the mass of bulk material and voids between granular material.

Rock shape

When the D_{n50} and PSD are known, still a large variation in the shape exists. Within any size distribution of particles in bulk, the size and shape distribution are dominant factors governing the porosity.
Different ratios are classified to give more insight into shapes. Four characteristics are distinguished, *length-to-thickness ratio*, *blockiness*, *cubicity*, and *roundness*. (*The Rock Manual*, 2007)

Length-to-thickness ratio (LT)
The length-to-thickness ratio (LT) is the maximum length divided by the minimum distance between parallel lines in which the rock would just pass, visualized in Figure 2.6. The LT is also referred to as the aspect ratio.

$$LT = \frac{l}{d} \tag{2.2}$$

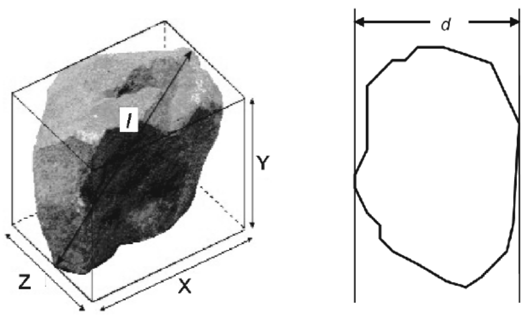

Figure 2.6: Illustration of armour stone shape measurement systems (*The Rock Manual*, 2007)

Blockiness (BLc)
The BLc of a stone is expressed in a percentage, it defines the ratio between the volume of a stone over the volume of the enclosing XYZ box with a minimum volume. As shown in Figure 2.6, in the left image. The BLc is determined using the following equation:

$$BLc = \left(\frac{M}{\rho_{app}} \cdot \frac{1}{X \cdot Y \cdot Z} \right) \cdot 100 \tag{2.3}$$

The BLc can also be referred to as the compactness of bulk material, correlating well with the packing behavior. A high BLc promotes the positioning of stones with a higher number of sub-parallel faces aligned, given higher bulk densities and a greater number of contact points and therefore more interlocking. Interlocking this is discussed in Section 2.5.3. (*The Rock Manual*, 2007)

Cubicity
The cubicity is also known as the form index, the cubicity is determined by:

$$cubicity = \frac{L+G}{2E} \tag{2.4}$$

L, G and E are the longest, intermediate and shortest orthogonal dimensions, starting by defining L. The cubicity is received as a more objective measurement than blockiness when stones become highly irregular. It is unknown whether the cubicity is better than the LT.

Roundness
When stones have encountered significant weathering, the roundness of the rock plays an important role in the bulk behavior of the material. The roundness of the rock can be quantified by visual comparison charts. An example is the Fourier asperity roughness P_R (-), introduced for quantifying wear and roundness. This is considered outside the scope of the research. (Bradbury et al., 1991)

Using a combination of the BLc and the LT has multiple advantages: (*The Rock Manual*, 2007)

- The packing and porosity of bulk materials can be predicted more accurately;
- More accurate predictions can be made regarding the stability and hydraulic performance;
- And a match between armour stone behavior in a prototype and hydraulic models can be made

Scour protection rock

For scour protection usually the materials come from a quarry, classifying it as natural armourstone. Depending on the quarry the strength and other parameters can be defined. As quarry rock is 'made' to become scour protection and it has not seen any weathering yet, the material is rather angular. However, along the way from the quarry to the installation site, some weathering occurs. As presented in Section 2.5.3, these minor breakage has no significant influence on the D_{n50} or the PSD.

2.3.4. Installation procedure

Different vessels can be used for scour protection installation. In Figure 2.7 three examples are shown from left to right: a side stone dumping vessel, a slip hopper barge and a fall pipe vessel. The image visualizes clearly how each of the vessels operates. Dumping stones from a barge cause large displacement errors. For a higher accuracy during placements, a fall-pipe vessel can be used. In the stone deposition activities for depth greater than $15m$ and stones above $300kg$, a tolerance of $+1.5m$ to $-0.5m$ can be achieved. (Schiereck, 2004) The accuracy of placement is checked afterwards by the as-built measurement of the scour protection.

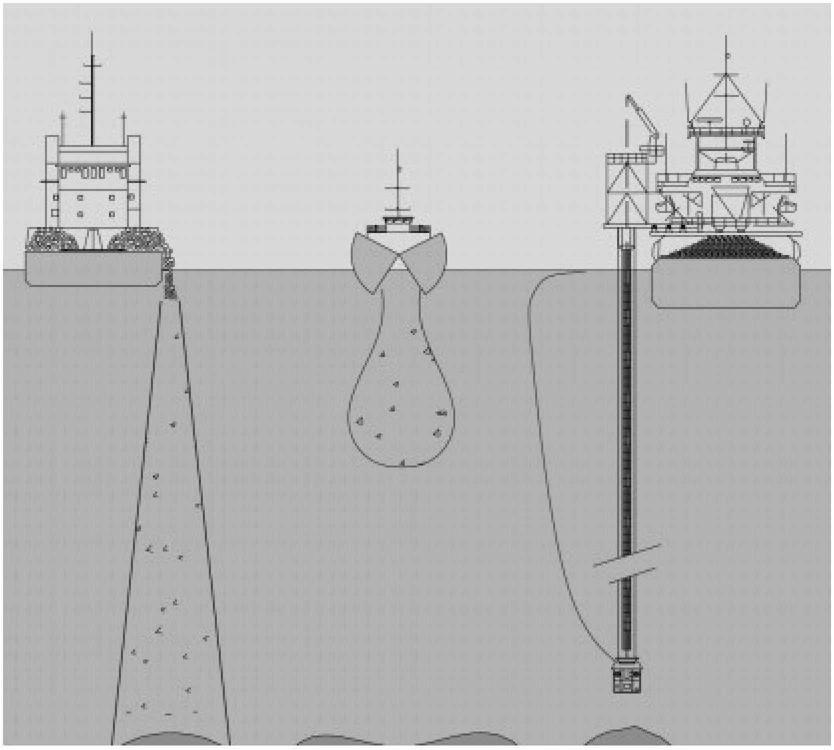

Figure 2.7: Scour protection installation vessels (Ciria et al., 2006)

2.4. Soil parameters

For the design of offshore wind foundations, soil investigations need to be carried out. This is because of the design of the foundation and to determine the installation tool. Soil investigations are executed to identify the soil stratigraphy of a specific location. This can vary largely over an area of a wind farm and therefore all locations are designed separately, or bins of turbines are created with similar soil characteristics. A combination of in situ testing and laboratory testing should be carried out to sufficient depth. In situ testing is for example done by Cone Penetration Test (CPT), where a rod with a cone-shaped tip is pushed into the soil. (Van Der Male, 2020)
After the geotechnical investigation at the site combined with sampling testing in the laboratory, the following geotechnical data should be provided for all important layers:

- Soil and rock description and classification;
- Deformation and shear strength properties;
- In-situ stress conditions.

Soils are classified as sand or clay and everything in between. A large variation in sand and clay exists and based on the ratio between the cone resistance and friction ratio different types of soil can be identified. An example of a classification scale is from Robertson. Robertson (1990) defines 12 zones, where the soil types vary from organic materials, silty clay to clay, and very stiff fine-grained, visualized in Figure 2.8.

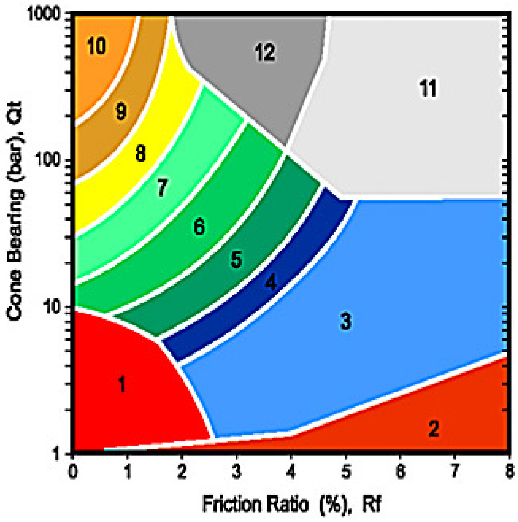

ZONE		SBT
1		Sensitive, fine grained
2		Organic materials
3		Clay
4		Silty clay to clay
5		Clayey silt to silty clay
6		Sandy silt to clayey silt
7		Silty sand to sandy silt
8		Sand to silty sand
9		Sand
10		Gravely sand to sand
11		Very stiff fine grained*
12		Sand to clayey sand*

*over consolidated or cemented

Figure 2.8: Robertson soil classification (ITRC, 2022)

The behavior of soil is further explained in Section 2.5.

2.5. Physical process

In Section 2.3.4 an overview of monopile installation and the physical processes included are introduced. Within this section, the processes will be further elaborated using available research.
As the scope of the research defines, the focus is on the self-weight penetration of the monopile during the installation. Steps 2 & 3 of the installation sequence in Figure 2.3 show the self-weight penetration of the monopile, in which several of physical processes can be identified:

- Self-weight penetration I (due to the weight of the monopile)
- Self-weight penetration II (due to the weight of the monopile and the hammer)
- Penetration resistance
- Interaction with scour protection

Starting with an introduction on pile driveability, the focus will be on the self-weight penetration. Afterward, the soil resistance to driving (SRD) and a method used to execute calculation on the penetration resistance are explained. Followed by a section on movements in the scour protection during pile installation.

2.5.1. Pile driveability

Before the design of a monopile is finalized a driveability assessment is carried out. There are different methods to determine the driveability. These methods predict the pile driveability in siliceous sand and clay. Three methods are given by Shonberg et al. (2017): Toolan and Fox (1997); Stevens et al. (1982) and Alm and Hamre (1998, 2001). A classification society within the energy, maritime, and oil and gas industry is DNVGL, within their standard on offshore soil mechanics, it is stated that driveability analysis consist of three stages (DNVGL-RP-C212, 2017):

1. Estimation of soil resistance during pile driving (SRD) vs depth
2. Estimation of blow counts versus SRD and pile stresses during driving using one-dimensional wave equation analysis
3. Combine the results to calculate the blow count curves

As determined in Section 1.3 the scope of this research does not include the pile driving using the hammer. Therefore not all three stages mentioned above will be elaborately discussed. The focus is on soil resistance during self-weight penetration.

2.5.2. Self-weight penetration (SWP)

The process of self-weight penetration is split into phases I and II, simply for ease of explanation. Self-weight penetration is the process in which the monopile is penetrating the seabed due to its weight (SWP I) and the weight of the hammer on top (SWP II). The SWP can be estimated using different methods. The SWP is predicted until the depth at which the soil resistance is greater than the combined weight of the monopile and the hammer. Shonberg et al., 2017 made a comparison between different self-weight penetration prediction models for large diameter monopiles (6m) in the North Sea Soils. Their focus is on a specific offshore wind farm, Westmonst Rough offshore wind farm, about 9km off the UK coast. The self-weight penetration of 35 monopile foundations is closely monitored and compared with prediction methods. A differentiation is made between soil resistance to driving (SRD) methodologies and a skirted foundation penetration assessment. The skirted foundation methodology is outside the scope of this research, as this research focuses on monopile foundations. The SRD methodology is designed to execute calculations regarding the pile driving during the installation process, according to Shonberg et al. (2017) this method is also applicable to the self-weight penetration.

Soil resistance to driving methodology (SRD)

The SRD is a summation of the shaft friction and the tip friction, the combination of the two is the static resistance part. Within the dynamic part of the SRD, also the damping during hammering is included.
Different researchers came up with different methods of SRD, the input of these methods are generally CPT data. The most common methods are; Toolan and Fox (1977) Stevens et al. (1982) and Alm and Hamre (1998); Alm and Hamre (2001). It is found that the Stevens et al. (1982) method is the most accurate in predicting the average SWP, however the predictions have a high standard deviation. Generally the Stevens et al. (1982) method under-predicts the SWP in clay soil while an over-prediction in sand is identified. When combining the average and the standard deviation, the Alm and Hamre (2001) method provides the best results. (Shonberg et al., 2017)
In the research of Shonberg et al. (2017) two of the 35 locations in the research have a substantial lower SWP compared to the predictions. Unforeseen variations in the ground are likely the reason for this. Small boulders, discrete cemented layers, or cobbles are examples that could lead to an SWP considerably lower than expected. These obstacles are expected to have a significant influence on the SWP and are therefore excluded from the research of Shonberg et al. (2017). This decision shows the lack of knowledge on the penetration resistance when larger obstacles like stones or cobbles are involved.

Alm and Hamre (2001) Soil resistance to driving methodology

The Alm and Hamre (2001) method is an updated model for static resistance of the Alm and Hamre (1998), based on the frictional fatigue concept. In the updated soil model the shaft friction reduction (friction fatigue) is taken into account.
In the study of Alm and Hamre (2001) a database of 18 jackups installations with varying soil parameters is used. All 18 installations took place in the North Sea area and it is assumed that all piles behaved unplugged. When the resulting skin friction does not exceed the resistance of the soil at the pile tip, the pile is unplugged. Consequently, the bearing capacity is a combination of the friction forces inside the pile, outside the pile and at the tip.
The original pile driveability prediction model of Alm and Hamre (1998) is developed using back-calculations of driveability studies from North Sea installation data. In the 2001 version, a CPT-based method to address the issue is developed, taking into account the variability and uncertainty in soil parameters. The database contains monopiles from $1.8m$ to $2.7m$ in diameter. Alm and Hamre (2001) have proven the model to give reliable predictions for the variety of North Sea soils database. Below the Alm and Hamre (2001) method is summarized:

Side friction
The general formulation of side friction is given by f_s [kPa]:

$$f_s = f_{s,res} + (f_{si} - s_{s,res})e^{k(d-p)} \tag{2.5}$$

with:

- $f_{s,res}$ is the residual pile side friction [kPa]
- f_{si} is the initial pile side friction [kPa]
- d is the depth to the soil layer [m]
- p is the pile tip penetration [m]

The last part of Equation 2.5 ($e^{k(d-p)}$) represents the friction fatigue in which the shape factor (k) for both clay and sand models is:

$$k = 0.0125 \left(\frac{q_t}{\sigma'_{v0}} \right)^{0.5} \tag{2.6}$$

Here q_t [kN/m^2] is the total cone resistance from the CPT, which is normalized to effective in-situ stress, σ_{v0} [kPa] as shown in Equation 2.6.

For CLAY the initial friction (f_{si}) is determined using CPT sleeve friction (f_s). The residual friction (f_{sres} [kPa]) is a function of the cone resistance (q_t) normalized over the effective vertical stress (σ'_{v0} [kPa]) in the following manner:

$$f_{sres} = 0.004 q_t 8 \left(1 - \frac{0.0025 q_t}{\sigma'_{v0}} \right) \tag{2.7}$$

For SAND the best fit for the residual shaft friction is found to be 20% of the initial shaft friction.

$$f_{sres} = 0.2 f_{si} \tag{2.8}$$

Tip resistance

The piles are considered to be unplugged. Only the resistance from the pile tip area is calculated. The end bearing resistance for CLAY is given by $q_{tip,clay}$ [kPa]:

$$q_{tip,clay} = 0.60 q_t \tag{2.9}$$

The end bearing resistance for SAND is given by $q_{tip,sand}$ [kPa]:

$$q_{tip,sand} = 0.15 q_t \left(\frac{q_t}{\sigma'_{v0}} \right)^{0.2} \tag{2.10}$$

Where q_t is the total cone resistance from the CPT [kPA].

2.5.3. Deformation of scour protection

Looking at the monopile interaction with the scour protection rock, a further zoom-in in the process is made, see Figure 2.9. Due to the force of the monopile acting on the rocks within the scour protection, different responses or combinations of responses are possible. There are four main processes that (might) occur: rotation of rocks, rock breakage, rock protruding the soil and interlocking causing refusal. To the writer's knowledge, in literature, there is a lack of knowledge on this topic. But it is expected that the interaction between rocks and the monopile wall depends on the ratio of wall thickness and rock size.

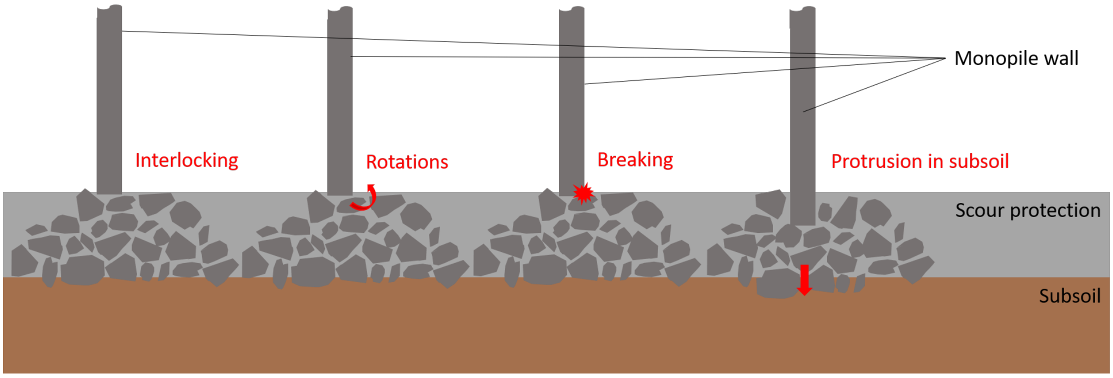

Figure 2.9: Monopile wall and scour protection interactions

Interlocking

The interconnected stability and strength within scour protection can be classified as interlocking, a type of frictional strength within the rocks. The stability of submerged rocks is mainly researched with an eye on stability due to currents or waves, for the design of bed, bank, and shore protection.

Stones start rotating

Depending on the stone size, shape, and wall thickness of the monopile, the rocks of the scour protection could start rotating. This depends on the forces working on the stones and the contact point. The stones will encounter forces from the surrounding stones, possibly from the subsoil, a buoyant force, and the monopile weight. Unfortunately, no prior research has been found on the interaction of the scour protection rocks and the monopile wall. Holeyman et al. (2015) researched the interaction of monopile and boulders. However multiple reasons exist why the work of Holeyman et al. (2015) is not relevant for this research are:

- The interaction focuses on the driving of the monopile using a hammer
- The boulders are surrounded by soil
- The boulder size is $1m$ (scour protection rocks are significantly smaller)

Stones break

The resistance to breaking of armour rocks is separated into two degrees, minor breakage and major breakage. Minor breakage is for example when the corner and edges are broken off due to routine handling. This phenomenon has no significant influence on the PSD. It can however contribute to the roundness of material. Major breakage is referred to when individual armour rocks break along pre-existing defects. The design value D_{n50} might be influenced as a result of major breakage over a significant number of rocks. Armour stone integrity is the resistance to major breakage, basically the ability to withstand breakage during their life cycle. Within the integrity, a differentiation can be made in individual stone integrity and the integrity for amour stone as a granular material. For individual rock integrity, a threshold is determined. This is not available for amour stone as a granular material. (*The Rock Manual*, 2007)

Stones penetrating the soil

No literature is found on this topic. It is expected that this process is depending on multiple factors: the stiffness of subsoil, the force of monopile, and the interactions with other stones.

2.6. Past projects

For the first four Dutch wind farms, different scour mitigation strategies have been adopted. All four projects have scour protection existing of smaller and larger rocks, a filter layer and an armour layer. The four projects differ in the installation and ease of construction. An overview is given in Table 2.1. (Lengkeek et al., 2017) (Netherlands Enterprise Agency, 2015) In the first project Offshore Wind Egmond aan Zee, a dynamic scour protection is designed, resulting in a rock size of about $40cm$ to $45cm$. This rock grade was considered too large to drive the monopile through, therefore the armour rock was installed after the installation of the monopile. Within the Princess Amalia wind farm, experiments have been done in the order of the cable installation, but the monopile is installed before the scour protection as well. A different strategy was applied to the Luchterduinen and GEMINI wind farms, where optimization of the rock size of the armour layer was done. This reduced the cost of the grading itself, but the main advantage is that the monopile was driven through both of the rock layers. Besides the trend toward smaller rocks, in 2017 single grade protection has been used as well. The smaller stability of the rock is often compensated by a thicker layer of rock protection, allowing some winnowing of the seabed sediments through the protection. Using these types of scour protection designs, also the scour protection can be installed prior to the monopile installation. For both the GEMINI and Luchterduinen wind farms limited knowledge is available to the public, specifically regarding monopile installation through the scour protection. (Lengkeek et al., 2017) (Brasseur et al., 2018)

Wind Farm	**Year**	**Applied or estimated rock grades**	**Installation order**
Offshore Wind Egmond aan Zee	2006	Coarse armour grade (60-300kg ND) and 1-3” filter grade	1. Filter layer 2. Monopile 3. Cables 4. Armour layer
Pinsess Amalia Wind Park	2007	Medium coarse armour grade (10-200kg ND) and a coarse filter grade (2-8”)	1. Monopile 2. Scour development 3. Cables 4. Cushion layer (filter) 5. Armour layer
Luchtterduinen	2015	Medium coarse armour grade and 1-3” filter grade	1. Filter layer 2. Armour layer 3. Monopile 4. Cables (with cable protection)
GEMINI	2016/2017	smaller armour grade (D_{50} = ~0.15m ND or HD) and a 1-3” filter grade	1. Filter layer 2. Armour layer 3. Monopile 4. Cables (with cable protection)

Table 2.1: Applied scour protection in Dutch North Sea wind farms; ND and HD refer to normal density and high density rock. (Lengkeek et al., 2017)

By knowledge of the author, no clear limiting rock characteristics for monopile installations are given in literature. From the information above it is shown that the rock size of $40cm$ to $45cm$ was considered too large, however, no scientific background for this is found in literature. Pile penetration through scour protection is a complex process, which is not fully understood.

2.7. Conclusion

In this section sub-question 1 will be answered, the question is:

> **SQ1:** What physical processes can be identified during monopile self-weight penetration through scour protection?

This section is split up into two parts, physical processes and identification of the knowledge gap.

2.7.1. Physical processes

As explained in this chapter monopile installation is an elaborate procedure in which different processes can be identified. Including a fully pre-installed scour protection makes it even more complex. Focusing on phase 2 of the monopile installation sequence (Figure 2.3) the most important physical processes during monopile self-weight penetration are identified using literature:

- The development of tip resistance due to the scour protection layer.
- The development of shaft resistance due to the scour protection layer.
- The self-weight penetration due to the weight and dimensions of the monopile.
- The interaction between the monopile wall and the scour protection rock and inter-rock interaction (interlocking, rotation, breaking, and protrusion of the subsoil).

The complexity of the processes is shown by the interaction between all the different parameters. An overview of the parameters is visualized in Figure 5.7

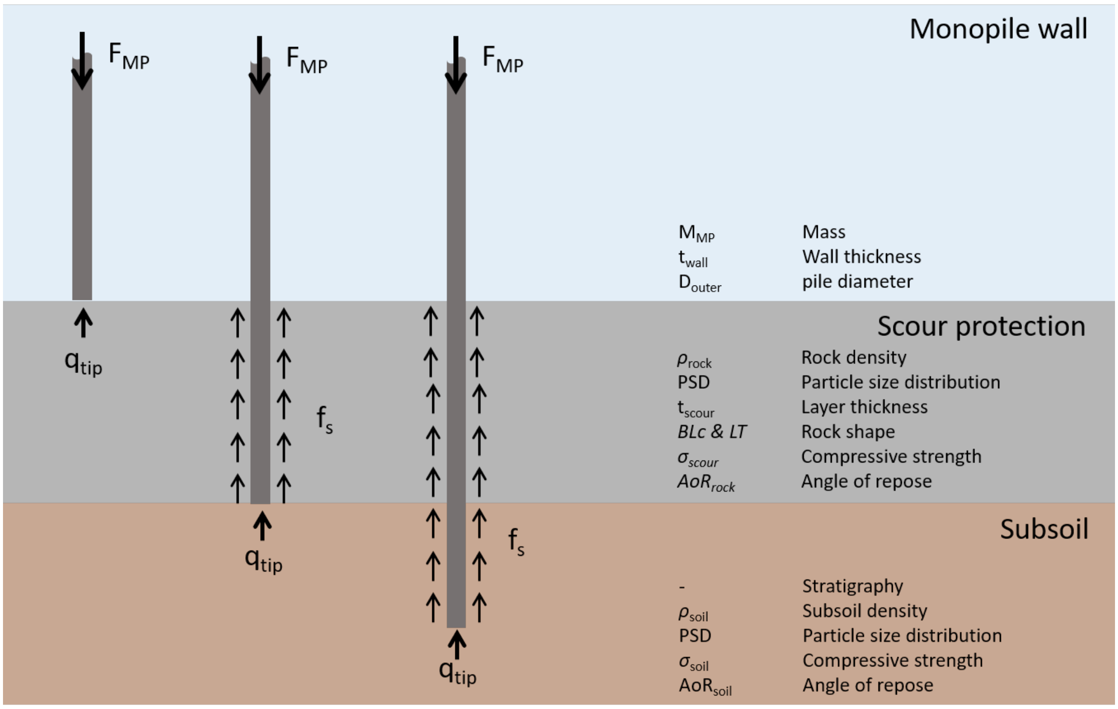

Figure 2.10: Parameter overview monopile penetration

2.7.2. Knowledge gaps

The overall knowledge gap arising from the literature research is: *'What is the technical feasibility of monopile installation through scour protection?'*. In the past, projects with pre-installed scour protection have been executed. However, what difficulties and/or windfalls encountered in the process are unknown.' Besides the rule of thumb introduced in Section 1.1, no prior documentation is found on the limitations on monopile installation through pre-installed scour protection.

3. Modelling method

The literature study in Chapter 2 focuses on the understanding of processes and identifying current knowledge gaps in research. To research the knowledge gaps a modelling approach needs to be selected. What modelling method is suitable for the process of monopile installation through scour protection? For the simulation of the behavior of an engineering component, different methods can be used. For this research, the comparison is made in continuum modelling and discrete modelling, two frequently used methods in geotechnical engineering. Both will be discussed and compared in this chapter. Eventually, an approach is selected to continue the research.

3.1. Continuum modelling

Any material, gas, solid, or liquid is composed of molecules. When looking at materials from a macroscopic point of view, these materials can have deformations, cracks, and discontinuities. Some material properties can be viewed with an uniform effect on the material as a whole. This is the base for continuum mechanics.
Within continuum mechanics, the full space is occupied by the material and it is considered as one mass. The material is presented as one entity, with one single set of parameters. This is represented by partial differential equations. To solve the partial differential equations in two or three space variables, the Finite Element Method can be used. The basic principle of the FEM exists of the idea that the body investigated is subdivided into elements, a finite number of elements in a continuous system. The elements are connected by interconnecting joints, also known as nodes. The complete set of elements and nodes is also referred to as mesh.
Often the field variable is described with the use of a partial differential equation, which is impossible to solve by hand. Assumed is that the variable acts through or over each element in a predefined manner. This assumption may seem a bit of a liberty, but it can come startlingly close to reality. After the discretization of the model, the governing equation for each element is calculated. (Barkanov, 2001)
Continuum mechanics is often used in geotechnical engineering and fluid mechanics. However, can discontinuities, cracks, and differences in molecular structures not be presented.
FEM is commonly used in geotechnical applications. For example in Murphy et al. (2018), where FEM is used for the design of a latterly loaded monopile. The effect of monopile installation on the lateral loading response is investigated by Fan et al. (2021). Similar to the given examples, the majority of the FEM on this topic regards the monopile to be in position already, compared to the installation of the monopile

itself.

3.2. Discrete modelling

The opposite of continuous modeling is discontinuous modeling. At which the discontinuities like cracks or deformations of materials can be taken into account. The next step is discrete modeling, in which the material consists of an assembly of particles and each particle can have unique quantities. Calculations are executed on each individual particle using the Discrete Element Method (DEM). The DEM is used to represent the materials as rigid particles, obeying Newton's law of motion and the interactions by contact laws. The main advantage of using DEM is the ease of handling large displacement and deformation. Therefore is discrete modeling an effective method for addressing engineering problems in granular and discontinuous materials, like rock. DEM can be very computationally intensive because every interaction between individual particles has to be calculated over a specific time period. (Bharadwaj, 2014)
In the past, DEM is used for different applications, varying from grains, fibers, powders to soils. The potential of DEM modeling for pile installation is represented in the paper by Cerfontaine et al. (2021), Tanaka et al. (2000) and Lobo-Guerrero and Vallejo (2007). The three articles mentioned will be shortly discussed and their applicability to this research will be given.

DEM modeling of silent piling group installation for offshore wind turbine foundations (Cerfontaine et al., 2021)

The paper by Cerfontaine et al. (2021) focuses on the silent piling concept, composed of a cluster of four piles. To decrease the number of particles and therefore the computation time, Cerfontaine et al. (2021) used prototype scaling combined with a scaling factor (SF) on the particle size distribution.
The potential of DEM piling analysis is shown within this article. An elaborate analysis of the macroscopic forces and microscopic observation is performed. However, no validation of the DEM model is executed at this point. Moreover, the model focuses on pile driving into a sand subsoil, no rock materials are involved. The simulation set-up is presented in Figure 3.1.

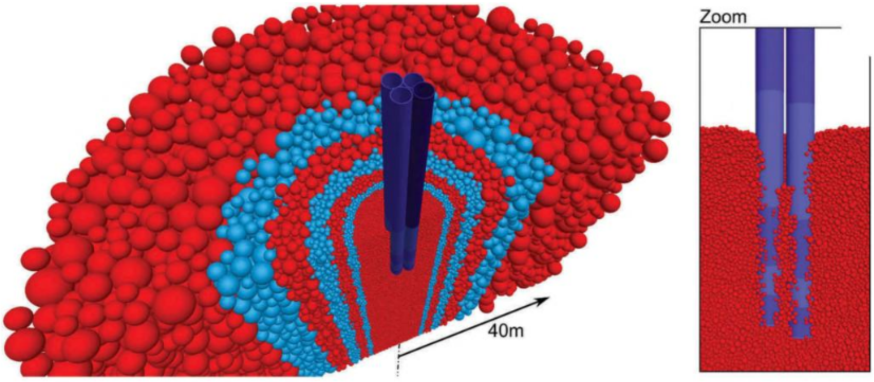

Figure 3.1: Simulation set-up of pile driving simulation by Cerfontaine et al. (2021)

Simulation of soil deformation and resistance at bar penetration by the Distinct Element Method (Tanaka et al., 2000)

Within the article by Tanaka et al. (2000), a bar penetration test was conducted and compared with simulation results. Concluded is that the DEM simulated the discontinuous behavior of the soil well, but that the parameter input plays an important role to make the model useful.

Influence of pile shape and pile interaction on the crushable behavior of granular materials around driven piles: DEM analyses (Lobo-Guerrero & Vallejo, 2007)

The penetration resistance of different pile shapes is investigated in Lobo-Guerrero and Vallejo (2007): flat tip, open pile, and triangular tip. In this article specifically, particle breakage is taken into account. It is shown that the shape significantly influences the development of the penetration resistance. The flat-ended pile induces the highest penetration resistance. The pile with the triangular tip resulted in the lowest penetration resistance. The hollow pile resulted developed a plug during the driving process. No validation of the model is executed.
The pile width is $3cm$, with a wall thickness of $1mm$ and the materials have a radius of $3mm$. This results in a slenderness ratio $t/D = 0.01/3 = 0.0033$. The slenderness ratio deviates significantly from the monopile slenderness ratios of $4 - 8$.

3.3. Comparison of continuum and discrete modelling

In Figure 3.2 a comparison overview of continuum and discrete modelling is presented. Also, hybrid modelling approaches are possible, but due to the complexity of the application, this is outside the scope of this research.

Working with a continuum approach can offer valuable insights. Sinha and Walton (2019) made a comparison within the use of a continuum and discontinuous model for rock support interaction for excavations undergoing stress-induced spelling. Their findings show that continuous modelling can represent part of the behavior, whereas discontinuous models can represent the full behavioral range. A more fundamental understanding of particle interaction and displacement can be achieved using a discontinuous model. A discontinuum modelling approach is concluded to be superior in rock support interaction compared to the continuum modelling approach according to Sinha and Walton (2019).

When it comes to scaling applicability, Sinha and Walton (2019) states that continuum models are more suitable for analyzing large structures. Typically discontinuous approaches are limited to smaller-scale simulations.

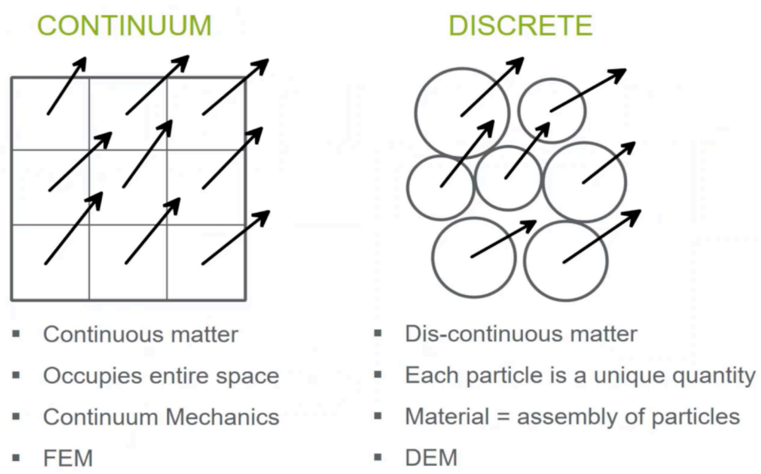

Figure 3.2: Continuum or discrete modelling

3.4. Conclusion

In this section sub-question 2 is answered:

> **SQ2:** What is an adequate numerical modelling method?

For simulating monopile installation through scour protection, continuum and discrete modeling have been compared to find an appropriate modeling method. Due to the computational time of discrete modeling, continuous modeling would be more suitable when it comes to the scale of the process. However, is scour protection not a suitable set-up for continuum analysis. Scour protection is a layer of stones, of different sizes, shapes, etc. This layer thickness is in the order of $2m$ to $3m$ and a diameter in the order of $25m$ diameter. In the built-up of this layer, 5 to 15 stones are located on top of each other. This is not a formation that can be identified as a continuum, therefore is a continuum modeling approach not suitable for researching the interaction between the monopile and the scour protection rocks. Therefore DEM will be used in this research.

4. DEM calibration of Truck Load Simulation

This chapter aims to determine calibrated parameter input to mimic bulk characteristics and the behavior of the scour protection material. To investigate the influence of the input parameters, a Truck Load Simulation is designed. In Section 4.1 the software setup used in this research is presented. Section 4.2 presents the simulation design for the Truck Load Simulation. In Section 4.3 the calibration plan is given, followed by the results in Section 4.4 and a conclusion in Section 4.5.

4.1. Software set-up

For the simulations, the commercial software package Altair EDEM 2021.1 is used. EDEM uses algorithms to simulate and analyze the behavior of granular materials like coal, iron ore, soils, and rock. The software has a user-friendly interface which makes it easy to create, run and analyze DEM simulations. Using EDEM helps to keep focused on the monopile installation process, compared to alternative DEM software. In alternative software the implementation of state-of-the-art DEM technology might be necessary.
Besides the DEM parameters describing the bulk material behavior, EDEM also requires other settings that can significantly influence the results and the computational time. Those parameters are the contact model and the time step. Inadequate input may lead to excessive computational times and/or faulty results. The contact model and time step have to be prescribed in EDEM and are explained below.

4.1.1. Contact models

Inter-particle and particle-geometry interactions are calculated using a contact model, this is a crucial element for DEM simulations. Particle interaction with other particles and boundaries involves three types of motions: normal contact force displacement, tangential contact force displacement and rolling movement (see Figure 4.1). Figure 4.1a. shows the normal contact force, where the contact force is identified using the normal spring stiffness (k_n), the normal damping coefficient (c_n), and the overlap of two contacting spheres (δ_n). Figure 4.1b. shows the tangential contact force, where the contact force is identified using the tangential spring stiffness (k_r), the tangential damping coefficient (c_r), the static friction coefficient (μ_s), and the tangential component of the relative displacement (δ_r). Figure 4.1c. shows the rolling movement, where the rolling movement is identified using the rotational spring stiffness (k_r), the rotational damping coefficient (c_r), the rolling friction coefficient (μ_r), and the rolling overlap (δ_r).

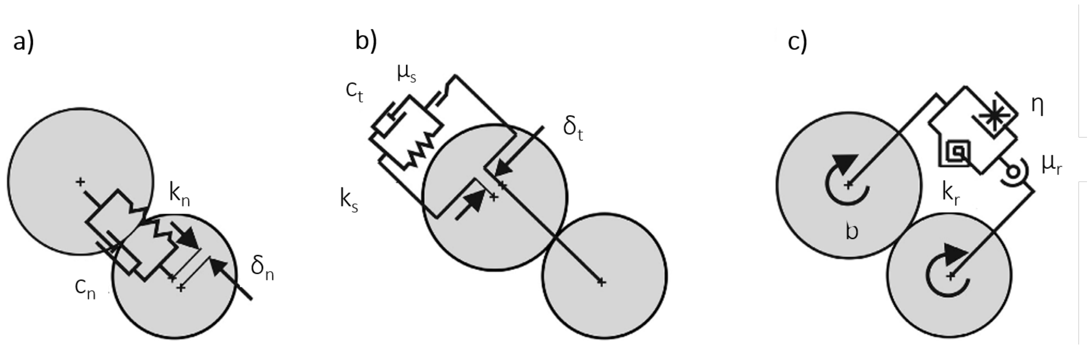

Figure 4.1: Particle contact models for DEM: a) normal contact force displacement, b) tangent contact force displacement, c) rolling movement (This image is modified from: Horabik and Molenda (2016))

Force based displacement

Multiple contact models exist, the first one being the Linear Spring Dashpot model, based on the work of Cundall and Strack (1979). Alternatively, the Hertz-Mindlin contact model is available, within "Altair EDEM 2021.1" (2021). The Hertz-Mindlin contact model is most commonly used and is a non-linear elastic model, very suitable for non-cohesive interactions.
Besides the above-suggested contact models, multiple other contact models are available. These models can be used to incorporate cohesion, plastic deformation, or polyhedral-shaped particles. As those physics are not present in the scope of this research those models will not be further discussed.
The Hertz-Mindlin contact model is the default contact model within EDEM and within this research. This contact model is selected due to its efficient and accurate force calculation according to "Altair EDEM 2021.1" (2021). Within the Hertz-Mindlin contact model both normal contact force displacement, tangent contact force displacement, and rolling movement are included, see Figure 4.1. The full mathematical description can be found in Appendix A

Rolling resistance

Rolling resistance is a restrictive force that slows down the rotational movement of the particles. A rolling friction model is added to compensate for the material resistance to rolling. "Altair EDEM 2021.1" (2021)
The rolling resistance within the interaction can be included in the contact model by using a friction model. Ai et al. (2011) researched four friction models for discrete element simulations. Three of the four researched models are capable to incorporate the dissipation of energy. According to Ai et al. (2011), the stability function is incorporated well in one of the models. With the stability function, Ai et al. (2011) refers to the packing support, so providing stability within a particular system, which is especially important

in the static phase. Friction model C provides stable torques and therefore it is most suitable for the pseudo-static system of this research. Friction model C is defined as an 'Elastic-plastic spring-dashpot model'. The full mathematical description of Friction model C can be found in Appendix A.

4.1.2. Time step

Within the DEM algorithm, it is assumed that within a very short period of time, the acceleration and speed are constant and a single grain disturbance will not reach further than its nearest neighbors. This short period of time is referred to as the time step. New positions are calculated and the algorithm starts again, see Appendix A. (Horabik & Molenda, 2016)

The time step is crucial for DEM simulation. Having a time step that is too small can result in unnecessarily long computational time. While a time step that is too large can result in numerical instability and solutions that are physically impossible, for example exploding simulations. (Burns et al., 2019)

The Rayleigh time step is a method to calculate the critical time step of the simulation. The Rayleigh time step (T_R) is the time it takes for a shear wave to propagate through a solid particle. It depends on the shear modulus in combination with the smallest particle in the simulation, combined with the particle density and Poisson's ratio, see below. ("Altair EDEM 2021.1", 2021)

$$T_R = \frac{\pi R \sqrt{\frac{\rho}{G}}}{0.1631\nu + 0.8766} \tag{4.1}$$

With

- R is the smallest particle radius $[m]$
- ρ is the particle density $[kg/m^3]$
- G is the shear modulus $[Pa]$
- ν is the Poisson's ratio $[-]$

Commonly a fraction of $0.2-0.4$ of the T_R is used as the time step. A time step of $0.2T_R$ was also used at the start of these simulations as well. As the ρ, G, and R deviate per simulation, the T_R and the time step also deviate per simulation.

While executing the simulations the stability of the simulation was questionable when using a time step of $0.2T_R$. The particles kept on rolling and no stable material configuration was reached. A conservative decision is made to ensure the stability of the simulation. A time step of $1*10^{-5}$ s is used, this is a fraction of 0.02 of the Rayleigh time step. Within these simulations a stable material configuration was reached, resulting in more reliable model output.

4.2. Simulation design

To calibrate the bulk behavior of the scour protection material, a simulation is designed. This simulation is referred to as the Truck Load Simulation. Limited knowledge about the scour protection behavior is available and within the scope of this research, no laboratory or field experiments are executed. In Appendix B, the available information of the bulk materials is presented.

4.2.1. Particle shape

Within the simulation particles representing the scour protection rock are needed. The shape of rock particles is an unknown characteristic of the scour protection material. Within EDEM (multi-)spherical or polyhedral particle shapes can be incorporated into the simulation. The (multi-) spherical particles can be generated and manually adapted within EDEM. Polyhedral particle shapes can be imported into EDEM. Using multi-spherical or polyhedral particles will increase the computational time since more contact points are present and therefore more calculations are needed. Combining the extensive computational time with the unknown shape parameters of the scour protection rock, decided is to use spherical particles. The decision to use spherical particles is justified by including rolling friction in the DEM simulation (Wensrich & Katterfeld, 2012) .
According to Qu et al. (2022), DEM simulations with either spherical or irregular-shaped particles are capable of properly reproducing the stress behavior of granular material. Within the article of Qu et al. (2022), the irregular-shaped particles consisted of two clumped spherical particles. Including the rolling friction in the DEM simulation recreates the shape-induced behavior, like interlocking. (Wensrich & Katterfeld, 2012)

4.2.2. Particle generation

Different options for particle generation exist and are tested. A static or dynamic factory can be implemented. A static factory is a geometry, that is filled with particles at a specified time step. While a dynamic factory is a plate that generates particles over a certain amount of time. A dynamic factory can be assigned a certain speed in any direction, this is referred to as a moving dynamic factory.
Different factory types can influence among other things the particle size distribution (PSD). The PSD input settings are consistent with the particle size distribution from the scour protection rock, see Appendix B. The three factory settings are tested to verify the PSD output. The results in Figure 4.2 show that the moving dynamic factory generates a PSD comparable to the PSD input. Therefore a moving dynamic factory will be used in the simulations.

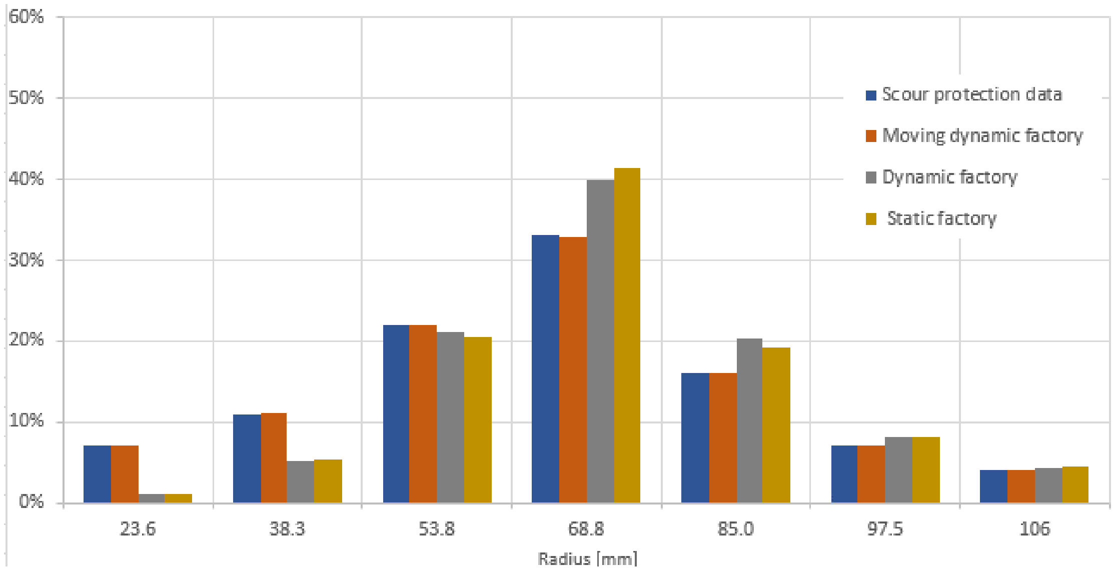

Figure 4.2: Particle size distribution output while changing the factory type

4.2.3. Key Performance Indicators (KPIs)

Two Key Performance Indicators (KPIs) of the bulk material behavior are investigated using the Truck Load Simulation. The KPIs are the porosity of the bulk material and the angle of repose (AoR).

Porosity

The porosity of the material is a characteristic parameter to describe the bulk behavior. The bulk density, void ratio, and porosity are all a measure focusing on the amount of solid material and voids within bulk materials. The porosity (n) is determined using the following formula:

$$n = \frac{V_v}{V_t} \tag{4.2}$$

Where V_v and V_t represent the void volume and total volume. Filling out this formula with the data from the case study presented in Appendix B, results in a target porosity value of $n = \frac{651}{1414} = 0.46$.

Within EDEM the voidage of a predefined bin can be obtained, the voidage is determined using the following formula (“Altair EDEM 2021.1”, 2021):

$$Voidage = \frac{V_{bin} - V_{particles}}{V_{bin}} * 100 \tag{4.3}$$

The V_{bin} is equal to the V_{total} of a pre-described bin. And the $V_{bin} - V_{particles}$ is equal to the V_{void} of the material. Therefore a factor of 100 is the difference between the $Voidage$

output of EDEM and the n from field experiments. The $Voidage$ output of EDEM will be divided by 100 to create a fair comparison.

Angle of Repose (AoR)

The angle of repose (AoR) describes the steepest angle under which a stack of bulk material is stably positioned on a horizontal plane. The AoR is included as a KPI because it characterizes the inter particle frictional resistance to movement. (Amidon et al., 2017) The AoR for bulk materials in DEM is characterized by the static and rolling friction of the particles. Including the AoR in the calibration can therefore significantly contribute to generating the desired behavioral description of the bulk material. Within the available data on the scour protection material, no AoR is present. Therefore, the target value of the AoR is determined using the approach of Froehlich (2011), this approach is elaborately discussed in Appendix D. With experimental data from 25 stockpiles located at quarries, Froehlich (2011) created a formula to calculate the estimated angle of repose. For the case study this results in a target value of 38 °, see Appendix D. According to Froehlich (2011), the AoR of rock materials is not changing significantly when submerged.
Within the Truck Load Simulation, a slice of material is extracted from the generated pile. The angle under which this slice of material is positioned is measured using Matlab. This angle is compared to the target value of the AoR.

4.2.4. Simulation set-up

The angular rock stockpiles considered by Froehlich (2011), were used to determine the target value of the AoR. The experimental setup is recreated in the simulation. Of the 25 stockpiles considered by Froehlich (2011), 19 stockpiles are deposited from a truck or a front-end loader and 6 are deposited from a conveyor belt. As the majority of the stockpiles are created by rock deposition from a truck, the simulation set-up represents a deposition from a truck.
The dimensions from the Truck Load container are $3 * 3 * 6m^3$ and in total $15000kg$ is generated. The size is simplified from truck containers, which are slightly smaller, namely $2.43 * 2.59 * 6.06m^3$.
In Figure 4.3, the design of the Truck Load simulation is presented in 4 phases: a,b,c and d. In phase a. the container is empty. Within phase b the container is filled with bulk materials. The particles are generated using a dynamic factory, sized $2.8 * 5m^2$. The factory starts $20cm$ above the bottom plate of the container and moves upward with a speed of $1m/s$. Afterward, it is moved upward and turned sideways to deposit the materials on the floor in phase c. Phase d shows the situation where all the material is positioned in stockpiles. Within these stockpiles, the porosity and angle of repose are measured.

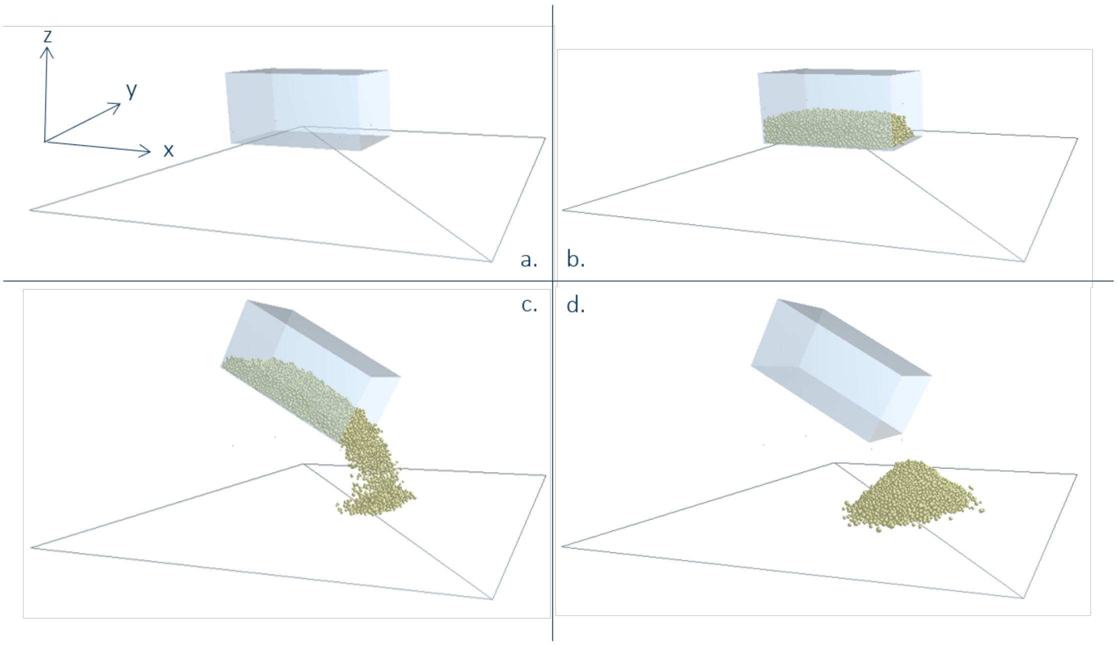

Figure 4.3: Truck Load Simulation design

4.3. Simulation plan for calibration

To reach the target values of the KPIs in the bulk material, the DEM input parameters need to be adjusted until the predicted bulk behavior is reached. When using trial and error the number of simulations required is difficult to determine beforehand. The DEM input parameters need to be changed one parameter at a time and when the number of calibration parameters increases, the method becomes less feasible. To reduce the number of simulations while finding an adequate input set, the Design of Experiments (DoE) method is used. The DoE method will be explained in this section, followed by the DoE plan for the Truck Load Simulation. (Zhou et al., 2018)

4.3.1. Design of Experiments

The influence of individual parameters and the influence of combinations of parameters can be tracked using the Design of Experiments method (DoE). During DoE, i initial parameter sets are generated forming a matrix. Each set contains N parameter values. The initial set of parameters is referred to as $X = x_1, \ldots, x_i$. The simulations are run and the results $y'_i = y'_1, \ldots, y'_M$ can be calculated. The results are compared to the calibration targets. N_s is the number of variable input parameters and N_y is the number of calibration targets. (Richter et al., 2020) (Zhou et al., 2018)

4.3.2. Simulations

Within the simulation, parameter input values need to be defined. A distinction is made between fixed and variable parameters input. The fixed parameters are kept constant, while the variable parameters are varied within the calibration. The DoE method is executed using 5 variable input parameters, each with an upper and lower value, and no in-between values are used, to keep the number of simulations limited. This results in $2^5 = 32$ simulations. Below are the 2 fixed parameters and 5 variable input parameters described.

Fixed parameters

Coefficient of restitution
The coefficient of restitution represents the ratio between velocity before and after the collision. For the scour protection rocks is expected that there will barely be any velocity after collision, therefore the coefficient of restitution is set at 0.02.

Poisson's ratio
The Poisson's ratio is a material constant, representing the ratio of transversal elongation over the axial compression. Values between 0.2 and 0.3 are commonly used in DEM simulation, for this simulation the Poisson's ratio (ν) is 0.25. This value is consistent with Poisson's ratio used for granite gneiss in Ji et al. (2018) and for gravel in Elskamp et al. (2017). Granite gneiss is the rock material used for the scour protection in the case study.

Variable input parameters

Five parameters have a variable input, expected is that they contribute noticeably to the bulk behavior. A differentiation is made within the type of parameter: continuous and categorical. The concept of continuous and categorical input parameters is introduced by Mohajeri et al. (2021). This differentiation is made for the calibration process later. Continuous type DEM parameters are numerical and have an infinite number of values between two values, for example, the rolling friction coefficient. Categorical type variables have a finite number of categories or groups, for example, the shape of particles or the number of bins within the particle size distribution.

Coefficient of static friction
Static friction, also known as Coulomb friction, represents the friction between two particles. Static friction prevents a particle from sliding down a slope. The static friction coefficient is a scalar value. And used to determine how much force is required, before an object in rest can be put into motion. (*EDEM2.4 user guide*, 2011)
Within Li et al. (2018) different types of granite are researched using DEM, within this research, intergranular friction for the three types of granite is used. The values range from 0.43 to 0.8. This range is the basis for the static friction values in the simulation. The input values for the coefficient of static friction (μ_s) are:

- 0.4
- 0.9

Coefficient of rolling friction
The rolling friction (μ_r) is important due to two reasons. Firstly, it recreates the dissipation of energy during rotation. Secondly, the rolling resistance also provides packing stability in a pseudo-static system. Meaning that among other things the rolling friction will compensate for the assumed spherical shape of the particles.
In Wensrich and Katterfeld (2012) the μ_r is analyzed in relation to the shape of the particle and the resulting AoR. When using spherical particles and having a target AoR value of 38°, an μ_r above 0.4 is shown to give credible results. Therefore a value of 0.4 is used.
Within the research of Wensrich and Katterfeld (2012), the highest μ_r is 0.8, within some experiments this did not result in an AoR above 35° for the spherical particles. As the target value of the AoR is 38°, ot is decided to use an upper value higher than 0.8, namely 0.9.

- 0.4
- 0.9

Particle density
The particle density of the scour protection is given in the density test of the scour protection material in Appendix B. The solid particle density (ρ_s) is equal to 2650 kg/m^3. As the process takes place below water an alternative value of the density is also tested, the buoyant density (ρ') of the particles is 1625 kg/m^3, see Appendix B.

- 1625 kg/m^3 (ρ')
- 2650 kg/m^3 (ρ_s)

Particle size distribution (PSD)
The PSD of the scour protection is given in Appendix B, it consists of 7 particle bins plus 1 empty bin. Within EDEM the smallest particle has a significant influence on the computational time of the simulation. Due to a large number of particles needed, a limitation of the particle sizes included is suggested to reduce the computational time. Therefore it is investigated what the influence of the smallest three particle bins is on the KPIs. It should be noted that bin 1 is empty. Two options are investigated:

- 7bins: sieve number 2 until and including sieve number 8 (see Appendix B)
- 5bins: sieve number 4 until and including sieve number 8 (see Appendix B)

Shear modulus
The shear modulus of the material is a measure of the stiffness of the material, how the materials deform under a certain load. The stiffness of the materials has a significant effect on the computational time of the simulation. The shear modulus is not expected

to have a significant influence on the KPIs. However, there are lower shear modulus values used to decrease the effect on the computational time.
In Lommen et al. (2014) the relationship between the penetration resistance and the shear modulus in a DEM simulation is researched. Within Lommen et al. (2014) an AoR test has shown that a shear modulus of $1 * 10^7\ Pa$ is the lowest value, for which the results are not altered. The upper three tested shear modulus values show a trend towards similar penetration resistance. Decided is to use the lowest of those three values, to decrease the computational time. This results in an upper shear modulus value of $1 * 10^8\ Pa$. The shear modulus values used are:

- $1 * 10^7\ Pa$
- $1 * 10^8\ Pa$

Overview
In Table 4.1 an overview of the input parameters is shown. For the complete overview of the 32 simulations, a reference is made to Appendix E. The differentiation between continuous and categorical input parameters is made for later in the calibration process. Another set of input parameters is included in the research. This is a manually generated input set, see Table 4.2.

Variable input parameters			Low	High	Continuum/ Categorical
1	Coefficient of static friction	$\mu_s\ [-]$	0.4	0.9	Continuum
2	Coefficient of rolling friction	$\mu_r\ [-]$	0.4	0.9	Continuum
3	Particle density	$\rho\ [kg/m]$	1625	2650	Categorical
4	Particle size distribution	PSD	5 bins	7 bins	Categorical
5	Shear modulus	$G\ [Pa]$	$1 * 10^7$	$1 * 10^8$	Continuum

Table 4.1: Overview of the variable input parameters of the Truck Load Simulation

Reference	PSD	ρ $[kg/m^3]$	μ_s $[-]$	μ_r $[-]$	$G\ [Pa]$
Set5	5bins	1625	0.5	0.5	$1 * 10^8$

Table 4.2: Manually generated parameters input sets

4.4. Results

The simulation results are divided into 4 subgroups, combining the 2 categorical parameters:

- PSD with 5 bins & $\rho' = 1625 kg/m^3$

- PSD with 5 bins & $\rho_s = 2650 kg/m^3$
- PSD with 7 bins & $\rho' = 1625 kg/m^3$
- PSD with 7 bins & $\rho_s = 2650 kg/m^3$

The outcomes of the simulations are presented in Figure 4.4 for the static friction, in Figure 4.5 for the rolling friction, and in Figure 4.6 for the shear modulus. All simulations are presented in each of the figures, however, the dependency of the variable parameters can be observed within the different plots. A smaller scatter within the data points, represents a larger dependency on the specific parameter.

Both target values are well within the range of the result data. The target value of the porosity is 0.46. The simulation outcomes vary around the target value, within a range of 0.38 and 0.50. The target value of the AoR is 38°. The simulation outcomes vary around the target value, within a range of 34° and 48°.

Coefficient of static friction

Within Figure 4.4 is shown that a porosity of 0.46 cannot be reached with a μ_s of 0.4. And for the 7bin PSD, the target value of the porosity can neither be reached when μ_s is 0.9. For the static friction coefficient, a narrow scatter is presented for the porosity of the bulk materials. This reflects a larger dependence of the μ_s on the porosity. For the AoR in the right figure, a wider scatter around the target value is presented for the upper and lower value of μ_s.

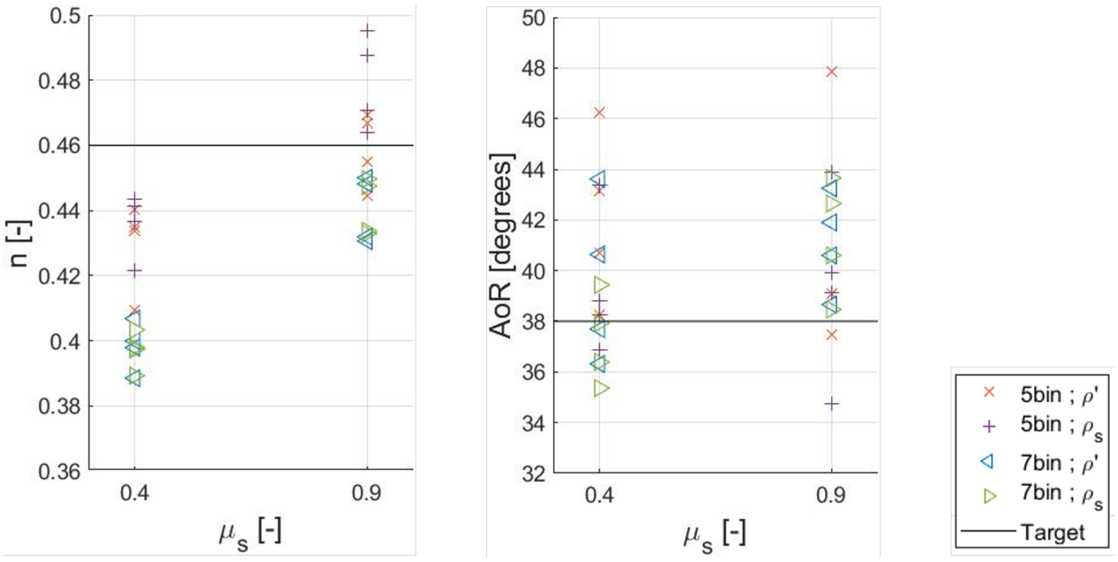

Figure 4.4: Influence of coefficient of static friction (μ_s) on bulk behavior

Coefficient of rolling friction

The coefficient of rolling friction is presented in Figure 4.5, a smaller scatter within the AoR is represented. This reflects a larger dependence of the μ_r on the AoR. Within the porosity plot for the 7bin PSD, the data do not cover the target value, this is the case for both $\mu_r = 0.4$ and $\mu_r = 0.9$.

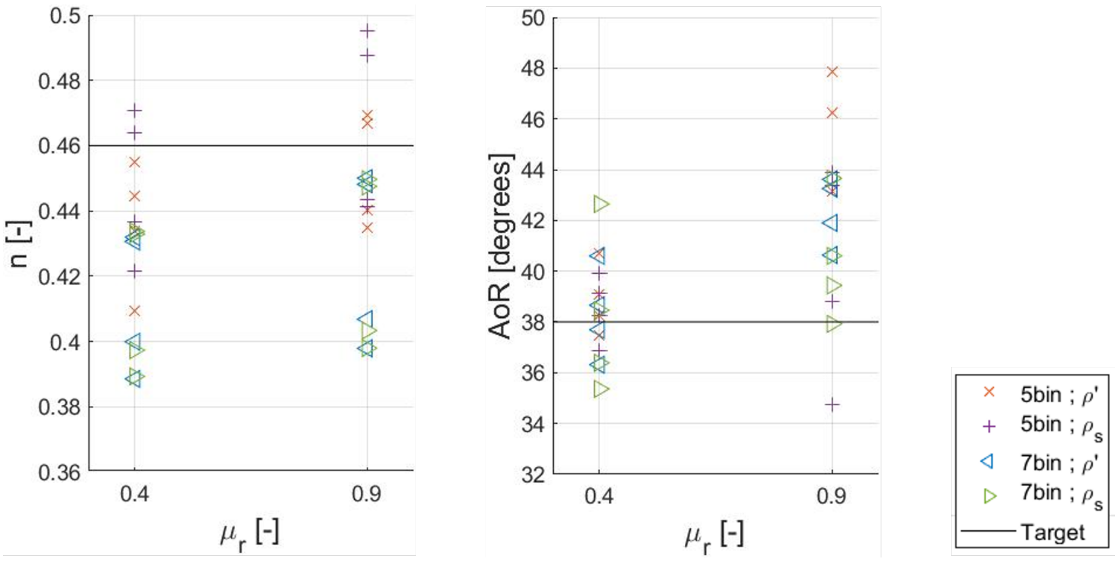

Figure 4.5: Influence of coefficient of static friction (μ_s) on bulk behavior

Shear modulus

For the shear modulus, the largest scatter in both the porosity and AoR is observed. Meaning that KPI performance is less dependent on the shear modulus input.

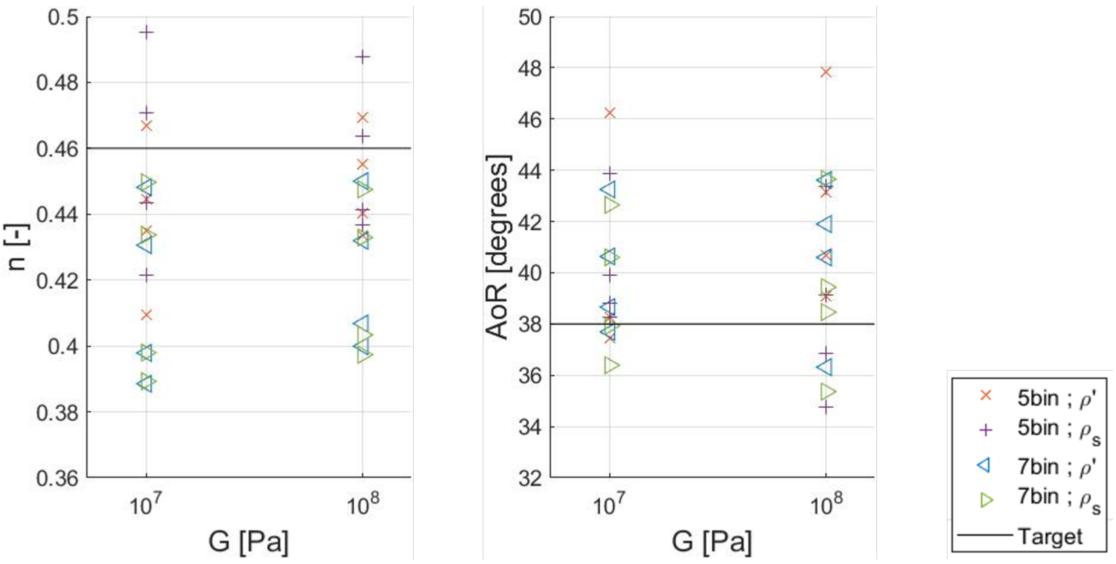

Figure 4.6: Influence of coefficient of static friction (μ_s) on bulk behavior

Consistently with EDEM (2019), the data presents that the μ_s and μ_r are the most influential DEM parameters for the AoR calibration. However, is an optimal set of input parameters not identified from the presented data at this point. Therefore further steps in the calibration process need to be taken.

4.4.1. Optimization method

As suggested by Mohajeri et al. (2021) optimization methods can be applied to calibrate the continuous DEM input parameters. According to Richter et al. (2020) surrogate modeling-based methods are promising for DEM calibration for continuous parameters.

Surrogate modeling-based optimization

Within surrogate modeling based optimization, the parameter space is searched to approximate the target values. The surrogate model, F(x) maps the relationship between the DEM input variables and the calibration targets. Three different regression models are tested:

- Linear Regression
- Gaussian Process Regression
- Linear Support Vector Machine Kernel

A coefficient of determination R^2 is used to assess the predictive quality of the surrogate model:

$$R^2 = 1 - \frac{\sum_{i=1}^{N_s}(y_i - \hat{y}_i)^2}{\sum_{i=1}^{N_s}(y_i - \bar{y}_i)^2} \tag{4.4}$$

With:

- y_i is the observed value
- $\hat{y}_i$ is the corresponding predicted value
- $\bar{y}$ is the mean of the observed values

Consistent to Mohajeri et al. (2021), a minimum R^2 value of 0.75 is considered to represent a well-working surrogate model. If the R^2 is below 0.75, either a higher number of input training samples is required or a more advanced surrogate model.

The linear regression model was the evident most suitable surrogate model, based on the R^2 values. The linear regression model is the most commonly used regression model. Within the surrogate model, the desired calibration targets can be found using an optimization method.

Genetic Algorithms

A specific optimization method is a Genetic Algorithm (GA). As within DEM simulation generally more than one KPI is considered, it is a multi-objective optimization problem. The GA overcomes the problems that arise when a multi-objective optimization is required compared to a single-objective optimization. (Do et al., 2018)
A genetic algorithm is a method for searching and optimization, inspired by Charles Darwin's theory of natural evolution. The algorithm reflects the natural selection process, using selection, crossover, and mutation. In the first phase, a population is randomly generated. During the next phase, techniques are used to select the next generation. The selection phase is of importance as it determines the significance of the convergence. The better fit of an individual, the larger the probability of survival and mating. Crossover mimics the process of generating new offspring, were a mix of the parents gene is generated. The selected individuals are mated in pairs using a single point crossover. To promote genetic diversity in the current population, mutations are used. Comparable to biological mutations, one or more gene values are randomly altered. (Do et al., 2018)

4.4.2. Parameter input sets

The parameter sets are generated while keeping the categorical input fixed. So the results are organized into 4 sets:

- PSD with 5 bins & ρ'
- PSD with 5 bins & ρ_s
- PSD with 7 bins & ρ'
- PSD with 7 bins & ρ_s

With the help of a linear regression model and the GA, the optimized values of μ_s, μ_r and G are generated for each set.

In Table 4.3 the sets are presented, including the R^2-values of the linear regression models. For all the R^2-values of the porosity, a satisfactory fit is found. For the angle or

repose, the R^2-value of Set2 and Set4 appear to be a less pleasing fits. For Set4, the deviation is rather small, however, the value for Set2 of 0.17 is significantly lower. This means that finding a fit for the given data points was not successfully reached, using linear regression. This can mean that more input is needed or that the linear regression is not a good fit.
The R^2-value is a good indication that the parameter set will give reliable results, however, the input of the model is limited. Therefore the correctness of the input sets is questionable. The next step is to verify if the sets are presenting calibrated input sets.

	Categorical parameters input		Continuum parameters GA-output			R^2 values of KPIs	
Reference	PSD	ρ $[kg/m^3]$	μ_s $[-]$	μ_r $[-]$	G $[Pa]$	Porosity	AoR
Set1	5bins	1625	0.896	0.405	$9.9 * 10^7$	0.95	0.80
Set2	5bins	2650	0.858	0.420	$9.0 * 10^7$	0.95	0.17
Set3	7bins	1625	0.898	0.400	$8.7 * 10^7$	0.98	0.79
Set4	7bins	2650	0.857	0.403	$9.5 * 10^7$	0.98	0.73

Table 4.3: Parameters input sets

To verify the parameter input sets, extra simulations with the calibrated input sets are run. The results are presented in Table 4.4. Besides the porosity and the angle of repose, the relative error from the target values of the KPIs is included. The relative error is determined using the following formula:

$$error = \frac{x_{output}}{x_{target}} * 100\% \tag{4.5}$$

Where x_{output} is the KPI outcome of the simulation and x_{target} is the target value of the KPI.
As shown in Table 4.4, the relative error is below 7% for all sets, therefore all input sets are considered suitable for further simulations. Also, the suitability of the linear regression model together with the genetic algorithm is confirmed for the DEM calibration problem. For set3 and set4 the relative error of the porosity is higher compared to the other sets. This is consistent with the finding that reaching a porosity close to the target value is more difficult to achieve when using the 7bins within the particle size distribution instead of the 5bins.

Reference		EDEM output porosity n [$-$]	EDEM output AoR ϕ [°]	error porosity	error AoR
Target value		0.46	38		
Set1	= sim18	0.46	39	1%	3%
Set2	=sim13	0.44	39	4%	2%
Set3	=sim20	0.43	41	6%	7%
Set4	=sim24	0.43	38	6%	1%
Set5	=sim33	0.44	39	4%	2%

Table 4.4: Verify input parameters sets

4.5. Conclusion

In this chapter, bulk material behavior is calibrated using two KPIs, the porosity and the angle of repose. The calibration is executed using the Truck Load Simulation as introduced in Section 4.2. Combining the Design of Experiments method with a linear regression model and genetic algorithm provides the answer for sub-question 3.

> **SQ3:** What are appropriate parameter input sets for the bulk behavior of the scour protection?

This chapter shows that multiple parameter input sets exist to generate the desired bulk behavior of scour protection, focusing on the porosity and angle of repose. The final parameter input sets are presented in Table 4.3 and Table 4.2. The relative error presented in Table 4.4, shows no error above 7%. Therefore, all sets are appropriate input sets for further simulations.

5. Full-Scale Monopile Simulation

Due to the novelty of the full-scale DEM monopile simulation, uncertainties exist regarding the domain size and simulation characteristics. During the process of creating the simulation, optimization has to be found in accuracy and computational time.
Within this chapter, a case study is introduced and translated into a reference simulation in EDEM, see Section 5.2. To investigate the influence of multiple simulation input values, an experimental design is introduced in Section 5.3. The experiment results are given in Section 5.4. Within the last section, Section 5.5, the chapter will be concluded by answering the fourth sub-question.

5.1. Software settings

For the following simulations, the commercial software package Altair EDEM 2021.2 is used. This software package is an update from the previously used package in Chapter 4. Using this updated software package, allowed including a GPU CUDA Solver. The GPU CUDA Solver can do calculations across literally thousands of processing cores and therefore delivers results many times faster than the desktop CPUs. ("Altair EDEM 2021.1", 2021)

5.1.1. Contact model

Within this simulation, the same contact models are used as in Chapter 4, a Hertz-Mindlin contact model with Friction model C.

5.1.2. Time step

Consistently with Chapter 4, a time step of $1 * 10^{-5}$ s is used. While using input set5 (Section 4.4), the Rayleigh time step is $5.7464 * 10^{-4}$ s. So the time step is about $0.02 T_R$. In later simulations, different time steps are investigated.

5.2. Simulation design

The design of the Full-Scale Monopile Simulation is presented in this section. The section will be split up into two parts: 1) the introduction of the case study and 2) the EDEM input settings.

5.2.1. Case study

The case study is based on data from practice. In the current research, only one data set is used.

Monopile dimensions

The outer tip diameter of the monopile ($D_{MP,tip}$) is $8m$ with a wall thickness ($t_{MP,tip}$) of $0.08m$. The mass of the monopile (m_{MP}) is $775ton$. More details of the monopile are available, however, they are irrelevant for this research.

Scour protection design

The information about the scour protection material is discussed in Chapter 4 and the available information is shown in Appendix B. To present the layout of the scour protection, a cross-sectional drawing of the design is shown in Figure 5.1. The parameters and the corresponding values for the case study are:

- The thickness of the bottom layer: $T_{BOT} = 1.0m$
- The total thickness: $T_{TOT} = 1.5m$
- The diameter of the top layer: $D_{TOP} = 26.8m$
- The diameter of the bottom layer inline with the current: $D_{BOT,inline} = 33.7m$

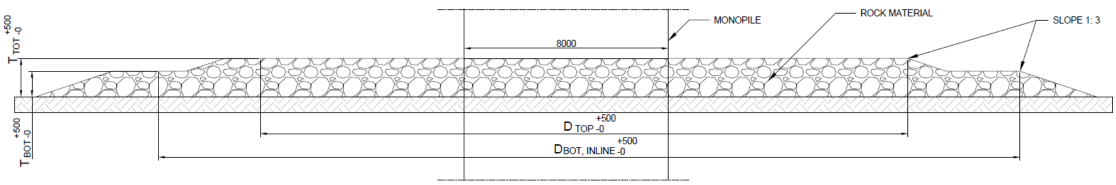

Figure 5.1: Cross-sectional drawing of scour protection design

A tolerance of $0.5m$ is accepted during the installation of the scour protection. This means that the maximum height is $2m$. After the installation, the heights of the scour protection is measured every 10° of the circumference and stored in the as-built documentation. In Figure 5.2 a measurement of the as-built data of the case study is presented. In this graph, the x-axis represents the depth, where $-21.4m$ is the seabed. And the y-axis represents the distance, where $0m$ is the midpoint of the monopile (not installed at the time of measuring). Within this image, the blue line represents the seabed and the green lines the upper and lower bounds of the scour protection design. And the red line represents the height of the installed scour protection. In this example and within the case study, the red line fits well within the ranges and is the upper bound of $2m$ not crossed.

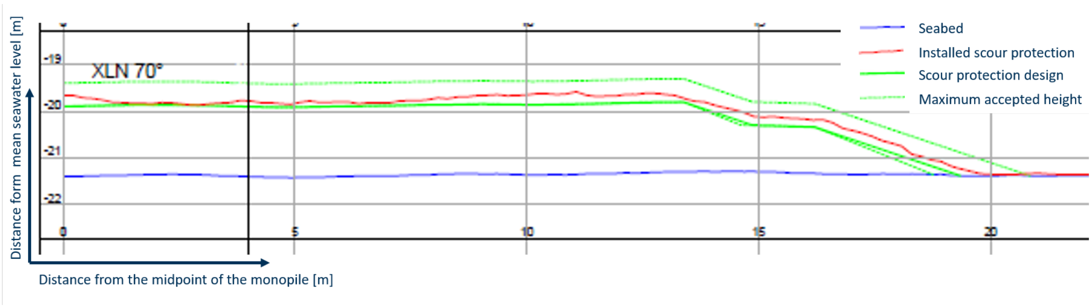

Figure 5.2: As-built measurement at XLN 70°

Monopile installation data

During the installation of a monopile, constant monitoring is executed, additional measurements are executed and recorded. For example, the inclination of the monopile and the loads in the crane can be measured and recorded during installation. What exactly is measured, depends on the project and agreements between the contractor and the client.
In the case study, the penetration time and the crane hook loads are recorded for multiple monopile installations. The penetration over time of the case study is presented in Figure 5.3. A chaotic part is identified near the top of the scour protection layer. From $z = 1m$ a constant penetration is observed.

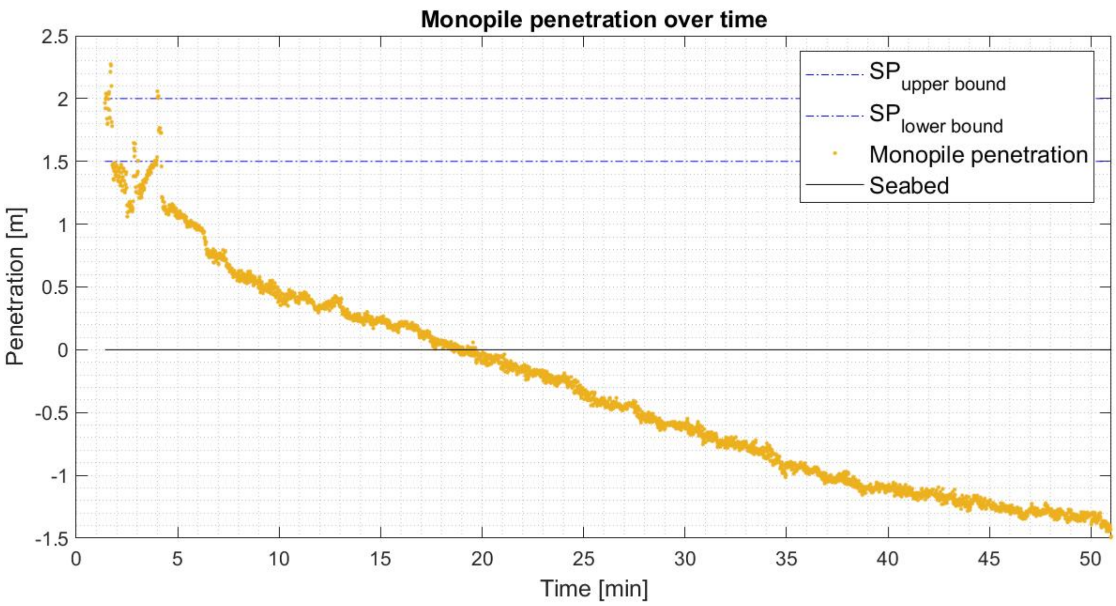

Figure 5.3: Monopile penetration over time

The crane hook loads (F_c) are especially valuable since the load working on the scour protection can be derived from this. As the mass and submerged volume are also known,

the gravitational force (F_g) and buoyancy force (F_b) can be calculated.
The gravitational force is presented in Equation 5.1.

$$F_g = m_{MP} * g \tag{5.1}$$

With m_{MP} the mass of the monopile in $[kg]$ and g the gravitational constant, which is $9.81 m/s^2$. F_g works in the negative z-direction. The buoyant force is presented in Equation 5.2.

$$F_b = \rho_{sw} * g * \Delta \tag{5.2}$$

Where ρ_{sw} is the seawater density, which is $1.025 kg/m^3$, and Δ is the submerged volume of the monopile $[m^3]$. F_b works in the positive z-direction.
This results in a total force working on the scour protection (F_{gbc}) as shown in Equation 5.3.

$$F_{gbc} = F_g + F_b + F_c \tag{5.3}$$

The forces for the case study are presented in Figure 5.4. Included in this graph is a fitted line to the data points of F_{gbc}, named $F_{gbc,fit}$

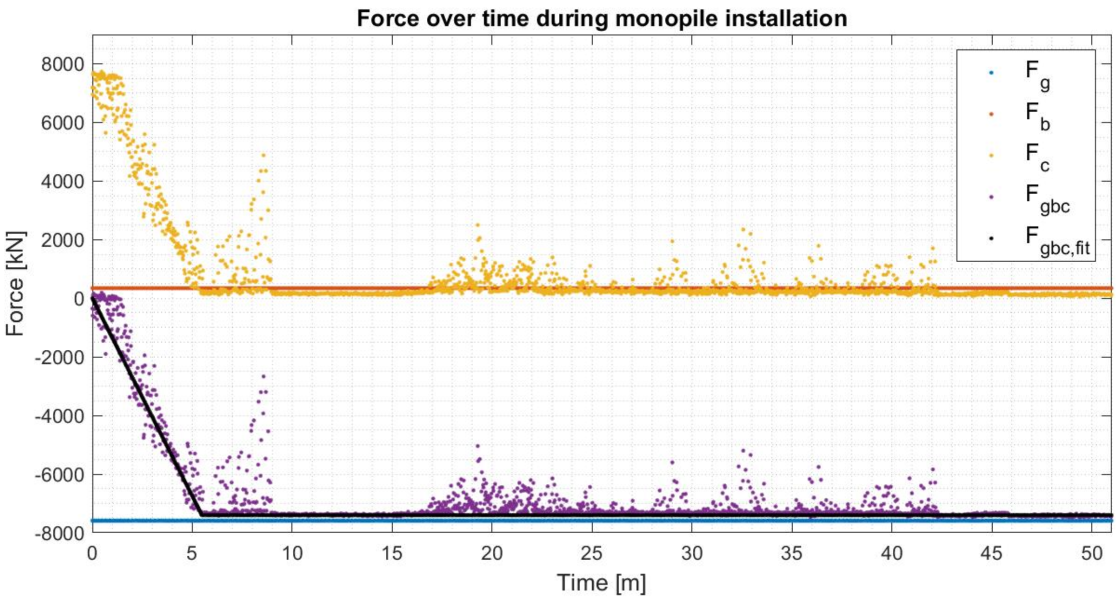

Figure 5.4: Forces during monopile installation

Cone Penetration Test CPT

At the installation site, cone penetration tests (CPT) have been executed prior to the project execution. The upper $10m$ of the CPT is presented in Figure 5.5, the full CPT has a length of $50m$. Within the CPT the cone resistance, q_c $[MPa]$ and sleeve friction f_c $[MPa]$ are measured. From these two parameters, different relations can be identified, these relations are indicated by the parameters shown in Figure 5.5. Not all relations

and parameters will be explained, more information about the different relations can be found in Lunne et al. (1997).
An example of a correlation is the soil behavior type index I_c $[-]$, this indicates the type of soil. The type of soil is visually presented in the left two charts. Two different correlations are used, in chart one is the correlation of Robertson (2009), and in chart two the correlation is defined by Ramsey (2002). Both charts agree that the soil presented is sand, either *clean sand to silty sand* or *gravely sand to sand*.
The last column shows ϕ $[°]$, which represents the angle of repose (AoR). Within the first half meter, the AoR increases rapidly. This can be explained by the mixture of sand and water, present near the seabed. An angle of repose of the upper layer of the subsoil is between $40°$ and $50°$. This represents stiff soil.
The penultimate column presents the relative density D_r $[\%]$. Again within the upper half meter deviating results are observed, due to the water soil substance near the seabed. A high relative density is presented in the graph, leaning towards 100% this represents again a stiff soil.

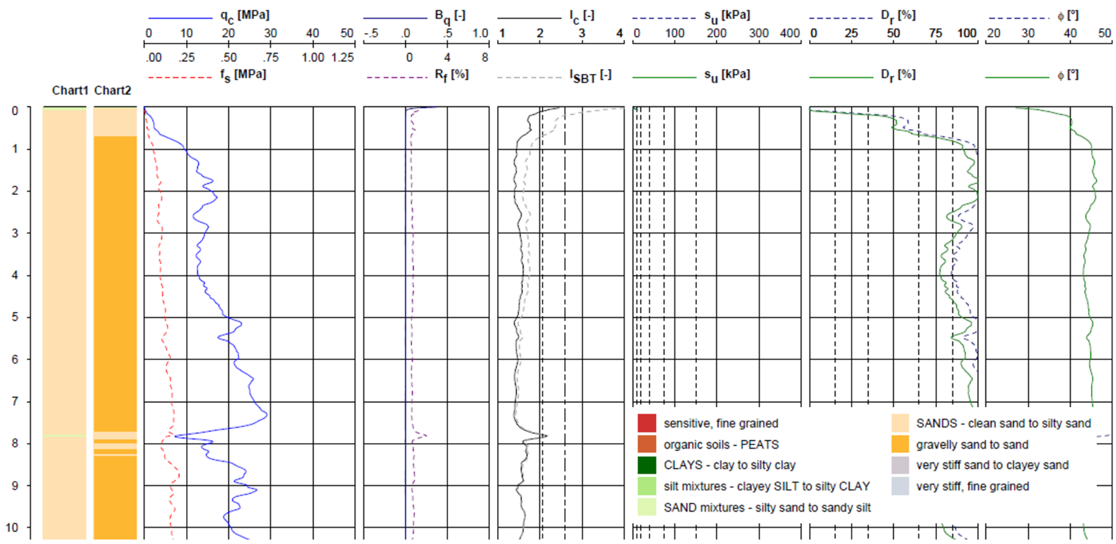

Figure 5.5: Cone penetration data

5.2.2. EDEM input settings

Now the case study is presented, a translation to the DEM simulation will be given.

Particle generation

The particle generation is consistent with Chapter 4, a dynamic factory moving upward with a speed of $1m/s$. The material bed is composed of material blocks of $3 * 3m^2$. The material block is generated in a separate simulation, within this simulation the material block settles for $10s$. Afterward, it is transferred into the Full-Scale Monopile

Simulation. Another period of settling is included. After $2.5s$ the average motion of the particles is reduced below $0.010m/s$. Below this motion, the material bed is considered to be stable. The average particle motion is presented in a graph in Appendix C.

Domain size and boundary conditions

Due to the novelty of this simulation set-up, assumptions regarding the reference simulation had to be made. Within the experiments to follow, the sensitivity of the assumptions is analyzed.

Firstly, the horizontal domain size is set, this is set in a box shape in $y * x$ of $12 * 12m^2$, see Figure 5.6. Periodic boundaries at the y and x are included, meaning that a particles can leave the domain at the $-x$ direction and re-enter the domain at the $+x$ direction. In this way, the reaction forces of the particles outside the environment can be recreated. Starting at the top of the vertical domain, the scour protection thickness is indicated, t_{SP} in Figure 5.6. The DEM input parameters of the scour protection are equal to the calibrated input set5 of Chapter 4. The layer thickness of the scour protection is $2m$, similar to the upper limit of the scour protection design.
Furthermore, a subsoil is included in the simulation, $t_{subsoil}$ in Figure 5.6. The subsoil included consists of sand materials, the starting thickness of the sand layer is $1.75m$. An existing DEM sand material is incorporated, extracted from Cerfontaine et al. (2021). Including sand particles to their real scale would result in too expensive computational times, therefore the particles are scaled up. A so-called 'Mass scaling' method is used, where the particle sizes are increased while the particle densities remain constant (Evans & Valdes, 2011). Cerfontaine et al. (2021) uses 7 zones of scaling. Higher scaling factors are extending radially from the soil-structure interaction zone. This is a similar method of mesh refinement within the Finite Element Method. The largest scaling factor applied is 205, this value is incorporated for the sand scaling. Underneath the sand layer, a steel plate geometry is included. The monopile starts about $0.25m$ above the scour protection.

	symbol	unit	value
Sand steel friction	μ_{p-w}	$[mm]$	0.445
Particle friction coefficient	μ_s	$[-]$	0.264
Buoyant density	ρ'	$[kg/m^3]$	992
Particle shear modulus	G	$[GPa]$	3
Particle Poisson's ratio	ν	$[-]$	0.3

Table 5.1: DEM input parameters for HST95 sand (Cerfontaine et al., 2021)

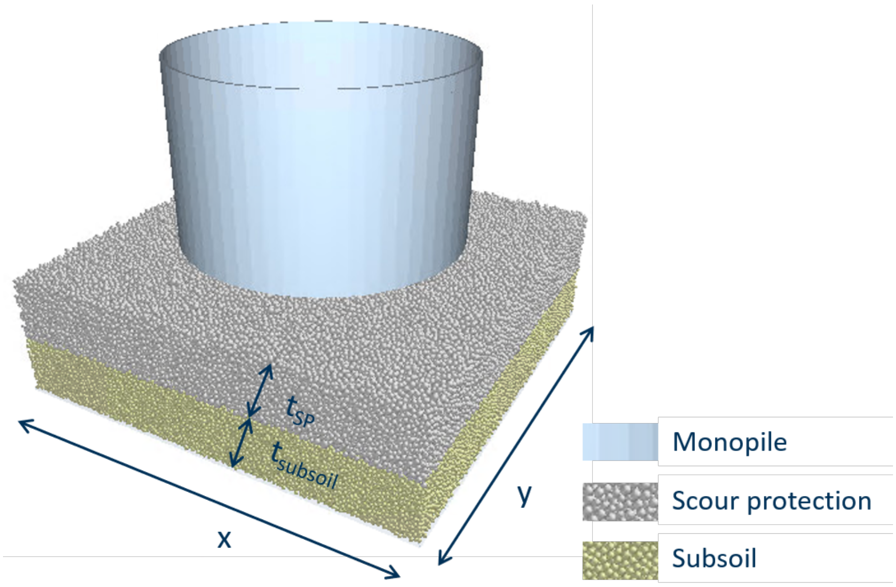

Figure 5.6: Full-Scale Monopile Simulation set-up

The computational time needed for a simulation is largely depending on the number of particles included in the simulation. The number of particles used in the simulation is presented in Table 5.2.

	Number of particles
Scour protection	164 672
Subsoil	247 952

Table 5.2: Number of particles within the base simulation

Monopile

The lower $5m$ of the monopile is recreated in Solidworks and imported into EDEM, see Figure 5.6. Consistently with the case study, the monopile diameter is $8m$ and the wall thickness $0.08m$ and mass $775ton$.

Force input and time scaling

In the case study, the F_{gbc} is introduced, this is the force that the monopile excites on the scour protection. Within the case study, the monopile penetrating through the scour protection takes about 20 minutes (see Figure 5.3). To decrease the computational time of the simulation, use is made of time scaling. The force input is scaled over time. In the starting simulation $1s : 10m$. This results in the following input force:

$$F_{gbc} = \begin{cases} -13500000 * t & \text{if } t \leq 0.55s \\ -7400000 & \text{if } t > t \end{cases} \tag{5.4}$$

This is a bold assumption, that needs further investigation, which is done in the experiments, further in the report.

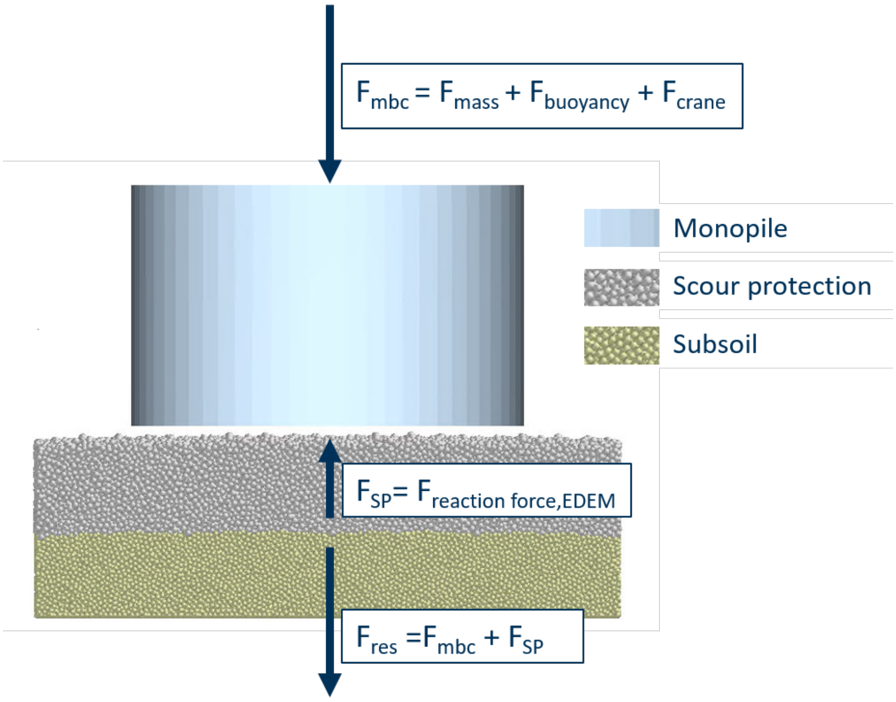

Figure 5.7: Force overview

5.3. Experimental design

Within the Full-Scale Monopile Simulation, the sensitivity of different input settings is investigated. This is done using the one-variable-at-a-time (OVAT) method. Using this method the direct effect of a DEM input variable is investigated.

In Figure 5.8 the experimental plan is provided, in the next section, all the steps are elaborately discussed, combined with the results. Note that the experimental plan begins with Experiment D. In the original plan, Experiment D was last. However, the time-scale experiments in Experiment D appeared to have a significant effect on the results and is therefore relocated to the beginning of the experimental plan. The simulation plan is updated and Experiments A,B, and C are rerun, using the output of Experiment D. The experimental sequence is adapted accordingly and the original names are maintained to keep all the documentation consistent.

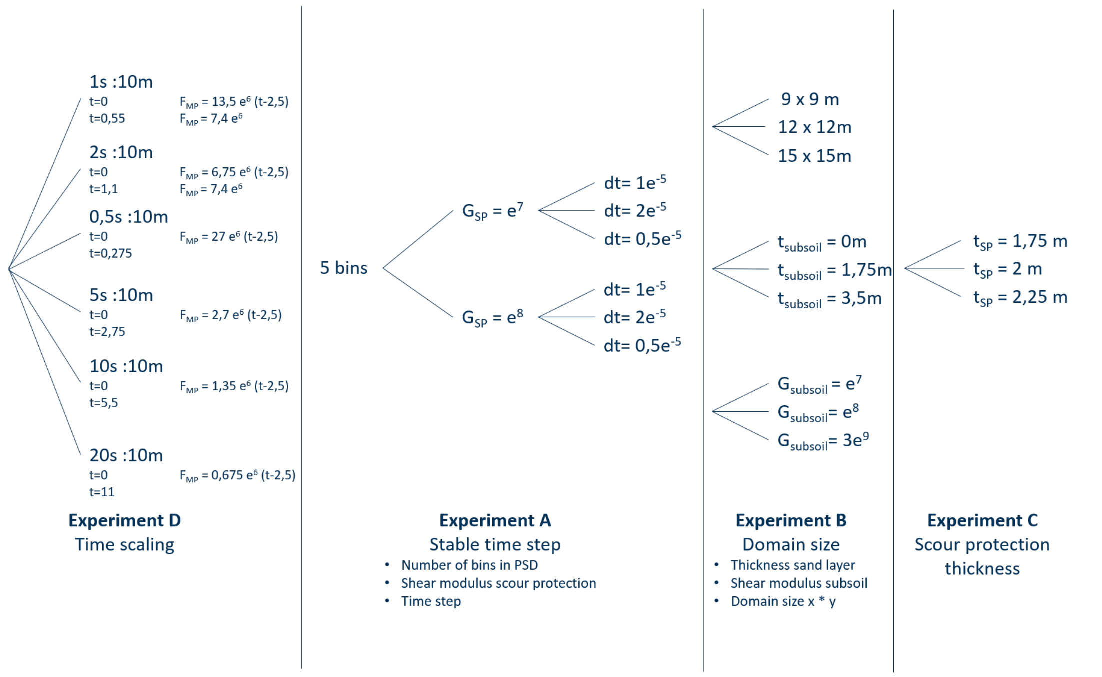

Figure 5.8: Simulation plan- Full-Scale Monopile Simulation

Sensitivity Analysis

The aim of a Sensitivity Analysis (SA) is to determine how changing an input variable, reflects in the output, in literature is referred to as Nominal Range Sensitivity (Frey & Patil, 2002). For Experiments B and C an SA is executed in the form of a comparison between the reference simulation and the experiment. This is for example done using the following formula:

$$SA = 100 - \frac{x_{sim}}{x_{ref}} * 100 \tag{5.5}$$

with:

- SA [%] is the deviation compared to the reference simulation
- x_{ref} [N] is the reference simulation output
- F_{sim} [N] is the experimental simulation output

The sensitivity analysis is executed on three simulation outputs (x):

- The monopile penetration time (t_{pen}), t when $z = 0$.
- The monopile velocity when reaching the seabed ($V_{z=0}$), v when $z = 0$.
- The reaction force when reaching the seabed ($F_{z=0}$), F when $z = 0$.

These three are selected because it is expected that those outputs are representative for the penetration resistance of the scour protection. The penetration resistance is the amount of force required to penetrate a bulk material, in this case, the scour protection

(Verruijt, 2018). There is not a target value available for the penetration resistance, however, in future research the outputs might be used for the calibration of for example the rolling friction between the particle and the geometry.

5.4. Results

Within this section, the results of the experiments are presented. For all experiments the data sets are plotted in two graphs. The observations of the graphs are given, followed by a conclusion per experiment. Experiments D and A generate new input for the experiments after. Experiments B and C focus on the environmental input, an SA is executed for Experiments B and C.

5.4.1. Experiment D. Time scaling

The time scaling of the force input on the monopile is adjusted to generate a feasible computational time for the simulation. This experiment is used to determine the time-scale in the simulations to follow. The base case consists of a time-scale of $1s : 10m$. The experiments show a time-scale of $0.5s : 10m$, $2s : 10m$, $5s : 10m$, $10s : 10m$ and $20s : 10m$. The linearly increasing force is adjusted accordingly. In the analysis of the results is referred to a smaller and a bigger time-scale. In which $0.5s : 10m$ is the smallest time-scale and $20s : 10m$ the largest time-scale.

The results of the simulation consist of two graphs, see Figure 5.9. In both graphs is the z-position of the monopile represented on the y-axis. Where $0m$ is the seabed, the scour protection reaches $2m$ and the vertical simulation boundary is at $-1.75m$. For Figure 5.9a, the x-axis represents the simulation time in seconds. In Figure 5.9b the reaction force of particles (F_{SP}) is represented on the x-axis. The simulations are executed twice, both simulations are plotted in the plots combined with the mean value.

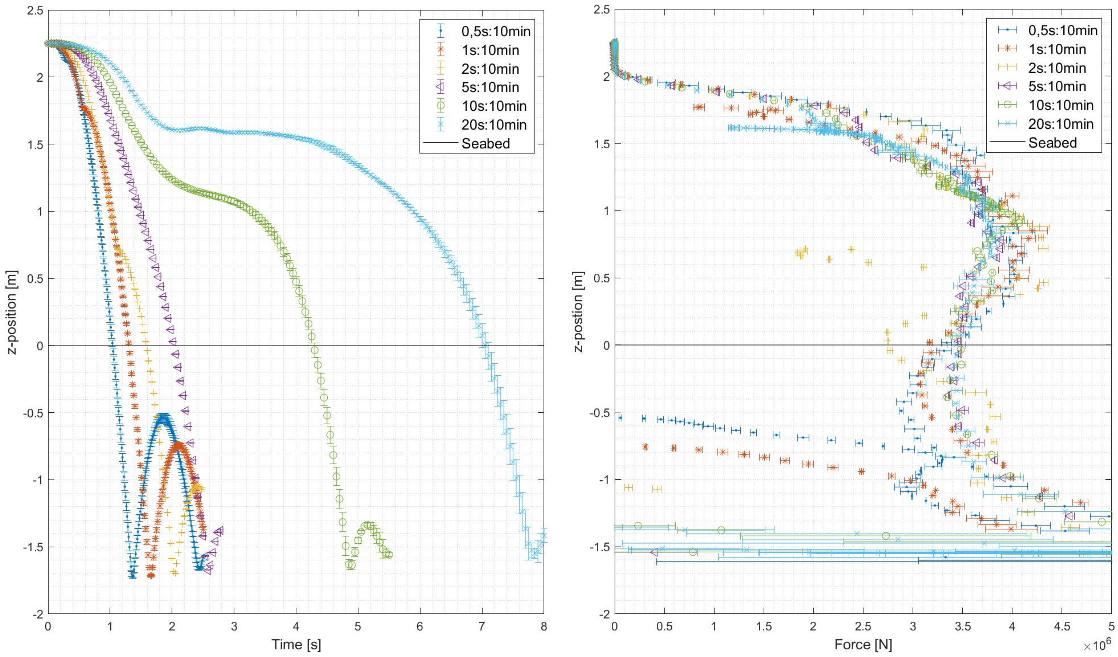

(a) Depth over time *(b)* Reaction force over depth

Figure 5.9: Experiment D. Time scaling results. *These plots are larger presented in Appendix F.*

For Figure 5.9a the difference between the two executed simulations is very limited, barely visible in the graph, meaning that the monopile penetration has not significantly changed within a new simulation. For Figure 5.9b this is also true when the monopile is above $-1m$. Below this value, a large deviation from the mean reaction force is observed.

Next the 'bounce behavior' will be discussed. With 'bounce behavior' is referred to the monopile response when the vertical boundary of the simulation is reached. When this happens particles get stuck between the bottom plate and the tip of the monopile, see Figure 5.10. This results in a strong reaction of the particles on the monopile. When the time scaling is smaller, a steeper linear input force is used, resulting in a higher 'bounce'. Visible in Figure 5.9a where the dark blue markers reach a height of almost $-0.5m$ after reaching the vertical boundary at $-1.75m$. The 'bouncing' phenomenon of the monopile is also enhanced in Figure 5.9b, where the reaction force of the smallest time-scale (the dark blue markers) varies within the depth range of $-0.5m$ and $-1.75m$.

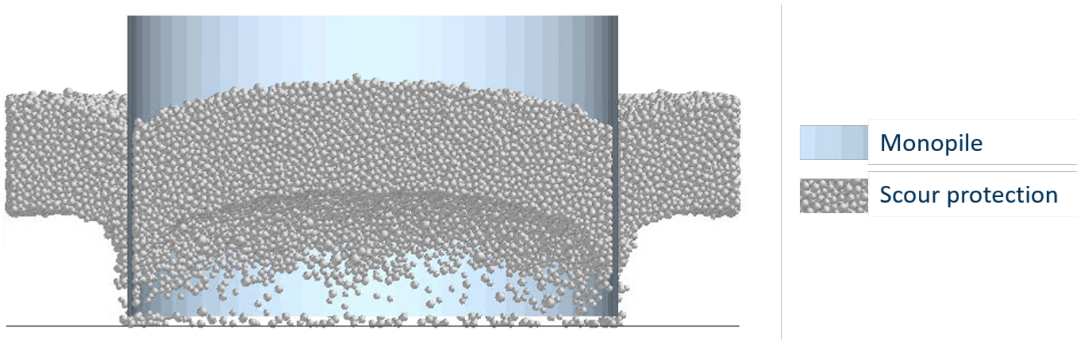

Figure 5.10: Side view, cut at $x = 0$ (the subsoil is not presented)

For the next remark is referred to Figure 5.11, this is a zoom-in of Figure 5.9. The focus is relocated towards the scour protection penetration and therefore is range of the z-position is reduced to $-0.5m < z < 2.5m$. Within time-scales, $1s : 10min$ and $2s : 1min$ similar behavior is presented. At $z = 1.8m$ for $2s : 1min$ and $z = 0.7m$ for $1s : 10min$, a small tilt is observed in the line. This tilt appears where the linear increasing input force reaches the maximum value of $7.4 * 10^6 N$ and converges to a constant input force. Within Figure 5.11b, those same depths show a deviating response of the reaction force. For the three larger time-scales the maximum force is not reached within the simulated time. And for the smallest time-scale ($0.5 : 10min$), the maximum force input is reached before the interaction with the scour protection starts, therefore no deviation in the trend is observed.

From time-scales $10s : 10m$ and $20s : 10min$, a non-linear trend in the penetration velocity can be observed. This is presented as a plateau in Figure 5.11a. The higher the time-scale, the earlier the non-linear trend is observed and the longer the plateau appears to be. This can be explained by the difference in the input force. As the time-scale deviates, the input force consequently deviates as well. A larger time-scale, results in a slower increasing input force. This slower increasing input force needs more time to reach the force needed to overcome the penetration resistance within the scour protection.

Focusing on the reaction force, in Figure 5.11b. It can be noticed that the reaction force converges to a similar trend for $5s : 10min$, $10s : 10m$, and $20s : 10min$. And the higher the time-scale, the closer the markers are together.

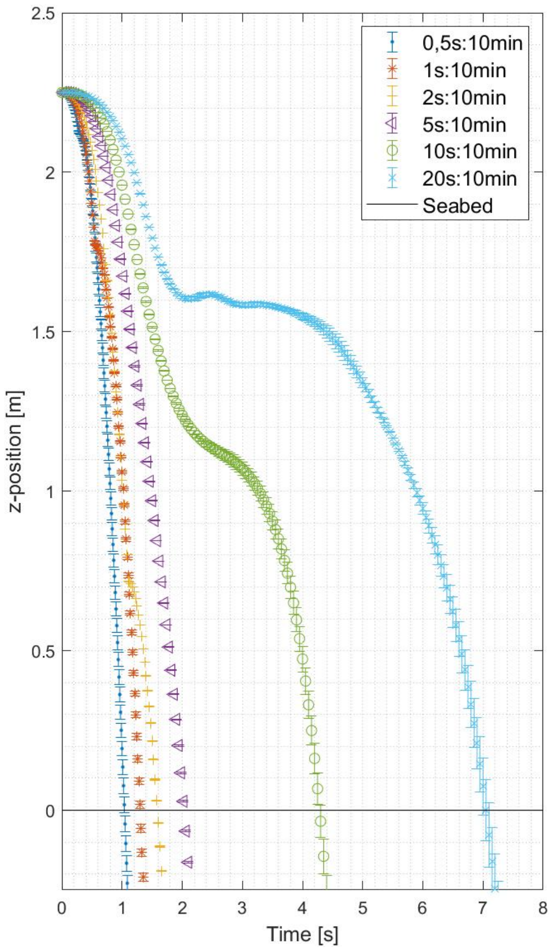

(a) Depth over time

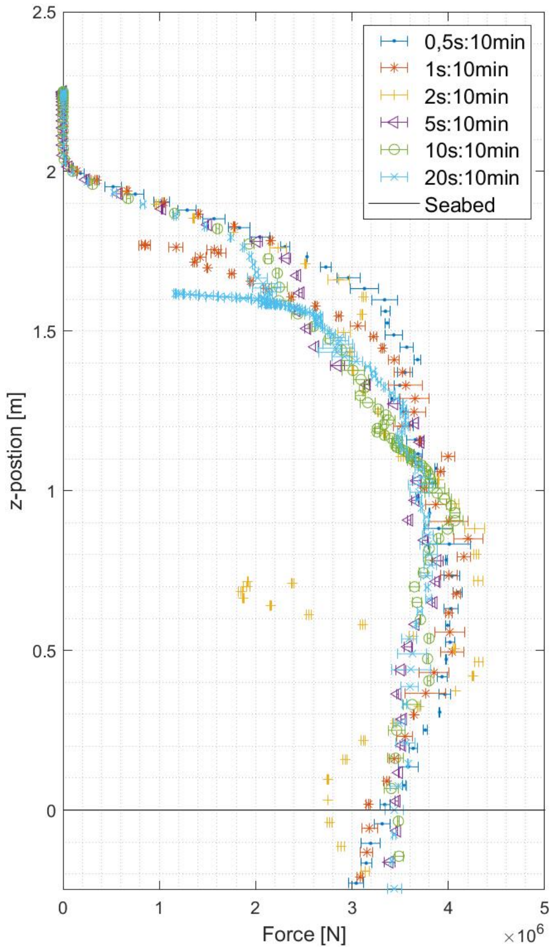

(b) Reaction force over depth

Figure 5.11: Experiment D. Time scaling results zoom-in (including standard deviation)

From the analysis above two main conclusions are drawn:

1. The diviation between the two executed simulations in the focus area is not significant, so further simulations will be executed once.
2. The upper three time-scales have converged to a similar trend. As $5s : 10min$, $10s : 10m$, and $20s : 10min$ show converging reaction forces of the scour protection, one of those three will be used for further simulations. And to include the plateau-behavior in the penetration over time plot, a time-scale of $10s : 10m$ (green o) is used for the simulations to follow.

5.4.2. Experiment A. Time step and shear modulus of scour protection

In Figure 5.8, the experimental plan shows for Experiment A, a differentiation in the shear modulus and three different time steps are used in the simulations. In Chapter 4 is shown that a more extensive PSD does not result in unrealistic bulk material. Combined with the extended computational time within a more elaborate PSD, it is decided to focus only on PSD with 5bins.

The results are presented in Figure 5.12, a consistent result representation of Experiment D is used. So, in both graphs is the z-position of the monopile tip represented on the y-axis. Where $0m$ is the seabed, the scour protection reaches $2m$, and the simulation environment stops at $z = -1.75m$. In Figure 5.12a, the x-axis represents the simulation time in seconds. In Figure 5.12b the reaction force of the scour protection (F_{SP}) is represented on the x-axis.

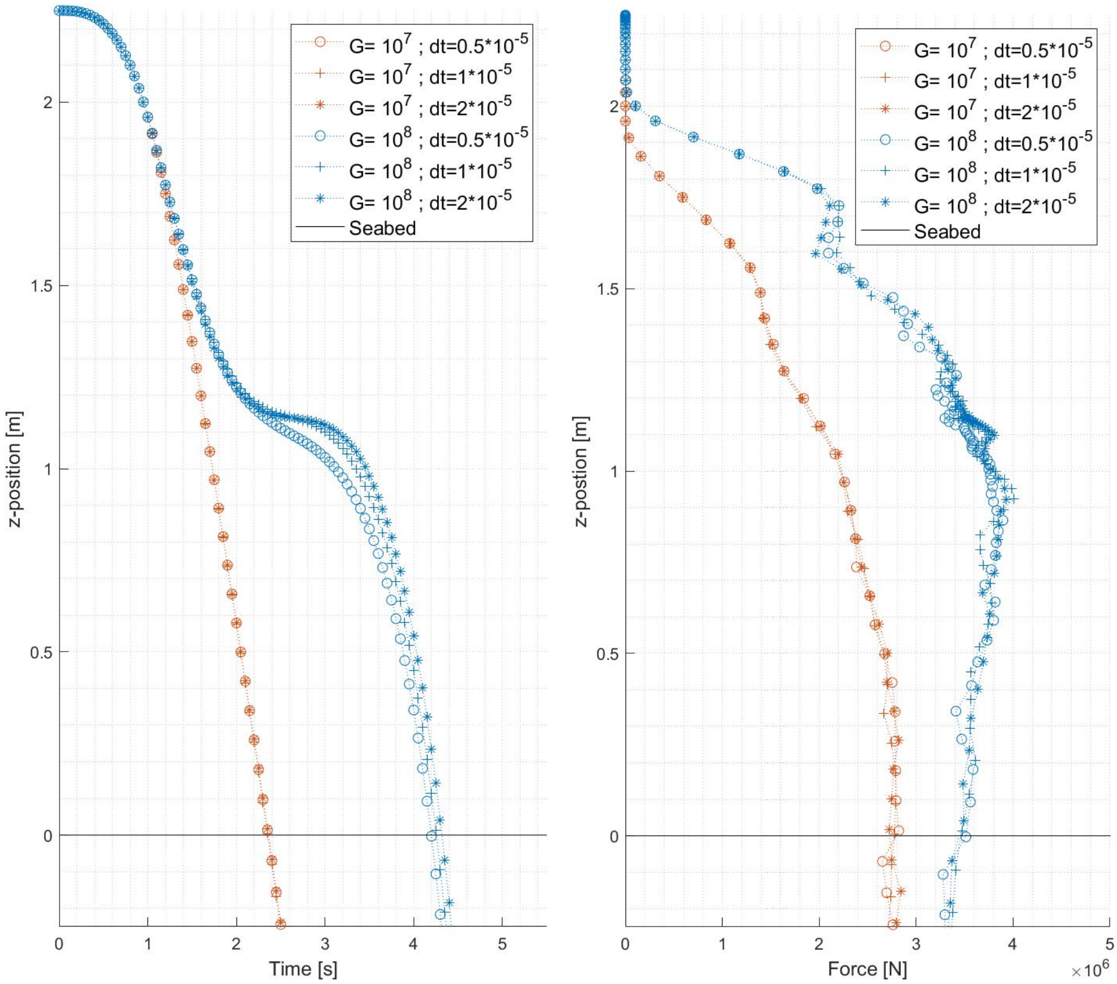

(a) Depth over time

(b) Reaction force over depth

Figure 5.12: Experiment A. Time step () and shear modulus (G) of scour protection

Focusing on the two clustered lines in the graphs, a comparison can be made between

$G = 1 * 10^7 Pa$ (orange scatter) and $G = 1 * 10^8 Pa$ (blue scatter). The lower shear modulus value shows a linear-like behavior in Figure 5.12a after $t = 1.5s$. This line crosses $z = 0m$ (the seabed) after about $2.4s$. For the higher shear modulus value, a deviation from the trend line is visible in the left graph. This represents a higher penetration resistance and slower penetration velocity, which is confirmed by the higher reaction force acting on the monopile in Figure 5.12b. This results in a penetration time of about $4.3s$.

For $G = 1 * 10^7 Pa$ (orange scatter), almost no variation in the results is observed for both the z-position over time and the reaction force over the z-position. For the reaction force working on the monopile, an increasing value can be observed in the beginning, followed by a relatively constant forcing towards the end. For $G = 1 * 10^8 Pa$ (blue scatter), more variation in the depth over time can be observed, starting at $t = 2.25s$. The variation is considered small. Within the reaction force over the z-position, the lines show similar variations. But a consistent trend is followed by the different time steps.

Besides the stability of the simulation, the computational expense of the simulation is of interest as well. The computation time is given in Table 5.3. A large deviation in the computational time is observed, it deviates from 2 to 8 hours. The computational time significantly increases when the time step decreases. A time step of $2 * 10^{-5}$ corresponds with a Rayleigh time step of $0.04T_R$. Commonly values between $0.2 - 0.4T_R$ are used. More research could be executed on the time step in future research.

sim	PSD	G $[Pa]$	dt $[s]$	computational time $[hh : mm]$
1	5bins	$1 * 10^7$	$1 * 10^{-5}$	04:02
2	5bins	$1 * 10^7$	$2 * 10^{-5}$	02:02
3	5bins	$1 * 10^7$	$0.5 * 10^{-5}$	07:52
4	5bins	$1 * 10^8$	$1 * 10^{-5}$	03:46
5	5bins	$1 * 10^8$	$2 * 10^{-5}$	02:00
6	5bins	$1 * 10^8$	$0.5 * 10^{-5}$	08:17

Table 5.3: Experiment A simulations and computational time

From the analysis above, the main conclusion is:

1. All the simulations are stable. So the main goal of Experiment A is reached using either of the six combinations. Next, the computation time is considered. A combination with $dt = 2 * 10^{-5}s$ is preferred, this corresponds with a stable simulation with a computational time of about 2 hours.

For the Truck Load Simulation (Chapter 4), the calibrated parameter input sets all require a $G = 1 * 10^8 Pa$, this draws the conclusion that a combination of $dt = 2 * 10^{-5}s$ and $G = 1 * 10^8 Pa$ will be used in further simulations.

5.4.3. Experiment B. Domain size

Experiment B focuses on the domain sizes of the simulation environment, combined with the shear modulus of the subsoil. This is done in 3 phases, the horizontal domain, the vertical domain, and the shear modulus of the vertical domain. The horizontal domain is represented by the $x * y$ in Figure 5.6. The vertical domain is represented by the lower particle layer, the subsoil layer ($t_{subsoil}$), in Figure 5.6. A sensitivity analysis of each of the phases is executed.
Similarly to Experiment D and A, two graphs are included per phase, see Figure 5.13, Figure 5.14 and Figure 5.15. In the graphs, the y-axis represents the monopile tip position, where $z = 0m$ is the seabed. For the left graph, the monopile position is plotted over time and for the right graph, the monopile position is plotted over the reaction force.

The analysis is done per domain characteristic, so a distinction between the horizontal domain, vertical domain, and shear modulus of the subsoil is made.

Horizontal domain

Within the horizontal domain of the simulation, three different sizes are simulated. Starting from the base case the horizontal domain consists of a square of $12 * 12m^2$. The monopile diameter is $8m$, so there is a $2m$ window between the monopile wall and the environment boundary. As the number of particles is an important parameter for the computational time, it is interesting to see how a decrease of the environment size (therefore decrease in the number of particles) will influence the simulation. Therefore additionally a domain of $9 * 9m^2$ and $15 * 15m^2$ are simulated.

In the two graphs of Figure 5.13, three data sets are plotted, varying with a horizontal domain of $9 * 9m^2$, $12 * 12m^2$, and $15 * 15m^2$. For the first $1.5s$, the data sets behave similarly. After which slower monopile penetration is observed for the smallest domain size (the blue data set). Within this same domain, the smallest domain, the monopile is pushed up a little at $t = 2.5s$, at a depth of $z = 1.3m$. At this same depth, the reaction force working on the monopile also shows varying data points. The force at this depth varies between $2.6MN$ and $4MN$.
For the $12 * 12m^2$ and $15 * 15m^2$ domains, the penetration behavior start deviating after $2.5s$. The reaction force of the particles in the $12 * 12m^2$ domain is slightly higher, resulting in a slightly slower monopile penetration.

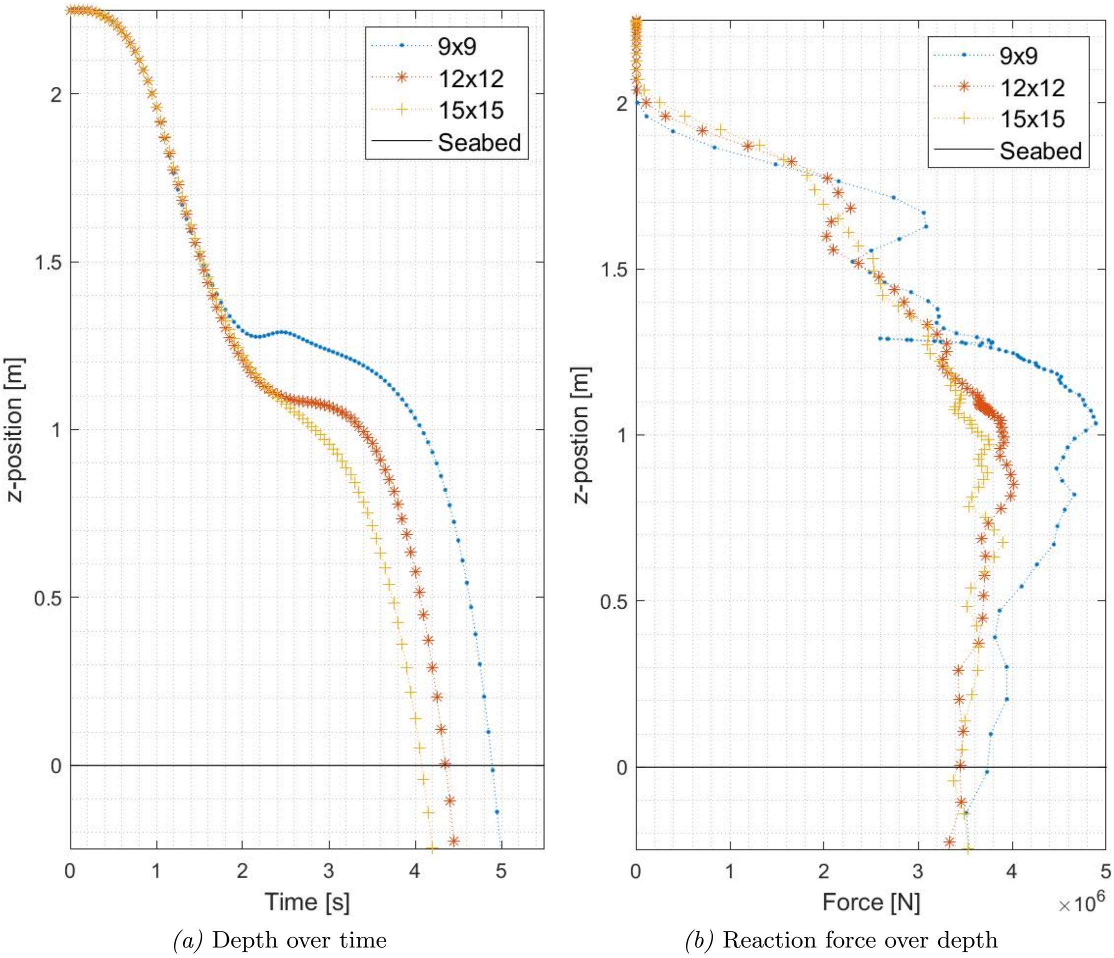

Figure 5.13: Experiment B. Horizontal domain

In Table 5.4, three characteristic values of the simulation are compared using the earlier introduced SA (Equation 5.5). The three characteristic values are: the monopile velocity when reaching the seabed, the time needed to fully penetrate the scour protection, and the reaction force of the particles when the seabed is reached.
For the $15 * 15m^2$ domain, the penetration time and the impact force deviate the least from the reference simulation. The impact velocity of the $15 * 15m^2$ simulation has a larger deviation from the reference simulation compared to the $9 * 9m^2$ domain size.

ExpB_horz domain size			$12 * 12m^2$	$9 * 9m^2$		$15 * 15m^2$	
			reference sim	sim2	SA	sim3	SA
Impact velocity	$v_{z=0}$	$[m/s]$	-2.3	-2.4	-4%	-1.9	17%
Penetration time	t_{pen}	$[s]$	4.4	4.9	-11%	4.1	7%
Impact force	$F_{z=0}$	$[MN]$	3.5	3.7	-8%	3.4	2%

Table 5.4: SA of Experiment B. Horizontal domain

Vertical domain

Within the vertical domain, coarse sand is simulated below the scour protection to avoid interaction from the floor plate at the bottom of the simulation. This thickness varies from $0m$, $1.75m$, and $3.5m$, where $1.75m$ is the reference thickness.
In Figure 5.14 the results of Experiment B regarding the thickness of the vertical domain are presented. With the thickness of the vertical domain is referred to the subsoil layer underneath the scour protection. For the first $3.5s$, the three plots show comparable behavior. One could even say that the penetration resistance of the simulation without subsoil is slightly less, as the blue data points are on the lower side of the trend between $1.8s$ and $3s$. However, this behavior changes when the monopile starts to interact with the environmental boundary. For the blue scatter data the particles are stuck between the horizontal bottom plate and the monopile, resulting in a stop of the monopile movement. Comparing $t_{subsoil} = 1.75m$ and $t_{subsoil} = 3.5m$, a slightly higher reaction force can be observed in the $t_{subsoil} = 3.5m$ between $z = 2m$ and $z = 1.5m$. Generally the results are very similar.

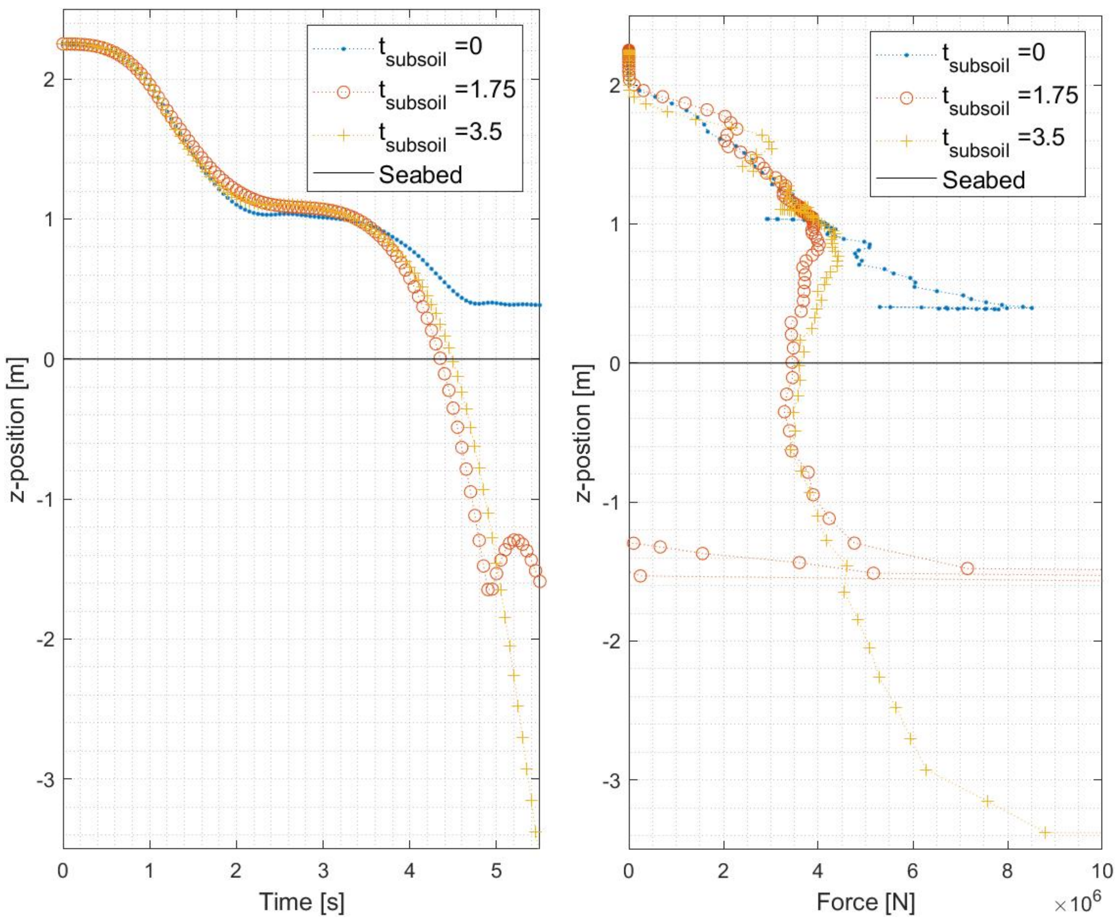

(a) Depth over time *(b)* Reaction force over depth

Figure 5.14: Experiment B. Vertical domain

Table 5.5 presents the results of three characteristic values of the simulations. For the blue scatter data, where $t_{subsoil} = 0$, the monopile does not reach the seabed. Therefore no data is available at his point. For the data set with $t_{subsoil} = 3.5$, some deviations compared to the reference simulation can be observed. The impact velocity has the largest deviation of 12%, the monopile penetration time and the reaction force at the seabed are both below a 5% deviation.

ExpB_vert domain			$t_{subsoil} = 1.75m$	$t_{subsoil} = 0m$		$t_{subsoil} = 3.5m$	
			reference sim	sim5	SA	sim4	SA
Impact velocity	$v_{z=0}$	$[m/s]$	-2.3	-	-	-2.0	12%
Penetration time	t_{pen}	$[s]$	4.4	-	-	4.5	-2%
Impact force	$F_{z=0}$	$[MN]$	3.5	-	-	3.6	-4%

Table 5.5: SA of Experiment B. Vertical domain

Shear modulus of the subsoil

The shear modulus of the subsoil influences the computational time of the simulations significantly. In the reference simulation, the shear modulus of the subsoil is $1 * 10^8$ Pa. Within the experiments values of $1 * 10^7$ Pa and $3 * 10^9$ Pa are simulated. This last value is the calibrated shear modulus of the HST95 sand (Cerfontaine et al., 2021).
The shear modulus influences the penetration resistance, a higher shear modulus results in a stiffer contact spring meaning a higher penetration resistance. However, it is unclear how the penetration resistance of the scour protection is influenced by the shear modulus of the layer underneath. This experiment aims to present the influence of the shear modulus variation on the penetration resistance of the layer on top.

The three plotted data sets in Figure 5.15 start with an equal penetration velocity. However, it can be observed in Figure 5.15b that the penetration resistance is slightly lower at the same depth for $G_{subsoil} = 1 * 10^7 Pa$ compared to the other two lines. At $t = 1.6s$ the three lines diverge. The steepest line is $G_{subsoil} = 1 * 10^7 Pa$, meaning the highest monopile velocity and the fastest monopile penetration time. For $G_{subsoil} = 1 * 10^8 Pa$ and $G_{subsoil} = 3 * 10^9 Pa$ an almost equal penetration time is observed. The reaction forces of $G_{subsoil} = 1 * 10^8 Pa$ and $G_{subsoil} = 3 * 10^9 Pa$ follow the same trend.

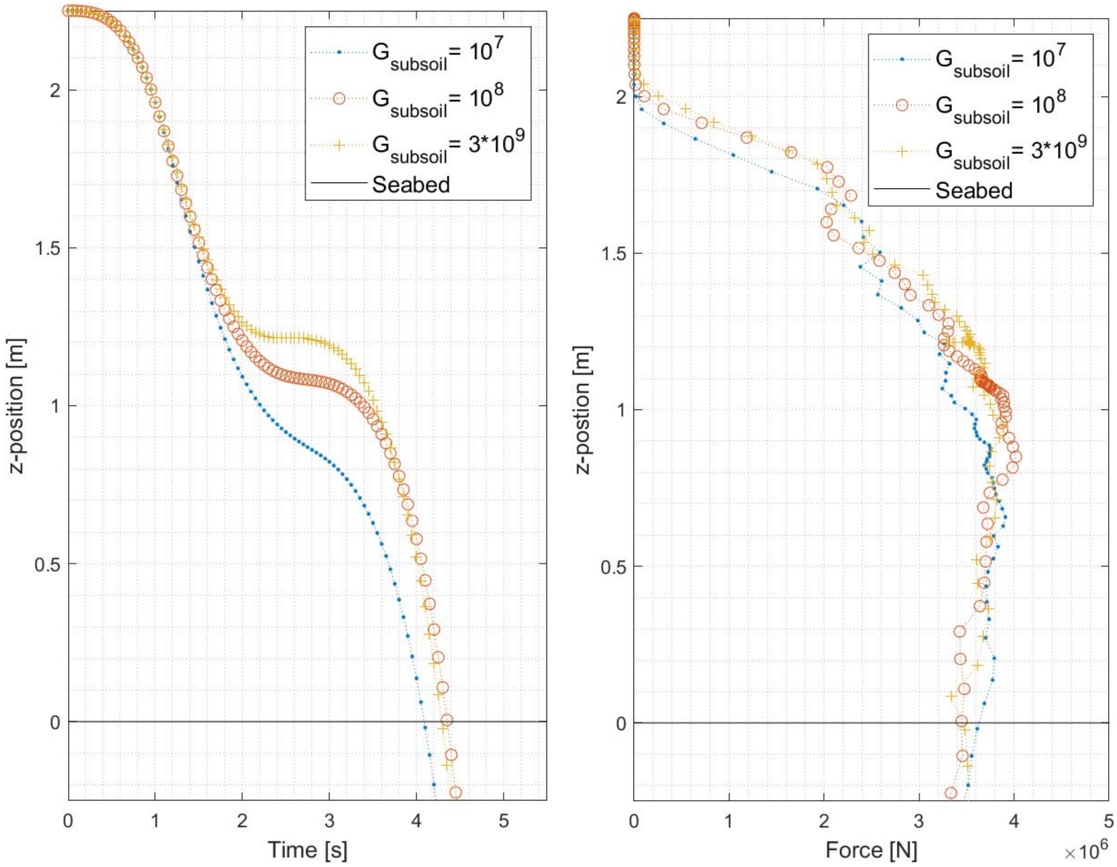

(a) Depth over time *(b)* Reaction force over depth

Figure 5.15: Experiment B. Vertical domain, shear modulus subsoil

In Table 5.6 the sensitivity of the shear modulus of the subsoil is presented. The deviation of 27% of the impact velocity at the seabed shows that the simulation is sensitive to the shear modulus input of the subsoil. A higher shear modulus of the subsoil however presents less deviation compared to the reference simulation, possibly the simulations are converging towards a constant output.

ExpB_vert domain shear subsoil			$G_{subsoil} = 10^8 Pa$	$G_{subsoil} = 10^7 Pa$		$G_{subsoil} = 10^9 Pa$	
			reference sim	sim6	SA	sim7	SA
Impact velocity	$v_{z=0}$	$[m/s]$	-2.3	-1.7	27%	-2.2	3%
Penetration time	t_{pen}	$[s]$	4.4	4.1	7%	4.3	2%
Impact force	$F_{z=0}$	$[MN]$	3.5	3.6	-4%	3.5	-1%

Table 5.6: SA of Experiment B. Vertical domain, shear modulus of subsoil

It can generally be concluded that all three tested variations in the domain characteristics results in noticeable deviations in the results.

1. For the horizontal domain size the largest variation appeared when the domain size was decreased. For the two upper simulations, the results converge.
2. For the vertical domain size can be concluded that a subsoil is necessary for the simulation, since without a subsoil the monopile will not penetrate the scour protection. The difference between the two subsoil thicknesses is considered small enough to continue with the $t_{subsoil} = 1.75m$ for this research.
3. For the shear modulus of the subsoil, the smallest value $S_{subsoil} = 1 * 10^7$ gives larger variations compared to the reference simulation than the $S_{subsoil} = 3 * 10^9$. Especially focusing on the velocity at the seabed, the monopile penetration time and the reaction force at the seabed shows small variation using either $S_{subsoil} = 3 * 10^9$ or $S_{subsoil} = 1 * 10^8$.

5.4.4. Experiment C. Scour protection thickness

Within Experiment C, the influence of the scour protection thickness is simulated. In the reference simulation, the scour protection thickness is approximately $2m$. The additional experiments have a scour protection thickness of $1.75m$ and $2.25m$. The scour protection layer is visualized in Figure 5.6 as the grey particle layer (t_{SP}).
The results are presented in Figure 5.16. In both graphs, the y-axis presents the monopile tip position, where $z = 0m$ is the seabed. For the Figure 5.16a, the monopile position is plotted over time and for Figure 5.16b the monopile position is plotted over the reaction force.
Since the scour protection thickness deviates, the data sets start at different heights, see the graphs in Figure 5.16. It can be observed in Figure 5.16a that the curvature in the blue graph is less apparent, and a more constant monopile penetration is observed. For the orange and yellow lines, a similar curvature is present. The reaction forces in Figure 5.16b shows a similar trend in the progression of the data. The simulation with the thickest scour protection shows the biggest reaction force, which can be explained by the presence of more particles.

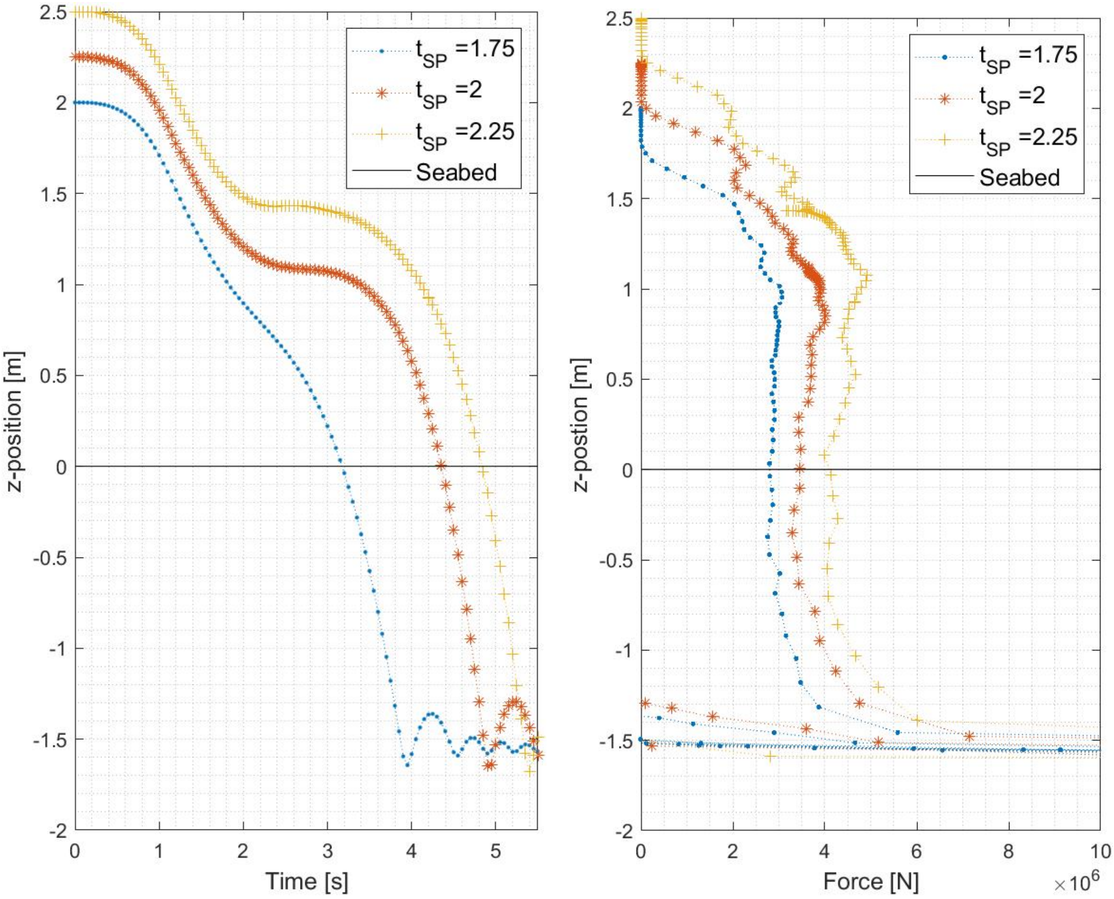

(a) Depth over time *(b)* Reaction force over depth

Figure 5.16: Experiment C. scour protection thickness

A similar table compared to Experiment B is generated for Experiment C, see Table 5.7. Comparing the velocity of the monopile when it reaches the seabed, it shows that thinner protection leads to a slower penetration velocity. This is not an expected result, but can be explained by the force input. The force input is dependent on time, and since the SP is thinner the monopile reaches the seabed earlier and therefore has less force and velocity compared to the reference simulation.
Using the same thought for the thickest scour protection a faster velocity is expected compared to the reference simulation. This is not observed in the results. A similar velocity at the seabed is observed. Due to the penetration resistance in a thicker layer is higher and the increasing force does not translate to an increasing velocity.
The time needed for the monopile to penetrate the full scour protection can be used to see if a similar increase as decrease in the thickness would result in a similar deviation compared to the reference. This is not observed in the data. A decrease of $0.25m$ results in a penetration 27% faster than the reference and an increase of $0.25m$ results in a

penetration 10% slower.
The reaction force of the particles on the monopile increase

ExpC_SP_thickness			$t_{SP} = 2.00m$	$t_{SP} = 1,75m$		$t_{SP} = 2.25m$	
Impact velocity	$v_{z=0}$	$[m/s]$	-2.3	-1.5	36%	-2.3	0%
Penetration time	t_{pen}	$[s]$	4.4	3.2	27%	4.9	-10%
Impact force	$F_{z=0}$	$[MN]$	3.5	2.8	19%	4.1	-19%

Table 5.7: SA of Experiment C. Scour protection thickness

s or decreases either with 19% for the thicker and thinner protection layer.

It is concluded that:

1. A change in the scour protection thickness does not result in a linear shift in the penetration velocity and force. For this specific experiment, it is observed that a decreasing scour protection thickness has more influence on the results compared to an increase in the thickness. Therefor should the scour protection thickness be included as a variable parameter.

5.5. Conclusion

Within this chapter, a full-scale monopile simulation is set up. To create a simulation where the actual monopile installation is simulated as accurately as possible, without creating an unnecessary large simulation, the influences of multiple input parameters are tested. At the start of this chapter, a reference simulation is designed based on a case study. Within this reference simulation, multiple input settings are tested in the experimental design:

- Exp. D: the time scaling of the force input
- Exp. A: the combination within the shear modulus and time step
- Exp. B: the domain size and characteristic
- Exp. C: the scour protection thickness

Using the results from the experiments, sub-question four answered:

> **SQ4:** How can a numerical model for full-scale monopile self-weight penetration be reached with optimization in accuracy and computation time?

From the results of Experiment D, the time scaling is encountered to seriously influence the simulation. After testing 6 different time-scales, a time-scale of $10s : 10m$ is used in the simulations. The reason for this is the converging results of the time-scales combined with the non-linear trend present in this time-scale.

From Experiment A is concluded that the shear modulus of the scour protection significantly influences the simulation results. This is expected as a higher shear modulus results in higher penetration resistance. For these experiments is decided to continue with the highest shear modulus, however, should the shear modulus be calibrated using experimental data in future research.

For the domain size and characteristic, it can be stated that a domain size of $12 * 12m^2$ is a minimum value. This corresponds with a minimum of a $2m$ window between the edge of the monopile and the enviromalal boundary. A smaller domain creates unintentional deviations in the results. For now a $12 * 12m^2$ domain is accepted to be sufficient, as the response force from EDEM particles in a $12 * 12m^2$ and $15 * 15m^2$ converge to similar output.
For the vertical domain, a subsoil is required in the simulation. Using either a subsoil of $1.75m$ or $3.5m$ thick generates roughly the same results. A minimum thickness should be investigated. Just as the characteristics of the subsoil. Deviating the shear modulus of the subsoil, creates significant deviation in the results. The shear modulus of the subsoil should be further investigated during the calibration of the penetration resistance in future research.

Lastly, the influence of the scour protection thickness is investigated. The reaction force generated by the scour protection increases when the thickness of the scour protection increases. For all tested scour protection thickness, a successful monopile installation is obtained. The scour protection thickness is recommended to be included as a variable input parameters in the simulations, comparable to real-time practice.

6. Validation of the Full-Scale Monopile Simulation

To investigate whether the simulation is representative for practice, a validation is executed. The case study introduced in Chapter 5, based on data from practice is compared with the reference simulation of Chapter 5. This simulation has appropriate sizes based on the experiments in Chapter 5.
Due to the novelty of this research, a qualitative validation is executed. Firstly the observations in the comparison between the simulation and practice are given, followed by an explanation of the observations. Within this explanation additional simulations are run for comparison with practice. Furthermore, some additional data from practice are discussed. Followed by the conclusion.

6.1. Observations

The case study data and the EDEM simulation data are both plotted in Figure 6.1. The qualitative validation is executed for two criteria:

1. Successful penetration
2. Comparable depth over time correlation

Successful penetration

Starting with the first criterion, successful penetration, this criterion is successfully validated. In both the EDEM simulation and the case study, a successful penetration is reached.

Comparable depth over time correlation

For validating the penetration over time, the case study data is time-scaled equally to the EDEM simulation, they are both scaled up to $10s : 10m$.
The case study data and the EDEM simulation data are both plotted in Figure 6.1. In this graph is observed that the simulation data and the case study do not behave according to the same trend. The process in the EDEM simulation is significantly faster. The simulation takes about $4.5s$ to penetrate the scour protection, compared to $19s$ within the case study. Therefore the penetration velocities are considerably different as well.

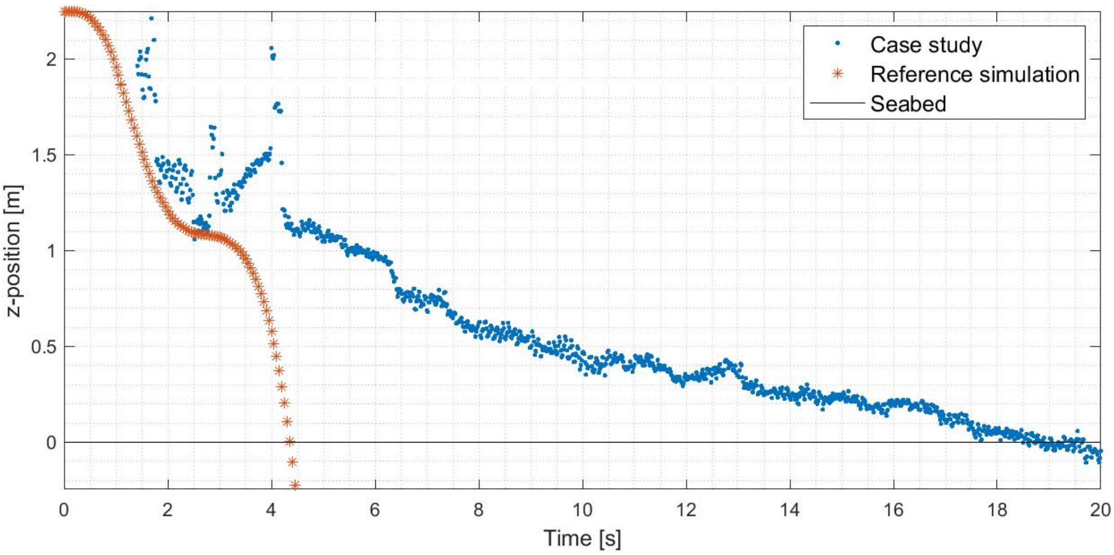

Figure 6.1: Depth over scaled time, comparison of reference simulation and case study data

6.2. Explanation

The difference between the simulation and the case study could be explained by a difference in the penetration resistance. The penetration resistance is defined as the amount of force required to penetrate a bulk material. It appears that the penetration resistance in the simulation is significantly underestimated compared to the case study, resulting in a smoother and faster monopile penetration in the simulation.
The penetration resistance is unknown for the scour protection material. When the penetration resistance of the scour protection is known, it could be included as a KPI during the calibration. When there would be a target value for the penetration resistance, the rolling friction between the monopile and the scour protection (μ_{p-w}) and the shear modulus (G) could be calibrated and a more realistic simulation is expected.

6.2.1. Restricted rolling

Moreover, made assumptions concerning the DEM simulations result in an underestimation of the penetration resistance. For example, the simulation is executed with spherical particles, while in practice the rocks are angular. This can result in a misrepresentation of the penetration resistance. However, a higher rolling resistance can compensate for this underestimate (Wensrich & Katterfeld, 2012). To analyze the rolling of the scour protection material within the reference simulation, the angular velocity of the particles is analyzed. The angular velocity is defined as:

$$\omega = \frac{\Delta\phi}{\Delta t} \tag{6.1}$$

Where ω is the angular velocity $[rad/s]$, $\Delta\phi$ is the difference in angle $[rad]$ and Δt is the difference in time $[s]$.

The angular velocity of the scour protection material is presented in Figure 6.2 for the reference simulation. The angular velocity during the monopile self-weight penetration is varying between 0 and 0.9 rad/s, (consistent with 0 to 52 $^\circ/s$). The angular velocity increases while the monopile tip starts penetrating the scour protection. Followed by a decrease in the angular velocity. After which the angular velocity builds up towards a peak, as the tip of the monopile reaches the subsoil layer at $t = 4.3s$.
To limit the rolling of the scour protection rock, two simulations are created. Simulation 1, where the rolling is restricted by implementing $\mu_r = 1$ (Tang et al., 2012) and in simulation 2, where no rolling of the scour protection materials is allowed. The angular velocity of these two simulations combined with the reference simulation is presented in Figure 6.2.

A lower angular velocity can be observed, for the simulation with restricted rolling compared to the reference simulation. A similar trend of the behavior is observed compared to the reference simulation. An increasing angular velocity when the monopile reaches the scour protection. Building towards a peak when the monopile starts interacting with the subsoil. For the reference simulation, this is at $t = 4.3s$ and for the restricted rolling simulation this is at $t = 6.2s$. However, the peaks of the simulation with restricted rolling are significantly lower.
As configured within EDEM, there is no rolling of the scour protection materials for the no rolling simulation.

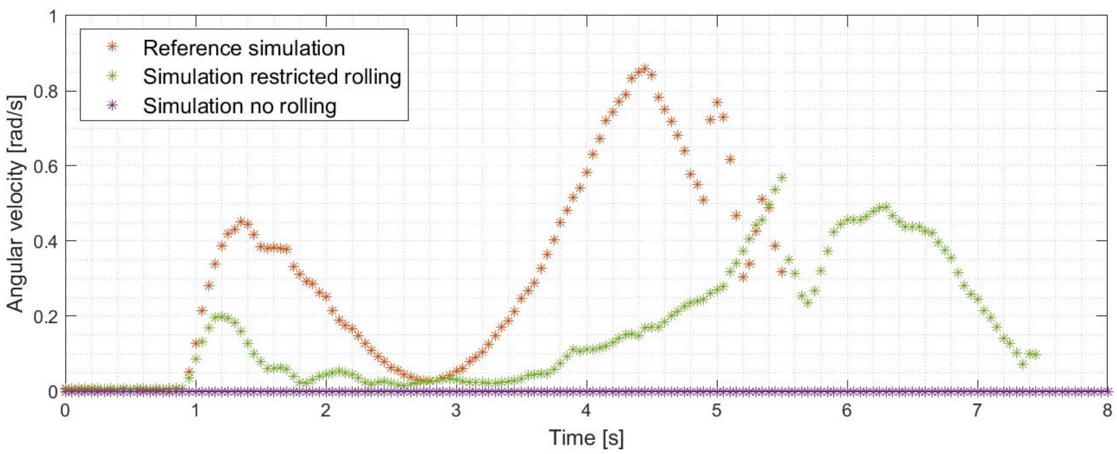

Figure 6.2: Angular velocity ($o\omega$) of the reference simulation, the simulation with restricted rolling, and the simulation without rolling

Within Figure 6.3, the penetration over time of the reference simulation, the simulation with restricted rolling, the simulation without rolling, and the case study are presented. The simulation without rolling does not result in successful penetration of the scour protection. This means that by eliminating the rolling of the scour protection, the penetration resistance becomes too high for the monopile to overcome within the simulation. Within the two other simulations, successful penetration is presented. An increased penetration time is observed for the simulation with restricted rolling, however, the simulation is still significantly different, compared to the case study data.

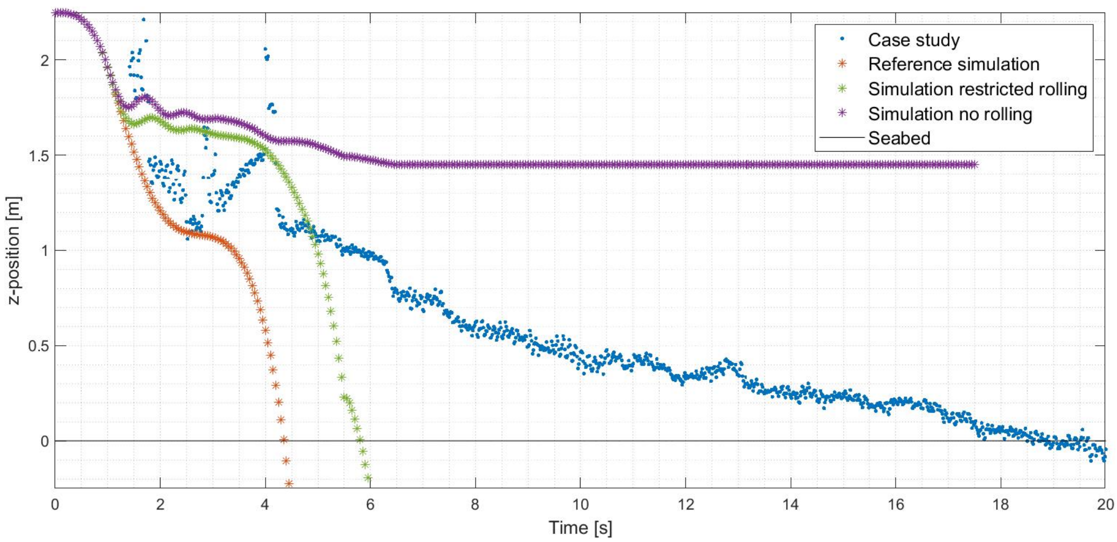

Figure 6.3: Depth over time plot, comparison reference simulation, restricted rolling simulation, no rolling simulation and case study data

6.3. Data from practise

Besides the improvements that can be made within the EDEM simulation, it should also be taken into account that within the data from practice a large variation exists. For example, the penetration time can vary from 20 minutes to 4 hours. The incorporation of those large variations should be taken into account in future research. For example taking the three data sets presented in Figure 6.4, all have the same scour protection design, monopile tip diameter, and wall thickness. However, the penetration time and behavior are very different. Monopile 3 takes about double the time to penetrate the scour protectoin compared to Monopile 1. While Monopile 2, needs to be taken out of the scour protection to be replaced again. What these three monopile installations have in common is that successful monopile installation has been reached.

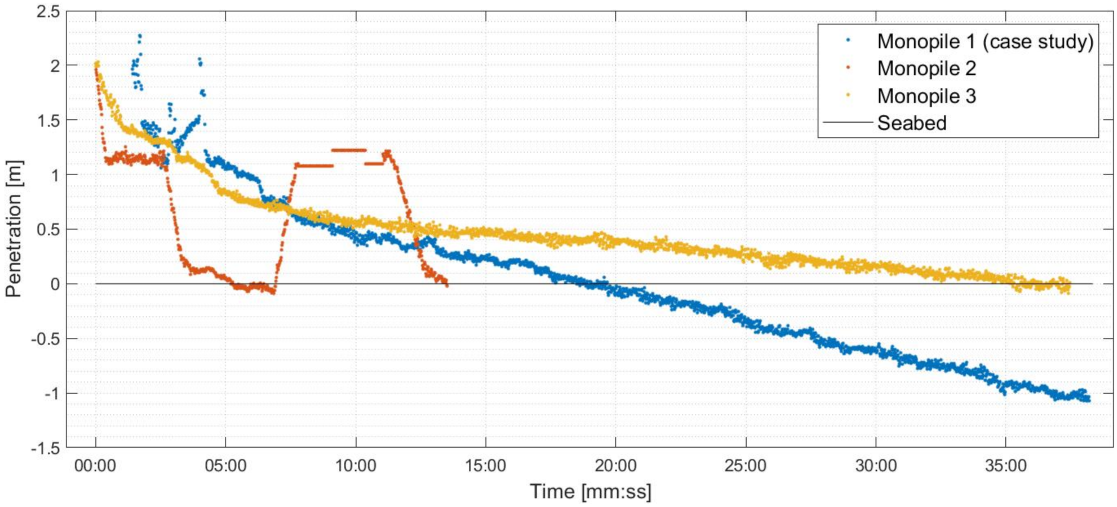

Figure 6.4: Monopile installation data

6.4. Conclusion

Rewinding towards the fifth sub-question:

> **SQ5:** To what extent does the full-scale numerical model represent practice?

After the qualitative validation the following conclusions can be drawn:

- Successful penetration can be mimicked in the EDEM simulations.
- The current simulation is not able to capture an accurate depth over time correlation compared to the case study. An underestimation of the penetration resistance is observed.
- An increased rolling restriction results in slower penetration and therefore a higher penetration resistance. The simulation with restricted rolling is however neither representative compared to the case study at this point.
- Eliminating rolling of the scour protection from the simulation does not result in successful penetration of the material bed, as the penetration resistance becomes to high.
- Large variation in data from practice complicates the validation. This makes developing an adequate simulation challenging. The simulation might work for some of the data in practice, but it might be unknown if all situations can be simulated.

7. Conclusions and Recommendations

This research aims to develop a numerical model of monopile installation through scour protection. The main research question is formulated as:

Is it feasible to develop a full-scale numerical model of monopile self-weight penetration through scour protection?

Within this chapter the research questions are answered in Section 7.1, followed by recommendations for future research in Section 7.2.

7.1. Conclusions

The sub-question presented in Chapter 1 are answered below, followed by the answer to the main research question

SQ1: What physical processes can be identified during monopile self-weight penetration through scour protection?

From the literature survey, a knowledge gap is identified regarding the technical feasibility of installing monopiles through scour protection. Currently, different driveability models focusing on pile driveability exist. However, these models do not include rock material layers like scour protection. Four main physical processes are identified in monopile self-weight penetration through scour protection:

- The development of tip resistance due to the scour protection layer.
- The development of shaft resistance due to the scour protection layer.
- The self-weight penetration due to the weight and dimensions of the monopile.
- The interaction between the monopile wall and the scour protection rock and inter-rock interaction (interlocking, rotation, breaking, and protrusion of the subsoil).

SQ2: What is an adequate numerical modelling method?

Currently, there is no numerical model which includes all the physical processes described above. To increase the understanding of monopile self-weight penetration through scour protection, the Discrete Element Method (DEM) is used. DEM is considered most suitable for the representation of the scour protection behavior. DEM is an effective method for addressing engineering problems in granular materials. The most important reason for using DEM is due to the discontinuous behavior of the scour protection materials.

SQ3: What are appropriate parameter input sets for the bulk behavior of the scour protection?

The parameter input for the numerical model is calibrated using two Key Performance Indicators (KPIs): the porosity of the bulk materials and the angle of repose. To reach the target values of the KPIs, five input parameters are varied: the particle size distribution (PSD), the static friction (μ_s), the rolling friction (μ_r), the particle density (ρ), and the shear modulus (G). In total 5 optimized parameter input sets are generated, presented in Chapter 4. All 5 parameter input sets have limited deviation of the KPI target values and are considered suitable to use in further simulations. Parameter input set5 is used in the follow-up of the research, see Table 7.1.

	PSD [bins]	ρ $[kg/m^3]$	μ_s $[-]$	μ_r $[-]$	G $[Pa]$
Set5	5	1625	0.5	0.5	$1 * 10^8$

Table 7.1: Parameter input set5

SQ4: How can a numerical model for full-scale monopile self-weight penetration be reached with optimization in accuracy and computation time?

A numerical model of monopile self-weight penetrating is created using a discrete element simulation. The Full-Scale Monopile Simulation has been designed, using a monopile with an outer tip diameter of $8m$. The material bed consists of a sandy subsoil and a scour protection on top. The downward force due to the mass of the monopile is time-scaled ($10s : 10min$).
Four experiments are conducted to determine the DEM input settings to achieve a realistic stable simulation with a reasonable computational time. The time scaling is set to $10s : 10min$ with a time-step of $2 * 10^{-5}s$. The sensitivity of the domain size and domain characteristics are analyzed. From the experiments regarding the domain characteristics, the following conclusions are drawn:

- A minimum environment of $12*12m^2$ is recommended, when using an $8m$ diameter monopile. Resulting in a window of $2m$ between the monopile and the environment boundary.
- A subsoil is required for successful penetration through the scour protection layer.
- The subsoil input parameters are of significant influence on the penetration behavior of the monopile, due to the rock penetration into the subsoil.

Furthermore, is the thickness of the scour protection varied. The reaction force, generated by the scour protection, increases when the thickness of the scour protection increases. Since also the installation thickness of the scour protection varies in practice, the following conclusion is drawn:

- The scour protection thickness can be included as a variable parameter.

SQ5: To what extent does the full-scale numerical model represent practice?

To analyze whether the model is representative for practice, the model is qualitatively validated by comparing the penetration data of the simulation to the case study. For the validation of the DEM simulation, a scour protection thickness of $2m$ is used, this is the upper bound of the installation design in the case study.
A successful penetration through the scour protection has been reproduced. The accuracy of the penetration resistance is questionable at this stage, as an underestimation of the penetration resistance in the rock material is observed. The use of spherical particles can for example lead to such an underestimation. To compenstae this, a higher rolling resistance can compensate for this underestimate. Two additional simulations are executed: firstly is angular velocity restricted by increasing the coefficient of rolling friction and secondly no rolling is allowed within the simulation. For the restricted rolling simulation, an increasing penetration resistance, compared to the reference simulation, is observed. The simulation without rolling does not result in successful penetration of the scour protection. There is at this point no representative simulation found.

Is it feasible to develop a full-scale numerical model of monopile self-weight penetration through scour protection?

It is feasible to develop a full-scale numerical model of monopile self-weight penetration through scour protection. This can be done by using the Discrete Element Method. A Full-Scale Monopile Simulation is developed within this thesis. Currently, no accurate representation of practice has been found, hence, recommendations to achieve this are given in the next section.

7.2. Recommendations

The recommendations for further research that arose from this thesis are given below and ordered based on significance. The following recommendations for further research can be made:

1. An extension of the DEM input calibration of the scour protection material is recommended to create a more accurate simulation. The material characteristics of the armour rock within the simulation should be improved. This can be done using laboratory experiments or field measurements. Creating similar conditions within a simulation helps to calibrate the bulk behavior of the material. For example, the angle of repose and the penetration resistance are characteristics that should be investigated further. Combining the output of the laboratory experiments and a similar calibration method as presented in this thesis, the representation of the bulk behavior can be improved.

2. To achieve a more realistic behavior of the subsoil in the simulation, and therefore the simulation in general, the approach on how to include the subsoil should be improved. This can be done using different methods:

a) The cone penetration test (CPT) data can be used to calibrate different parameter inputs in the DEM. Khosravi et al. (2020) identified the DEM parameters that influence the measured data of the CPT. The inter-particle static friction ($\mu_{s,p-p}$) and rolling resistance coefficient ($\mu_{r,p-p}$), appear to have strong influences on the measured tip resistance ($_c$), but a milder effect on the friction sleeve measurements (f_s).

b) Alternatively the subsoil can be included as a continuum material. the subsoil is commonly presented as a continuum and this has proven to be efficient (Murphy et al., 2018; Fan et al., 2021). The subsoil could be represented with a Finite Element Method (FEM). The combination of DEM and FEM can become part of the currently used penetration prediction models. A difficulty that might arise from a DEM-FEM combination is the interface between the two models.

3. The domain size of the reference simulation is set at $12 * 12m^2$, resulting in a $2m$ window between the monopile and the environmental boundary in the simulation. A further decrease for this window can be investigated to reduce the number of particles within the simulation. Different monopile masses and diameters should be included, especially the monopile mass can result in different reaction forces within the scour protection. Therefore different environmental sizes might be required.

4. Another option to decrease the number of particles included within the simulation is by integrating a Cylindrical Periodic Boundary (CPB). Within a CPB, particles that leave one boundary will re-enter at the opposite boundary. In the artcile by Mohajeri et al. (2020), a CPB is successfully implemented, reducing the environment to a quarter of the total environment.

5. The breaking of the scour protection stone should be investigated. When breaking is considered of importance, a breaking model can be included in the simulation. For example, Ciantia et al. (2015) developed a computationally efficient DEM crushing model to capture the load-deformation behavior of sand, including grain crushing. Later improved in Ciantia et al. (2019). The crushable DEM grain model is adopted from a Herz-Mindlin contact law with spherical particles, rotation is constrained within the model.

6. Collecting more data from practice will help validate the model. There is a large variation within the available data on monopile installation. More data would create the opportunity to seek correlations within the data. It is recommended to collect more crane hook load data from all monopiles installed, this is needed in determining the force acting on the scour protection. Also, data on different monopile diameters and wall thicknesses should be gathered. This can for example be achieved by collaboration with other offshore contractors.

7. It is recommended to gather different types of data. An example would be the data acquisition of the scour protection before and after monopile installation.

Currently, as-built data is measured before and after monopile installation. To get more insight into the rock movement, an option would be to use colored stones. Rock monitoring can help identify the motion of the rocks and therefore the possible rolling of the rocks during monopile installation.

8. Currently the environmental conditions like flow and weather/wave conditions are kept outside the scope of the research. Within future research, the appropriateness of those assumptions should be investigated.

Bibliography

Ai, J., Chen, J. F., Rotter, J. M., & Ooi, J. Y. (2011). Assessment of rolling resistance models in discrete element simulations. *Powder Technology*, *206*(3), 269–282. https://doi.org/10.1016/J.POWTEC.2010.09.030

Alm, T., & Hamre, L. (1998). Soil model for pile driveability predictions. *Offshore Technolog Conference*.

Alm, T., & Hamre, L. (2001). Soil model for pile driveability predictions based on CPT interpretations. *International Conference on Soil Mechanics and Geotechnical Engineering*.

Altair EDEM 2021.1. (2021).

Amidon, G. E., Meyer, P. J., & Mudie, D. M. (2017). Particle, Powder, and Compact Characterization. *Developing Solid Oral Dosage Forms: Pharmaceutical Theory and Practice: Second Edition*, 271–293. https://doi.org/10.1016/B978-0-12-802447-8.00010-8

Balmoral Comtec Ltd. (2022). Fixed wind turbine solutions. https://www.balmoraloffshore.com/solutions/offshore-wind/fixed-wind-turbine-solutions

Barkanov, E. (2001). INTRODUCTION TO THE FINITE ELEMENT METHOD. *Institute of Materials and Structures*.

Bharadwaj, R. (2014). What is Discerete Element Method? *Powder & Bulk Solids*. https://www.powderbulksolids.com/what-discrete-element-method

Bhattacharya, S. (2014). Challenges in Design of Foundations for Offshore Wind Turbines. *Engineering & Technology Reference*. https://doi.org/10.1049/etr.2014.0041

Bradbury, A. P., Latham, J. P., & Allsop, N. (1991). Rock armour stability formulae-influence of stone shape and layer thickness. *Proceedings of the Coastal Engineering Conference*, *2*. https://doi.org/10.1061/9780872627765.110

Brasseur, S., Kirkwood, R., & Aarts, G. (2018). *Seal monitoring and evaluation for the Gemini offshore windfarm: Tconstruction - 2015 report* (tech. rep.). Wageningen University.

Breusers, H. N. C., & Raudkivi, A. J. (1991). *Scouring*. Rotterdam : A.A. Balkema.

Burns, S. J., Piiroinen, P. T., & Hanley, K. J. (2019). Critical time step for DEM simulations of dynamic systems using a Hertzian contact model. *International Journal for Numerical Methods in Engineering*, *119*(5). https://doi.org/10.1002/nme.6056

Cerfontaine, B., Brown, M., Ciantia, M., Huisman, M., & Ottolini, M. (2021). Discrete element modelling of silent piling group installation for offshore wind turbine foundations. *Proceedings of the second international conference on press-in engineering 2021, kochi, japan*. https://doi.org/10.1201/9781003215226-25

Ciantia, M. O., Arroyo, M., Calvetti, F., & Gens, A. (2015). An approach to enhance efficiency of dem modelling of soils with crushable grains. *Geotechnique*, *65*(2). https://doi.org/10.1680/geot.13.P.218

Ciantia, M. O., O'Sullivan, C., & Jardine, R. J. (2019). Pile penetration in crushable soils: Insights from micromechanical modelling. *17th European Conference on Soil Mechanics and Geotechnical Engineering, ECSMGE 2019 - Proceedings*. https://doi.org/10.32075/17ECSMGE-2019-1111

Ciria, Cur, & Cetmef. (2006). *The Rock Manual. The use of rock in hydraulic engineering.*

Cundall, P. A., & Strack, O. D. (1979). A discrete numerical model for granular assemblies. *Geotechnique*, *29*(1). https://doi.org/10.1680/geot.1979.29.1.47

DNVGL-RP-C212. (2017). *Offshore soil mechanicsand geotechnical engineering* (tech. rep.). DNVGL.

Do, H. Q., Aragón, A. M., & Schott, D. L. (2018). A calibration framework for discrete element model parameters using genetic algorithms. *Advanced Powder Technology*, *29*(6). https://doi.org/10.1016/j.apt.2018.03.001

EDEM. (2019). *Calibrating DEM Models for Powder Simulation: Challenges, Advances & Guidelines* (tech. rep.). EDEM.

EDEM2.4 user guide (tech. rep.). (2011). DEMSolutions.

Elskamp, F., Kruggel-Emden, H., Hennig, M., & Teipel, U. (2017). A strategy to determine DEM parameters for spherical and non-spherical particles. *Granular Matter*, *19*(3). https://doi.org/10.1007/s10035-017-0710-0

Esteban, M. D., López-Gutiérrez, J. S., Negro, V., & Sanz, L. (2019). Riprap scour protection for monopiles in offshore wind farms. *Journal of Marine Science and Engineering*, *7*(12). https://doi.org/10.3390/JMSE7120440

Evans, T. M., & Valdes, J. R. (2011). The microstructure of particulate mixtures in one-dimensional compression: Numerical studies. *Granular Matter*, *13*(5). https://doi.org/10.1007/s10035-011-0278-z

Fan, S., Bienen, B., & Randolph, M. F. (2021). Effects of Monopile Installation on Subsequent Lateral Response in Sand. II: Lateral Loading. *Journal of Geotechnical and Geoenvironmental Engineering*, *147*(5). https://doi.org/10.1061/(asce)gt.1943-5606.0002504

Fazeres-Ferradosa, T., Taveira-Pinto, F., Romão, X., Vanem, E., Reis, M. T., & das Neves, L. (2018). Probabilistic design and reliability analysis of scour protections for offshore windfarms. *Engineering Failure Analysis*, *91*. https://doi.org/10.1016/j.engfailanal.2018.04.035

Frey, H. C., & Patil, S. R. (2002). Identification and review of sensitivity analysis methods. *Risk Analysis*, *22*(3). https://doi.org/10.1111/0272-4332.00039

Froehlich, D. C. (2011). Mass Angle of Repose of Open-Graded Rock Riprap. *Journal of Irrigation and Drainage Engineering*, *137*(7). https://doi.org/10.1061/(asce)ir.1943-4774.0000316

Golightly, C. (2014). Tilting of monopiles: Long, heavy and stiff; pushed beyond their limits. *Ground Engineering*, (January).

Gupta, B. K., & Basu, D. (2020). Offshore wind turbine monopile foundations: Design perspectives. *Ocean Engineering*, *213*. https://doi.org/10.1016/j.oceaneng.2020.107514

Holeyman, A., Peralta, P., & Charue, N. (2015). Boulder-soil-pile dynamic interaction. *Frontiers in Offshore Geotechnics III - Proceedings of the 3rd International Symposium on Frontiers in Offshore Geotechnics, ISFOG 2015*. https://doi.org/10.1201/b18442-72

Horabik, J., & Molenda, M. (2016). Parameters and contact models for DEM simulations of agricultural granular materials: A review. *Biosystems Engineering*, *147*, 206–225. https://doi.org/10.1016/J.BIOSYSTEMSENG.2016.02.017

ITRC. (2022). Cone Penetrometer Testing. https://asct-1.itrcweb.org/3-5-cone-penetrometer-testing/

Ji, S., Li, L., Motra, H. B., Wuttke, F., Sun, S., Michibayashi, K., & Salisbury, M. H. (2018). Poisson's Ratio and Auxetic Properties of Natural Rocks. *Journal of Geophysical Research: Solid Earth*, *123*(2). https://doi.org/10.1002/2017JB014606

Kay, S., Gourvenec, S., Palix, E., & Alderlieste, E. (2021). *Intermediate Offshore Foundations*. https://doi.org/10.1201/9780429423840

Khosravi, A., Martinez, A., & Dejong, J. T. (2020). Discrete element model (DEM) simulations of cone penetration test (CPT) measurements and soil classification. *Canadian Geotechnical Journal*, *57*(9). https://doi.org/10.1139/cgj-2019-0512

Lee, J., & Zhao, F. (2020). *Global Offshore Wind Report 2020* (tech. rep.). Global Wind Energy Council.

Lengkeek, W., Didderen, K., Teunis, M., Driessen, F., Coolen, J., Bos, O., Vergouwen, S., Raaijmakers, T., de Vries, M., & van Koningsveld, M. (2017). *Eco-friendly design of scour protection: potential enhancement of ecological functioning in offshore wind farms* (tech. rep.). https://edepot.wur.nl/411374

Li, X. F., Zhang, Q. B., Li, H. B., & Zhao, J. (2018). Grain-Based Discrete Element Method (GB-DEM) Modelling of Multi-scale Fracturing in Rocks Under Dynamic Loading. *Rock Mechanics and Rock Engineering*, *51*(12). https://doi.org/10.1007/s00603-018-1566-2

Lobo-Guerrero, S., & Vallejo, L. E. (2007). Influence of pile shape and pile interaction on the crushable behavior of granular materials around driven piles: DEM analyses. *Granular Matter*, *9*(3-4). https://doi.org/10.1007/s10035-007-0037-3

Lommen, S., Schott, D., & Lodewijks, G. (2014). DEM speedup: Stiffness effects on behavior of bulk material. *Particuology*, *12*(1), 107–112. https://doi.org/10.1016/J.PARTIC.2013.03.006

Lunne, T., Robertson, P., & Powell, J. (1997). Cone Penetration Testing in Geotechnical Practice., 1997. *Blackie Academic and Professional, ...*

Matutano, C., Negro, V., López-Gutiérrez, J. S., & Esteban, M. D. (2013). Scour prediction and scour protections in offshore wind farms. *Renewable Energy*, *57*. https://doi.org/10.1016/j.renene.2013.01.048

Mohajeri, M. J., Do, H. Q., & Schott, D. L. (2020). DEM calibration of cohesive material in the ring shear test by applying a genetic algorithm framework. *Advanced Powder Technology*, *31*(5). https://doi.org/10.1016/j.apt.2020.02.019

Mohajeri, M. J., van Rhee, C., & Schott, D. L. (2021). Replicating cohesive and stress-history-dependent behavior of bulk solids: Feasibility and definiteness in DEM calibration procedure. *Advanced Powder Technology*, *32*(5). https://doi.org/10.1016/j.apt.2021.02.044

Murphy, G., Igoe, D., Doherty, P., & Gavin, K. (2018). 3D FEM approach for laterally loaded monopile design. *Computers and Geotechnics*, *100*, 76–83. https://doi.org/10.1016/J.COMPGEO.2018.03.013

Netherlands Enterprise Agency. (2015). Offshore wind energy in the Netherlands. *The roadmap from 1,000 to 4,500 MW offshore wind capacity.*

Qu, T., Wang, M., & Feng, Y. (2022). Applicability of discrete element method with spherical and clumped particles for constitutive study of granular materials. *Journal of Rock Mechanics and Geotechnical Engineering*, *14*(1), 240–251. https://doi.org/10.1016/J.JRMGE.2021.09.015

Ramsey, N. (2002). A calibrated model for the interpretation of cone penetration tests (CPTs) in North Sea quaternary soils. *Offshore Site Investigation and Geotechnics "Diversity and Sustainability" - Proceedings of an International Conference, OSIG 2002*.

Richter, C., Rößler, T., Kunze, G., Katterfeld, A., & Will, F. (2020). Development of a standard calibration procedure for the DEM parameters of cohesionless bulk materials – Part II: Efficient optimization-based calibration. *Powder Technology*, *360*. https://doi.org/10.1016/j.powtec.2019.10.052

Robertson, P. K. (1990). Soil classification using the cone penetration test. *Canadian Geotechnical Journal*, *27*(1). https://doi.org/10.1139/t90-014

Robertson, P. K. (2009). Interpretation of cone penetration tests - A unified approach. *Canadian Geotechnical Journal*, *46*(11). https://doi.org/10.1139/T09-065

Schiereck, G. J. (2004). *Introduction to Bed, Bank and Shore Protection*. https://doi.org/10.4324/9780203397879

Shonberg, A., Harte, M., Schupp, J., Meissl, S., Liingaard, M. A., & Anusic, I. (2017). Comparison of self weight penetration prediction methods for large diameter monopiles in north sea soils. *Proceedings of the Annual Offshore Technology Conference*, *5*. https://doi.org/10.4043/27763-ms

Sinha, S., & Walton, G. (2019). Understanding continuum and discontinuum models of rock-support interaction for excavations undergoing stress-induced spalling. *International Journal of Rock Mechanics and Mining Sciences*, *123*, 104089. https://doi.org/10.1016/J.IJRMMS.2019.104089

Stevens, R. S., Wiltsie, E. A., & Turton, T. H. (1982). Evaluating pile drivability for hard clay, very dense sand, and rock. *Proceedings of the Annual Offshore Technology Conference*, *1982-May*. https://doi.org/10.4043/4205-ms

Tanaka, H., Momozu, M., Oida, A., & Yamazaki, M. (2000). Simulation of soil deformation and resistance at bar penetration by the Distinct Element Method. *Journal* *of Terramechanics*, *37*(1), 41–56. https://doi.org/10.1016/S0022-4898(99)00013-0

Tang, H., Zhang, X., & Chu, X. (2012). DEM simulation for the effect of rolling resistance on shear band. *Applied Mechanics and Materials*, *204-208*. https://doi.org/10.4028/www.scientific.net/AMM.204-208.246

The Rock Manual (tech. rep.). (2007). CIRIA.

Toolan, F. E., & Fox, D. A. (1977). GEOTECHNICAL PLANNING OF PILED FOUNDATIONS FOR OFFSHORE PLATFORMS. *Proc Inst Civ Eng (Lond)*, *62*(pt 1). https://doi.org/10.1680/iicep.1977.3224

Van Der Male, P. (2020). Lecture Notes 3 - Foundation design.

Verruijt, A. (2018). An Introduction to Soil Mechanics. *SAE Technical Papers*, *30*.

Wensrich, C. M., & Katterfeld, A. (2012). Rolling friction as a technique for modelling particle shape in DEM. *Powder Technology*, *217*, 409–417. https://doi.org/10.1016/J.POWTEC.2011.10.057

Whitehouse, R. J., Harris, J. M., Sutherland, J., & Rees, J. (2011). The nature of scour development and scour protection at offshore windfarm foundations. *Marine Pollution Bulletin*, *62*(1). https://doi.org/10.1016/j.marpolbul.2010.09.007

Zhou, H., Hu, Z., Chen, J., Lv, X., & Xie, N. (2018). Calibration of DEM models for irregular particles based on experimental design method and bulk experiments. *Powder Technology*, *332*, 210–223. https://doi.org/10.1016/J.POWTEC.2018.03.064

Appendices

A. DEM theory

The discrete element method, introduced by Cundall and Strack (1979) is a powerful tool in engineering, used to simulate bulk granular materials. In this section the theory behind the discrete element method is presented. The DEM algorithm can be broken down to 4 steps: initialisation, detect contact, calculate interaction forces and calculation particle position. In Figure A.1 the sequence of these four steps is visualised. The initialization phase of the simulation is critical, this the simulation is set-up. The set-up of the simulation will be discussed in this section.

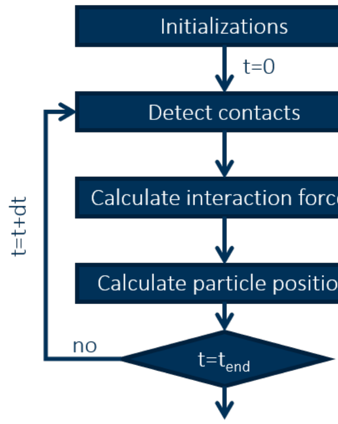

Figure A.1: DEM algorithm

A.1. Simulation set-up

Within the initialization of the DEM simulation the particles and environment are generated and the simulation properties are set.

A.1.1. Bodies

Within DEM different bodies are used in the calculation. A distinguish is made between the particles and geometry.

Particles

Particles in DEM are defined by a shape, material properties and interactions. The material properties are on their term defined by the Poisson's ratio (υ), the solid density (ρ) and Shear/Young's Modulus (G/E). The shape of the materials is typically a sphere defined by a radius (r) and a corresponding size distribution (PSD). Also different shapes are possible, like a assembly of sphere or any ordinary shape. Interaction between particles and particles-geometries interactions are defined by the coefficient of restitution (e), the coefficient of static friction (μ_s) and the coefficient of rolling friction (μ_r).

Geometry
Geometries within a DEM simulation are defined by the same properties as the particles.

A.1.2. Contact models

Hertz-Mindlin (no slip)
The normal force component is derived from Hertzian contact theory, whereas the tangential force based on the work of Mindlin-Deresiewicz. (“Altair EDEM 2021.1”, 2021)
The normal force F_n is given by:

$$F_n = \frac{4}{3} E^* \sqrt{R^*} \delta_n^{\frac{3}{2}} \tag{A.1}$$

In which E^* is the equivalent Young's Modulus and R^* is the equivalent radius:

$$\frac{1}{E^*} = \frac{1 - \upsilon_i^2}{E_i} + \frac{1 - \upsilon_j^2}{E_j} \tag{A.2}$$

$$\frac{1}{R^*} = \frac{1}{R_i} + \frac{1}{R_j} \tag{A.3}$$

Where E_i, υ_i, R_i and E_j, υ_j, R_j are the Young's Modulus, Poisson's ratio and Radius of the spheres in contact. An additional damping force is included in the form of:

$$F_n^d = -2\sqrt{\frac{5}{6}} \beta \sqrt{S_n m^*} \overrightarrow{\upsilon_n^{rel}} \tag{A.4}$$

Where m^* is the equivalent mass, υ_n^{rel} the normal component of the relative velocity, S_n the normal stiffness and β. Given by:

$$m^* = \left(\frac{1}{m_j} + \frac{1}{m_i} \right)^{-} 1 \tag{A.5}$$

$$\beta = \frac{-\ln e}{\sqrt{\ln^2 e + \pi^2}} \tag{A.6}$$

$$S_n = 2E^* \sqrt{R^* \delta_n} \tag{A.7}$$

Where e is the coefficient of restitution. The tangential force (F_t) is:

$$F_t = -S_t \delta_t \tag{A.8}$$

with δ_t the tangential overlap and S_t the tangential stiffness:

$$S_t = 8G^* \sqrt{R^* \delta_n} \tag{A.9}$$

Where G^* is the equiavalent shear modulus. The tangendial damping if formulated as:

$$F_t^d = -2\sqrt{\frac{5}{6}}\beta\sqrt{S_t m^*}\overrightarrow{v_t^{rel}} \tag{A.10}$$

Where v_t^{rel} is the relative tangential velocity. The limit of tangential force is the Coulomb friction $\mu_s F_n$, with μ_s is the coefficient of static friction.

Friction model C
Friction model C goes beyond the standard rolling friction due to the addition of a non-viscous term int he damping torque equation. The total damping M_r is:

$$M_r = M_r^k + M_r^d \tag{A.11}$$

Where M_r^k is the non-viscous damping torque vector and M_r^d is the viscous damping. The non-viscous torque vector depends on the rolling stiffness (k_r) and the relative particle rotation angle (θ_r):

$$M_r^k = -k_r \theta_r \tag{A.12}$$

$$k_r = 3k_n \mu_r^2 R_r^2 \tag{A.13}$$

Where R_r is the equivalent rolling radius, μ_r the coefficient of rolling friction and k_n the normal contact stiffness. The magnitude of the non-viscous damping is limited by:

$$\mid M_r^k \mid \leq \mu_r R_r F_n \tag{A.14}$$

Where F_n is the normal contact force. The viscous damping torque is:

$$m_r^d = -2\eta\sqrt{I_r k_r \omega} \tag{A.15}$$

With η the viscous rolling damping ratio, ω s the relative rotational velocity vector (at the contact point) and I_r is the equivalent moment of inertia for the rotational vibration mode (at the contact point).

A.1.3. Grid size

The simulation environment is divided into grids. In this way, the computer only starts the calculation algorithm in a grid when more than 2 particles are present within this specific grid. A smaller grid size results in faster detection of contact and a faster computational time. Altair EDEM recommends a gird size of 3-6 times the smallest radius in the simulation. For the truck load simulations, the default grid cell size is 3 times the minimum radius in the simulation. (“Altair EDEM 2021.1”, 2021)

B. Scour protection

B.1. Material information

B.1.1. Particle size distribution

The particle size distribution of the scour protection material is tested and documented, the results are shown in Figure B.1 and Table B.1. The grading width of the materials corresponds with a D_{90}/D_{10} of $2,5$ and D_{50} of 134 mm.

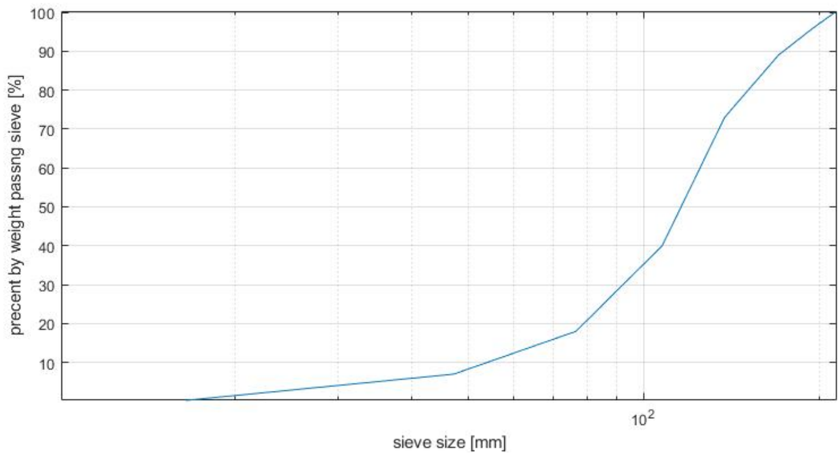

Figure B.1: PSD scour protection material

Sieve num.	Sieve_low [mm]	Sieve_up [mm]	Cumm.	Percentage	D_n50 [mm]
1	0	31,5	0%	0%	15,75
2	31,5	63	7%	7%	47,25
3	63	90	18%	11%	76,5
4	90	125	40%	22%	107,5
5	125	150	73%	33%	137,5
6	150	190	89%	16%	170
7	190	200	96%	7%	195
8	200	225	100%	4%	212,5

Table B.1: Particle size distribution of scour protection material

B.1.2. Bulk density test

Bulk density test have been executed and documented on rock material, the results are shown in Table B.2. From this data the buoyant density ρ' is calculated, assuming that no water is present within the rock the buoyant density is: $\rho_{'=\rho_s-\rho_w} = 1,625\ t/m^3$.

Density of solid rock	ρ_s	2,65	t/m^3
Total Volume	V_t	1414	$[l]$
Void volume	V_v	651	$[l]$
Porosity	n	0.46	$[-]$
Void ratio	e	0,85	$[-]$
Sea water density	ρ_w	1,025	t/m^3
Bulk dry density	ρ_d	1,43	t/m^3
Submerged bulk density	ρ'	0,93	t/m^3

Table B.2: Results from bulk density test of Normal Density 63-200mm rock

C. Settling time of material bed

In Figure C.1 the average particle motion of the material bed in the full-scale monopile simulation. A clear converging behavior of the average particle velocity can be observed. When the average particle motion is below $0.02m/s$ the bed is considered stable. So a settling time of 2,5 seconds is required.

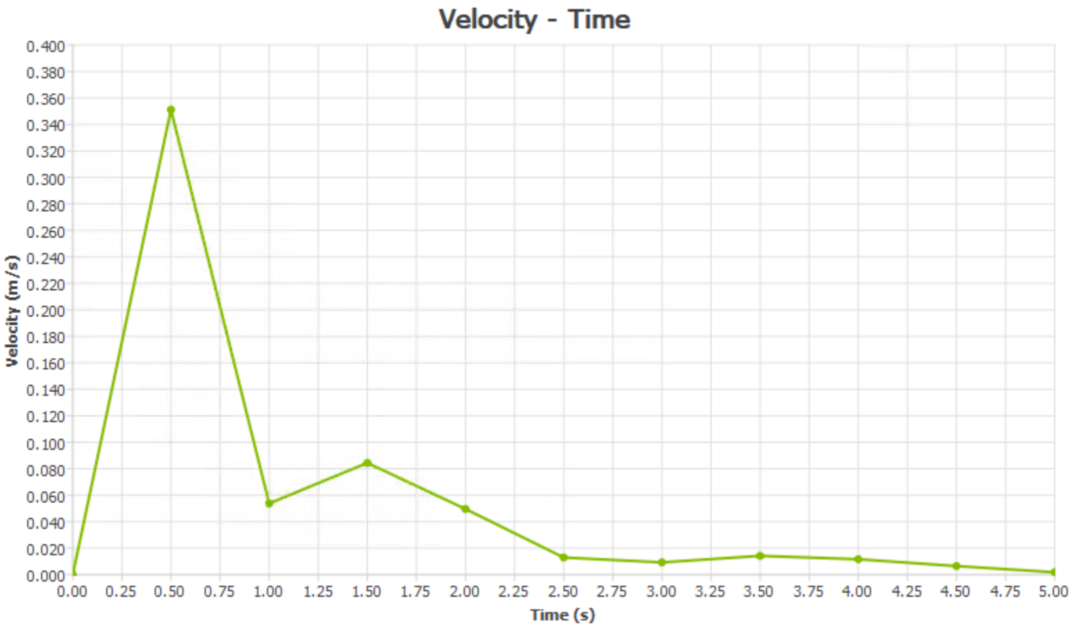

Figure C.1: Average particle velocity

D. Angle of Repose

The angle of repose of the scour protection material is not given in the material data. Two approaches have been used to determine the angle of repose of the materials. Firstly, as-build data from two installed scour protections is used. Secondly, the mass angle of repose of Froehlich (2011) is used.

D.1. Angle of repose from As-build

Using the as-built data of two installed scour protections, the installation angle on the seabed can be determined. This did not give promising results regarding the AoR. This angle represents the installation angle, leading to an underestimation of the AoR. This angle is not representative of the steepest angle under which the stack is stable. Therefore

The data from the as-build of the scour protection is available in graphical format. A plot digitizer is used to make the data numerical. In this data the Angle of the scour protection is approximated for 4 cross-sections of 2 scour protection. These 8 installation angles are visualized in Figure D.1 for MP2 and Figure D.2 for MP3. The corresponding angles are included in the graph, it may be concluded that those angles do not correspond to the AoR due to their low value.

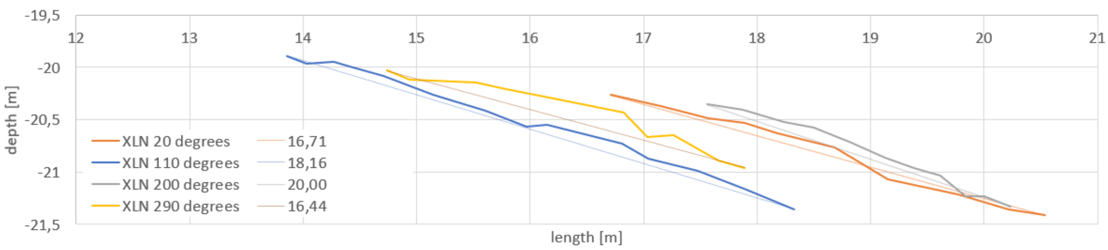

Figure D.1: Installation angle of scour protection MP2

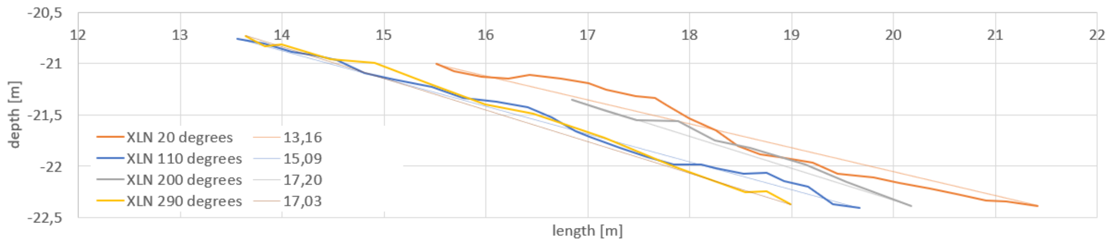

Figure D.2: Installation angle of scour protection MP2

D.2. Mass angle or repose by Froehlich (2011)

Froehlich (2011) refers to a Mass AoR, however, does it measure explanation correspond with the explanation of a regular AoR. Froehlich (2011) states: 'Stockpile side-slope angles were measured using a wooden board with a mechanical inclinometer attached.' With experimental data from stockpiles located at quarries, he created a formula to calculate the estimated angle of repose. Stated is that the AoR of rock materials is not changing significantly when submerged.

$$\hat{\phi}_r = \phi_{r1} * \left(\frac{D_{85}}{D_{50}}\right)^{0.125} \tag{D.1}$$

with ϕ_{r1}=

- 30.9° for round stones
- 33.4° for sub round and sub angular stone
- 37.1° for angular stone

This formula is largely dependent on the shape of the materials combined with the particle size distribution. The particle size distribution is known, therefore the D_{85} and D_{50} can be filled in. As the rocks are freshly cut rock from the quarry the rocks are identified as Angular rock.

Therefore $\hat{\phi}_r = 37.1 * \left(\frac{161.9}{134}\right)^{0.125}$, leading to an angle or repose of 38°

E. Truck Load simulations

	Parameter input					EDEM output	
sim	Coefficient of static friction μ_s $[-]$	Coefficient of rolling friciton μ_r $[-]$	Density ρ $[kg/m^3]$	PSD	Shear modulus G $[Pa]$	Porosity n $[-]$	AoR ϕ [°]
1	0,4	0,4	1625	5 bins	1E+07	0,41	38
2	0,4	0,4	1625	5 bins	1E+08	0,43	41
3	0,4	0,4	1625	7 bins	1E+07	0,39	38
4	0,4	0,4	1625	7 bins	1E+08	0,40	36
5	0,4	0,4	2650	5 bins	1E+07	0,42	38
6	0,4	0,4	2650	5 bins	1E+08	0,44	37
7	0,4	0,4	2650	7 bins	1E+07	0,39	36
8	0,4	0,4	2650	7 bins	1E+08	0,40	35
9	0,4	0,9	1625	5 bins	1E+07	0,43	46
10	0,4	0,9	1625	5 bins	1E+08	0,44	43
11	0,4	0,9	1625	7 bins	1E+07	0,40	41
12	0,4	0,9	1625	7 bins	1E+08	0,41	44
13	0,4	0,9	2650	5 bins	1E+07	0,44	39
14	0,4	0,9	2650	5 bins	1E+08	0,44	43
15	0,4	0,9	2650	7 bins	1E+07	0,40	38
16	0,4	0,9	2650	7 bins	1E+08	0,40	39
17	0,9	0,4	1625	5 bins	1E+07	0,44	37
18	0,9	0,4	1625	5 bins	1E+08	0,46	39
19	0,9	0,4	1625	7 bins	1E+07	0,43	39
20	0,9	0,4	1625	7 bins	1E+08	0,43	41
21	0,9	0,4	2650	5 bins	1E+07	0,47	40
22	0,9	0,4	2650	5 bins	1E+08	0,46	39
23	0,9	0,4	2650	7 bins	1E+07	0,43	43
24	0,9	0,4	2650	7 bins	1E+08	0,43	38
25	0,9	0,9	1625	5 bins	1E+07	0,47	52
26	0,9	0,9	1625	5 bins	1E+08	0,47	48
27	0,9	0,9	1625	7 bins	1E+07	0,45	43
28	0,9	0,9	1625	7 bins	1E+08	0,45	42
29	0,9	0,9	2650	5 bins	1E+07	0,50	44
30	0,9	0,9	2650	5 bins	1E+08	0,49	35
31	0,9	0,9	2650	7 bins	1E+07	0,45	41
32	0,9	0,9	2650	7 bins	1E+08	0,45	44
33	0,5	0,5	1625	5 bins	1E+08	0,44	39

Table E.1: Truck load simulation

F. Full-Scale Monopile Simulation

In Table F.1 and Table F.2 the simulation input for the Full-Scale Monopile Simulation are given.

sim	PSD	G $[Pa]$	dt $[s]$
1	5bins	10^7	$1 * 10^{-5}$
2	5bins	10^7	$2 * 10^{-5}$
3	5bins	10^7	$0,5 * 10^{-5}$
4	5bins	10^8	$1 * 10^{-5}$
5	5bins	10^8	$2 * 10^{-5}$
6	5bins	10^8	$0,5 * 10^{-5}$

Table F.1: Simulations of Experiments A

sim		horz domain $[m^2]$	t_{sand} $[m]$	G_{sand} $[Pa]$	t_{SP} $[m]$	time-scale
1	Base Case	$12 * 12$	1.75	10^8	2	1s:10min
2	Exp. B Domain size	$9 * 9$	1.75	10^8	2	1s:10min
3		$15 * 15$	1.75	10^8	2	1s:10min
4		$12 * 12$	3.6	10^8	2	1s:10min
5		$12 * 12$	0	10^8	2	1s:10min
6		$12 * 12$	1.75	10^7	2	1s:10min
7		$12 * 12$	1.75	$3 * 10^9$	2	1s:10min
8	Exp. C Scour thickness	$12 * 12$	1.75	10^8	1.75	1s:10min
9		$12 * 12$	1.75	10^8	2.25	1s:10min
10	Exp. D Time-scale	$12 * 12$	1.75	10^8	2	2s:10min
11		$12 * 12$	1.75	10^8	2	0.5s:10min
12		$12 * 12$	1.75	10^8	2	1s:10min
13		$12 * 12$	1.75	10^8	2	5s:10min
14		$12 * 12$	1.75	10^8	2	10s:10min
15		$12 * 12$	1.75	10^8	2	20s:10min

Table F.2: Simulations of Experiments B, C and D

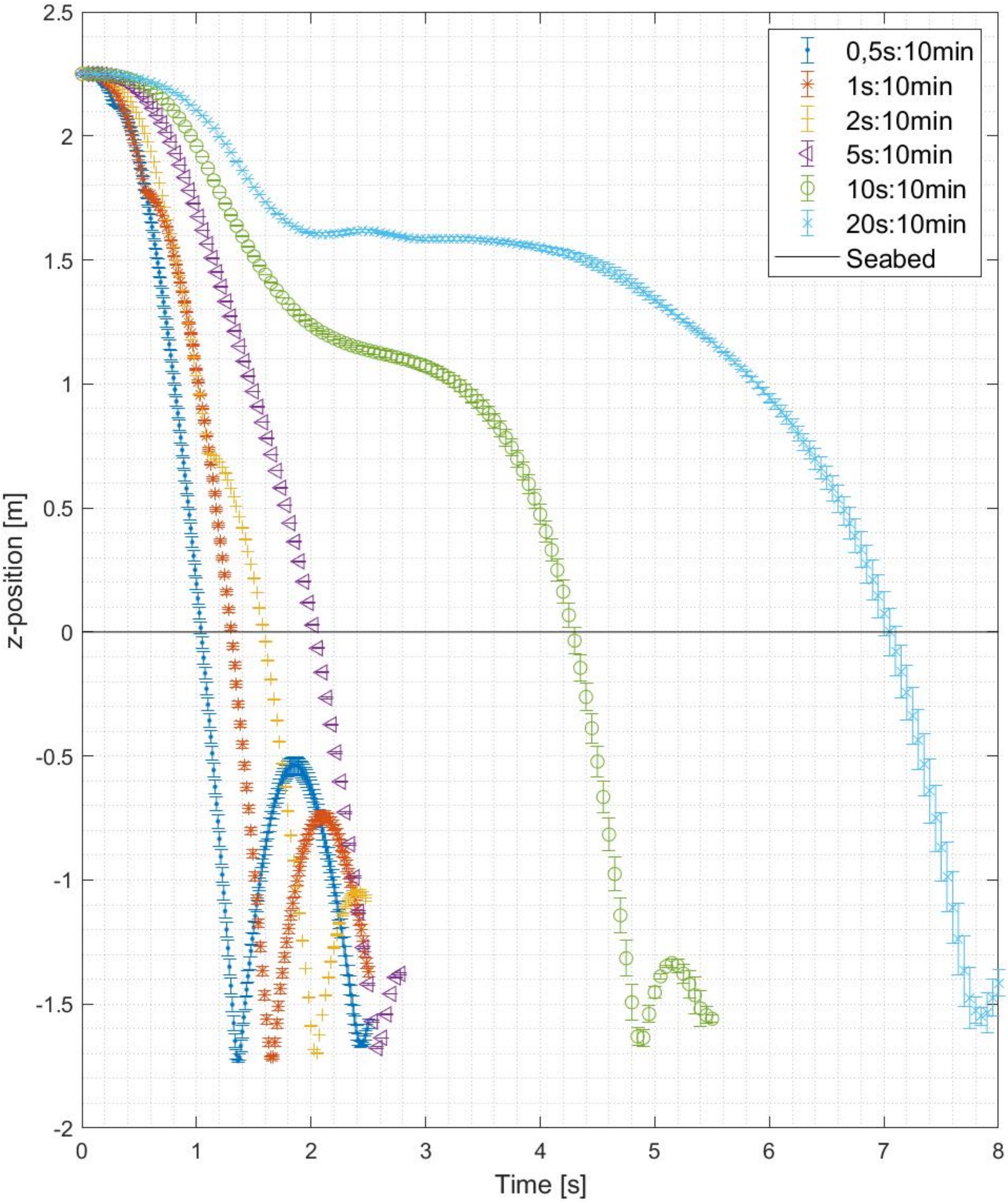

Figure F.1: Experiment D. Time scaling results (including standard deviation). Depth over time

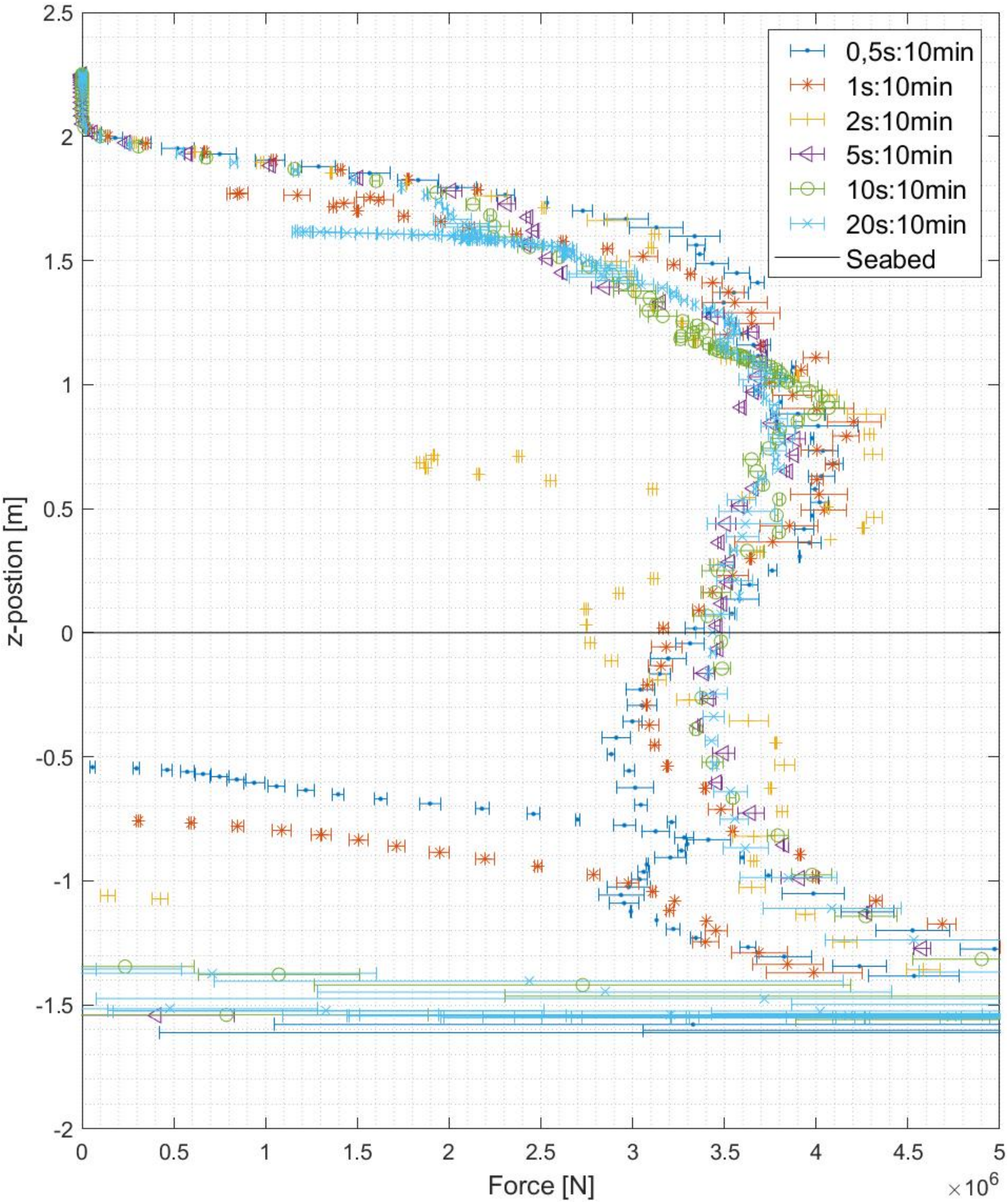

Figure F.2: Experiment D. Time scaling results (including standard deviation). Reaction force over depth.